Investigation of Gas-Phase Methane Oxidation by Reactor Profile Measurements and Microkinetic Modeling

vorgelegt von
Master of Engineering
Sardor Mavlyankariev
aus Taschkent, Usbekistan

Von der Fakultät II – Mathematik und Naturwissenschaften
der Technischen Universität Berlin
zur Erlangung des akademischen Grades
Doktor der Ingenieurwissenschaften
- Dr. Ing. -

genehmigte Dissertation

Promotionsausschuss:

Vorsitzender: Prof. Dr. Peter Hildebrandt
Berichter/Gutachter: Prof. Dr. Reinhard Schomäcker
Berichter/Gutachter: Prof. Dr. Robert Schlögl
Berichter/Gutachter: Prof. Dr. Manfred Baerns

Tag der wissenschaftlichen Aussprache: 8. Juli 2013

Berlin 2013

D 83

Contents

Abstract

Gas-phase reactions of oxidative coupling of methane (OCM) – one of the reaction channels of gas-phase methane oxidation – play a crucial role during a catalytic OCM reaction which is currently conducted at high temperatures (above 500 °C). For this reason, understanding the mechanism of gas-phase OCM reaction quantitatively on an atomic basis is crucial for further disentangling the complex interplay of gas-phase and surface chemistry in a catalytic OCM. In this thesis, a contribution to quantitative understanding of gas-phase OCM was done by microkinetic modeling and experiments in a spatially resolved profile reactor which is positioned as a tool for proper validation of a microkinetic model.

Gas phase experiments in a spatially resolved profile reactor were done at the inlet carbon-to-oxygen atomic ratios of 2 – 8 and nominal total inlet volumetric flow rates of 500 – 4000 mln $\cdot$ min^{-1} (flow rate at 293.15 K and 1 bar pressure), in the pressure range of 1 – 20 bar and non-isothermal reactor heating profiles spanning temperature range from 643 to 900 °C. Simulations of the experimental reactor profiles were performed with CHEMKIN Pro software on the basis of boundary-layer equations expressed through cylindrical shear-flow reactor model. As the boundary conditions for simulation, measured reactor oven temperature profiles were set, and to measure temperature profiles of the reactor heating oven as a function of electrical power and axial position a separate experimentation was designed and carried out. The microkinetic models of Dooley et al. [1], Lopez et al. [2], Warnatz et al. [3], Hughes et al. [8], Konnov [4], Mims et al. [5], Zanthoff and Baerns [7], Wang et al. [6], Sun et al. [9] and GRI 3.0 [10] of varying complexity were tested against the obtained experimental species and temperature profiles. Evaluation criterion was qualitative agreement with the experimental reactor profiles and quantitative agreement with reactor exit mole

fractions.

With experimental results it was corroborated that increase of temperature and pressure greatly accelerate the extent of gas-phase OCM reactions according to kinetic rules. Main products were water, carbon monoxide, hydrogen, carbon dioxide and C_2 hydrocarbons (ethane and ethylene) in descending order. Maximal combined selectivities and yields of C_2 hydrocarbons amount to 25% and 7.3%,respectively, at 30% methane conversion for lowest considered C/O ratio of 2. The space-time yield of the target C_2 hydrocarbons reaches an industrially relevant window of 1 to 10 $\mathrm{mol \cdot m^{-3} \cdot s^{-1}}$ from 4 bar on at high volumetric flow rates and low-to-middle (2 - 4) reactant carbon-to-oxygen atomic ratios. The simulation results showed good qualitative agreement except for the model of Konnov which showed inverse H_2O/H_2 ratio at carbon-to-oxygen atomic ratio of 2 and 4 bar pressure conditions. Quantitative prediction was not completely correct for any of the models and was good either at the end of the considered simulation zone or fully correct along the whole axial profile only for selected species. The models of Dooley et al. [1] and Mims et al. [5] were also in satisfactory quantitative agreement with experimental reactor profiles.

Due to their good performance, the models of Dooley et al. [1] and Mims et al. [5] were chosen for further detailed evaluation with reaction path analysis and sensitivity analysis. The reaction path analysis at the inlet methane-to-oxygen atomic ratio of 2, 4 bar pressure, 2000 $\mathrm{mln \cdot min^{-1}}$ flow rate and 500 °C inlet gas temperature conditions done at several reactor axial positions (total 4 positions) showed that the primary step of methane activation in the initiation regime is by molecular oxygen with generation of methyl and hydroperoxyl radicals. At a later reactor zone in the chain propagation and branching regimes in the presence of reactant oxygen the main pathways of methane activation were found to be by hydroxyl, hydrogen and hydroperoxyl radicals, whereas hydrogen radical-atoms constitute the main activation pathway in the absence of oxygen.

At low temperatures in the zone before reaction light-off, transformation of methyl radicals to mainly methylperoxyl radicals is observed, whereas coupling of methyl radicals to ethane is detected at sufficiently high temperatures, at least from 750 °C on. Further transformation of methylperoxyl radicals to formaldehyde and methanol is documented, in agreement with experimental observations

of other authors on formation of these oxygenates at low temperatures. A route for ethylene formation not directly by oxidative dehydrogenation of ethane but rather through decomposition of ethylperoxyl radicals at ca. 495 °C and by unimolecular decomposition of oxygen-containing higher $C_3 - C_4$ radicals, propylene oxide and C_3 alcohols at ca. 940 °C is observed.

Intrinsic limitations for high C_2 hydrocarbons yields in gas phase are found in that formed ethane and ethylene are not only decomposed by the same radicals which activate methane ($OH^\bullet$, $H^\bullet$, $HO_2^\bullet$), but also by desirable methyl radicals that dehydrogenate them to ethyl and ethenyl radicals, respectively. From this result, the function of a catalyst as not only a methyl radical generator, but also as an effective platform on which methyl radicals combine before their reaction with C_2 hydrocarbons is proposed.

An operation window in which a gas-phase OCM could operate as a technically feasible process was determined with calculations using the Dooley et al. model. As the modeling parameters, carbon-to-oxygen (C/O) equivalence ratio of 2 and 8, gas temperature (from 800 to 1550 K) and pressure (from 1 to 10 bar) were set. In particular, if high combined C_2 hydrocarbons selectivity - at the expense of high methane conversion and high combined C_2 yield - is a target, then a higher C/O ratio (of 8) and higher pressures were found to be favourable. If a high yield of C_2 hydrocarbons is a target, then low (of 2) to moderate (of 2 - 8) C/O ratios are desirable. In both cases, higher pressures (from 5 bar on) for highest C_2 product selectivities and yields are imperative.

Kurzfassung

Die oxidative Kopplung von Methan (OCM) in der Gasphase ist einer der möglichen Reaktionspfade während der Gasphasenoxidation von Methan und kommt so auch während der katalysierten OCM Reaktion bei Temperaturen über 500 °C vor. Um das komplexe Zusammenspiel zwischen Gasphasen- und Oberflächenchemie während der katalysierten OCM besser zu verstehen, ist es notwendig, ein quantitatives Verständnis der reinen gasphasen OCM zu erlangen. In der vorliegenden Arbeit wurde die gasphasen OCM in einem Profilreaktor experimentell Untersucht und mittels mikrokinetischer Modellierung theoretisch beschrieben.

Die Gasphasenexperimente wurden durchgeführt bei einem (atomaren) Kohlenstoff- zu Sauerstoffverhältnis (C/O) von 2 bis 8, der Eingangsvolumenstrom betrug 500 – 4000 $\mathrm{mln \cdot min^{-1}}$ bezogen auf 293.15 K und 1 bar; der Druck wurde zwischen 1 und 20 bar variiert. Die ortsabhängige Temperatur im Reaktor nahm Werte zwischen 643 und 900 °C an. Es wurde versucht, die experimentell ermittelten Edukt/Produkt-Profile mit Hilfe der Software CHEMKIN Pro zu simulieren, unter der Annahme zylindrischen Scherflusses im Reaktor. Als Randbedingungen für die Simulation wurden die experimentell bestimmten Temperaturprofile des Reaktorofens verwendet.

Es wurden 10 verschiedene mikrokinetische Modelle unterschiedlicher Komplexität getestet und mit den experimentellen Spezies- und Temperaturprofilen verglichen. Bewertet wurden die Ergebnisse anhand vom Grad der qualitativen und quantitativen Übereinstimmung mit den gemessenen Profilen und den Molenbrüchen am Reaktorausgang. Die Experimente stützen die bekannte Tatsache, dass die gasphasen OCM mit Zunahme von Temperatur und Druck stark beschleunigt wird. Die Hauptprodukte waren in abnehmender Reihenfolge: Wasser, Kohlenmonoxid, Wasserstoff, Kohlendioxid, und C_2–Kohlenwasserstoffe (Ethan,

Ethen). Die maximal erreichten kombinierten Selektivitäten und Ausbeuten für C_2–Kohlenwasserstoffe betrugen 25% bzw. 7.3% bei einem Gesamtumsatz von 30% bezogen auf Methan und bei einem C/O Verhältnis von 2, was auch gleichzeitig das kleinste gemessene Verhältnis war. Die Raum-Zeit-Ausbeute der gewünschten C_2 Kohlenwasserstoffe erreicht den industriell relevanten Bereich von 1 bis 10 $\mathrm{mol} \cdot \mathrm{m}^{-3} \cdot \mathrm{s}^{-1}$ beginnend bei 4 bar aufwärts und hohen Volumenströmen, und niedrig bis mittleren (2 – 4) C/O Verhältnissen. Die Resultate der Simulation zeigten gute qualitative Übereinstimmung für alle Modelle bis auf jenes von Konnov [4], welches ein invertiertes H_2O/H_2 Verhältnis vorhersagt, bei einem C/O Verhältnis von 2 und 4 bar Druck. Keines der Modelle konnte die gemessenen Profile für alle Spezies quantitativ korrekt vorhersagen, eine gute Übereinstimmung wurde immer nur partiell erreicht, nämlich entweder für einige wenige Spezies entlang des ganzen Reaktors oder für die Gesamtzusammensetzung am Ende des Reaktors. Die Modelle von Dooley et al. [1] und Mims et al. [5] lieferten insgesamt die besten, wenngleich auch nur befriedigende Ergebnisse. Anhand dieser beiden Modelle wurde nun eine Reaktionspfad- und Sensitivitätsanalyse durchgeführt. Die Reaktionspfadanalyse (C/O = 2, 4 bar, 500 °C, 2000 $\mathrm{mln} \cdot \mathrm{min}^{-1}$ Fluss) an mehreren Stellen im Reaktor (insgesamt 4) lieferte den ersten Schritt der Methanaktivierung im Initialbereich: die Reaktion von Methan und molekularem Sauerstoff zu Methyl- und Hydroperoxylradikalen. Weiter hinten im Reaktor, in der Zone wo Kettenfortpflanzung und Verzweigung eine Rolle spielen, waren die Hauptreaktionspfade der Methanaktivierung Hydroxyl-, Wasserstoff- und Hydroperoxylradikale, solange O_2 zugegen war; in Abwesenheit von O_2 hingegen stellen hauptsächlich Wasserstoffatome den Aktivierungspfad dar. Bei niedriger Temperatur, und bevor die Reaktion zündet, wandeln sich Methyl- in Methylperoxylradikale um, wohingegen die Kopplung von Methylradikalen zu Ethan erst bei Temperaturen von über 750 °C stattfindet. Methylperoxylradikale reagieren weiter zu Formaldehyd und Methanol, was in Übereinstimmung steht mit den Beobachtungen anderer Autoren bezüglich der Bildung dieser Oxygenate bei niedrigen Temperaturen. Die Ethenbildung auf einem anderen Weg als durch oxidative Dehydrogenierung ist auch möglich, nämlich durch Zersetzung von Ethylperoxylradikalen bei ca. 495 °C und durch unimolekularen Zerfall von Sauerstoffhaltigen C_3 und C_4 Radikalen, sowie Propy-

lenoxid und C_3 Alkoholen bei ca. 940 °C.

Für die Ausbeute an C_2 Kohlenwasserstoffen bestehen intrinsische Grenzen: gebildetes Ethan und Ethen wird durch Radikale zersetzt, welche Methan aktivieren ($OH^\bullet$, $H^\bullet$, $HO_2^\bullet$) oder aber für die C_2 Bildung selbst verantwortlich sind, nämlich Methyl, welches vom erwünschten Produkt Wasserstoffatome abstrahieren kann. Aufgrund dieses Ergebnisses kann man festhalten, dass die Funktion eines effektiven Katalysators nicht nur darin bestehen müsste Methylradikale zu erzeugen, sondern er sollte auch als Plattform dienen auf der diese dann kombinieren können. Reaktionsbedingungen für eine technisch brauchbare OCM wurden anhand des Modells von Dooley et al. [1] ermittelt. Diese Modellparameter wurden gesetzt: ein C/O Äquivalenzverhältnis von 2 bis 8, eine Gastemperatur von 800 K bis 1550 K und ein Druck von 1 bis 10 bar. Vorrausgesetzt eine hohe kombinierte C_2 Selektivität – auf Kosten des Umsatzes – ist gewünscht, so ergibt sich, dass ein hohes C/O Verhältnis von 8 und hohe Drücke günstig sind. Falls umgekehrt eine möglichst hohe Ausbeute von C_2 erziehlt werden soll, so muss das C/O Verhältnis niedrig sein; der Druck muss auch hier möglichst hoch sein, d.h. über 5 bar liegen.

List of Figures

List of Tables

Nomenclature

Symbol	Units	Description
A	$s^{-1} \cdot m^{3(n-1)} \cdot mol^{-(n-1)}$	Pre-exponential factor
C	$mol \cdot m^{-3}$	Molar concentration
c	$J \cdot K^{-1}$	Heat capacity
D	$m^2 \cdot s^{-1}$	Mass diffusion coefficient
E	$kJ \cdot mol^{-1}$	Activation energy
F	$mol \cdot min^{-1}$	Molar flow rate
F	–	Broadening factor
G	J	Gibbs free energy
H	J	Enthalpy
h	$W \cdot m^{-2} \cdot K^{-1}$	Heat transfer coefficient
I	A	Filament current
J	$J \cdot cal^{-1}$	Joule constant
$\dot{J}$	$mol \cdot m^{-2} \cdot s^{-1}$	Diffusive flux
K	–	Partition coefficient; Equilibrium constant
k	$s^{-1} \cdot m^{3(n-1)} \cdot mol^{-(n-1)}$	Reaction rate constant
L	m	Reactor length
λ	$W \cdot m^{-1} \cdot K^{-1}$	Thermal conductivity
μ	$J \cdot mol^{-1}$	Chemical potential
μ	$Pa \cdot s$	Dynamic viscosity
ν	–	Stoichiometric coefficient
Ω	–	Lennard-Jones parameter
p	bar, atm	Pressure
R	$J \cdot mol^{-1} \cdot K^{-1}$	Universal gas constant
ρ	$kg \cdot m^{-3}$	Density

r	m	Radius
r	$\mathrm{mol} \cdot \mathrm{m}^{-3} \cdot \mathrm{s}^{-1}$	Specific production rate
S	$\mathrm{J} \cdot \mathrm{K}^{-1}$	Entropy
s	–	Sensitivity coefficient
σ	Å	Collision integral for diffusion
τ	s	Space time
T	K, °C	Temperature
u	$\mathrm{m} \cdot \mathrm{s}^{-1}$	Axial velocity
v,	$\mathrm{m} \cdot \mathrm{s}^{-1}$	Radial velocity
V	m^3	Reactor volume
$\dot{V}$	$\mathrm{mln} \cdot \mathrm{min}^{-1}$	Volumetric flow rate
W, M	$\mathrm{g} \cdot \mathrm{mol}^{-1}$	Molecular weight
$\dot{\omega}$	$\mathrm{mol} \cdot \mathrm{m}^{-3} \cdot \mathrm{s}^{-1}$	Rate of production of gas phase species

Subscripts

a	Activation
BL	Boundary layer
f	Final; Forward
GP	Gas phase
H	Hydraulic
i	i^{th} species
j	j^{th} reaction
r	reverse
w	Wall
0	Inlet

Abbreviations

BHS	Back Heat Shield
CFD	Computational Fluid Dynamics
CPO	Catalytic Partial Oxidation of Methane
CSFM	Cylindrical Shear-Flow Model

DMTM	Direct Methane Conversion to Methanol
FHI	Fritz Haber Institute, Berlin
FHS	Front Heat Shield
GC	Gas Chromatograph
LFL	Lower Flammability Limit
LOC	Limiting Oxygen Concentration
MFC	Mass Flow Controller
MS	Mass Spectrometer
MTB	Methane to Benzene
MTG	Methane to Gasoline
MTO	Methane to Olefin
OCM	Oxidative Coupling of Methane
PFR	Plug-Flow Model
PID	Proportional Integral Derivative Controller
QMA	Quadrupole Mass Analyser
RMG	Reaction Mechanism Generator
RPA	Reaction Path Analysis
SEM	Scanning Electron Microscope
SSITKA	Steady State Isotopic Transient Kinetic Analysis
STY	Space-Time Yield
TAP	Temporal Analysis of Products
TCD	Thermal Conductivity Detector
UFL	Upper Flammability Limit

Chapter 1

Introduction

Crude oil is a valuable raw material for production of a vast variety of chemicals and transportation fuels. The 20th century can rightly be named the "oil era". However, the proven reserves of crude oil foresee its inevitable fast depletion, and this fact forces humanity to search for other raw materials for the petrochemical industry. One of the alternative raw materials could be natural gas, especially taking into account that the proven natural gas reserves exceed those of crude oil [21]. The annual world energy statistical review done by British Petroleum Corporation in the year 2011 [22] reported that the ratio of proven natural gas reserves to current production (R/P ratio) in 2010 was sufficient to meet 58.6 years of global production. Moreover, the Energy Outlook 2030 statistics and prediction as shown in Figure 1.1 states decrease of oil and increase of natural gas consumptions. Apart from the conventional natural gas sources, as those extracted from a gas-well or above-oil gas, there is also the unconventional source represented by the shale gas. Estimated reserves of the latter are reported to be large and be able to compensate for being-depleted conventional sources [23].

Advantage with high volumes of the available natural gas reserves is shadowed by disadvantage that those reserves are often found in remote areas, away from infrastructure facilities, and this requires natural gas liquefaction for easier transportation, with liquefaction, on its turn, being very costly due to necessity to use low temperatures (ca. -160 °C at maximum transport pressure set around 25 kPa/3.6 psi). For this reason, on-site conversion of natural gas either into easier transportable liquids or into more valuable base chemicals for petrochemistry

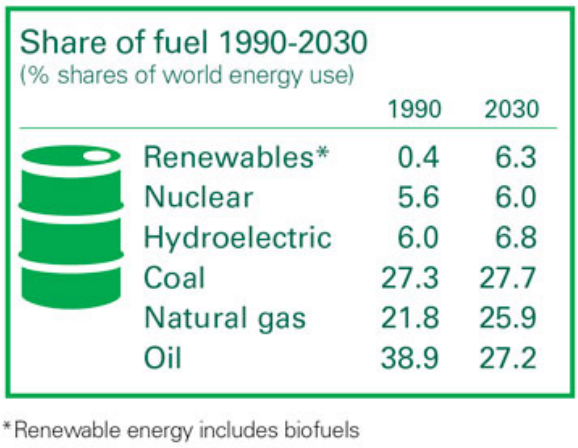

Share of fuel 1990-2030
(% shares of world energy use)

	1990	2030
Renewables*	0.4	6.3
Nuclear	5.6	6.0
Hydroelectric	6.0	6.8
Coal	27.3	27.7
Natural gas	21.8	25.9
Oil	38.9	27.2

*Renewable energy includes biofuels

(a)

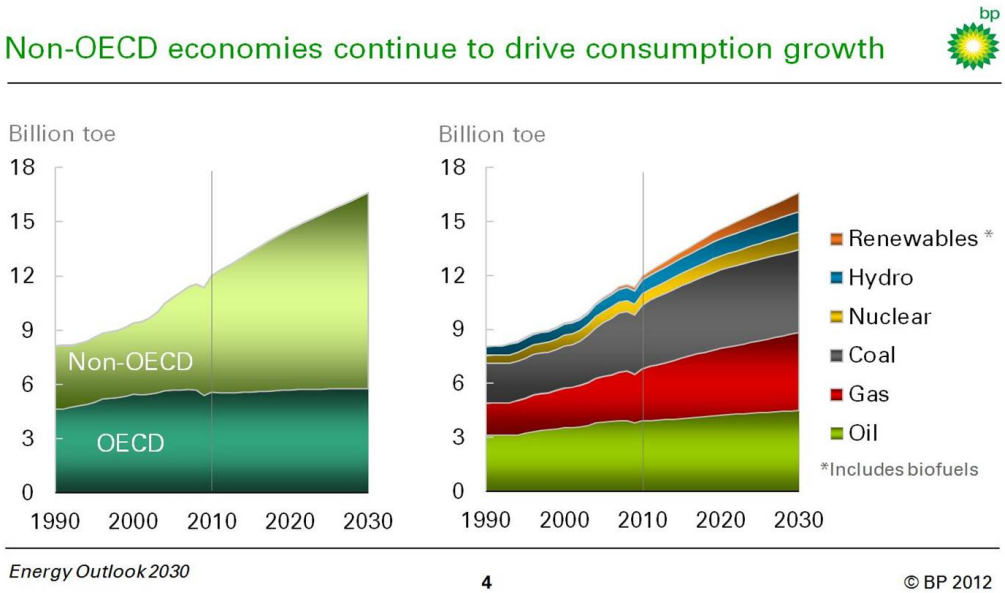

(b)

Figure 1.1: Data from 'British Petroleum World energy review 2011': (a) Outlook for percent share of world energy use by the year 2030; (b) Tendency for the rate of consumption of various energy sources between 1990 and 2030. The unit "toe" signifies tons of oil equivalent.

(so-called Value-Added Products) is of high practical interest. This conversion primarily concerns methane, as it is the far-dominant component of natural gas.

There are several major implemented/potential technologies for methane conversion into value-added products. Catalytic steam reforming for production of synthesis gas is currently one of the largest commercialised process for methane conversion into synthesis gas. Synthesis gas can also be produced by partial oxidation of methane with oxygen, either catalytically (CPO), or non-catalytically with the Shell Gasification Process (SGP). The combination of partial oxidation with steam refoming is known as the autothermal methane reforming (ATR), a technology pioneered by Haldor Topsøe A/S [24].

The obtained synthesis gas is a feedstock for conversion into synthetic fuels directly by Fischer-Tropsch process, or indirectly via methanol-to-gasoline (MTG) or methanol-to-olefins (MTO) processes. Lately a revived interest arose on direct dehydroaromatization of methane to benzene (MTB) [25]. Another possibility is direct methane pyrolysis to ethane and ethene, typically carried out at temperatures higher than 1500 K [26]. Also methane conversion into ethane and ethene, but at lower temperatures, can be achieved with the usage of oxygen, in a process called oxidative coupling of methane (OCM). Among others, the direct conversion of methane to methanol (DMTM) can be mentioned [27].

At the same time, in view of the remote location of natural gas extraction sites, steam/autothermal reforming of methane is not attractive, because reformers are themselves large plants not suitable for on-site processing. Catalytic partial oxidation may require a more compact technological line, but the necessity to use pure oxygen as the reagent and high pressures renders this process unsafe. Non-catalytic methane partial oxidation, on the other side, proved to be viable economically: for example, the largest gas-to-liquids (GTL) process plants currently are based on non-catalytic partial oxidation (on SGP). However, the high reaction temperatures of non-catalytic partial oxidation (typically 1573-1773 K [28]) force still to look for cheap CPO catalysts to reduce operation temperatures. Methane pyrolysis to C_2 products (ethane and ethene) has the disadvantage of not only application of rather high temperatures, but of also thermodynamic equilibrium limitation on C_2 yield. The same drawback of thermodynamic limitation applies for methane-to-benzene process as well. Introduction of oxygen to a reaction sys-

tem allows to overcome equilibrium barriers. For example, a yield in oxidative coupling of methane is not restricted thermodynamically, although conversion of C_2 hydrocarbons to carbon oxides is favoured by thermodynamics.

Out of these above-mentioned processes the OCM seems to be a promising one for investigations. From one point, novel reactor concepts could increase C_2 product yields to a levels acceptable for industrial application. Thus, a practical research interest exists for OCM. It has been speculated since long that OCM can occur with and without a catalytic material in a reactor [29]. In the case of a catalytic OCM there is a complex interaction between the heterogeneous and homogeneous reactions in realm of typically high temperatures. Universal agreement among various research groups on a specific catalytic active centre(s) of methane activation and detailed heterogeneous-homogeneous network of reaction pathways on an atomic scale has not been reached up to the present moment. Elucidation of exact reaction pathways thus constitutes a fundamental research interest in OCM.

Elucidation of detailed heterogeneous-homogeneous network of OCM reaction pathways represents a task of extreme complexity, especially in light of lack of unambiguous proof on the nature of the catalytic active centre(s). In this regard, concentrating efforts on revelation of only homogeneous reaction pathways offers less complexity for investigation. Detailed knowledge of homogeneous reaction pathways carries both fundamental and practical interest, since from wealth of available OCM literature it is already clear that catalytic and gas-phase reactions are intrinsically linked and occur in accord [30; 31], so that tailoring the catalytic properties based on detailed knowledge of gas-phase chemistry could bring the OCM process closer to industrial realisation.

Revelation of detailed homogeneous network of elementary reaction pathways is normally done through experimentation and microkinetic modeling of the chemical reaction. From survey of available literature it became obvious that a complete agreement between experimental and modeling results has not been achieved so far [32]. This disagreement can have happened due to either an incorrect microkinetic model or experimental data with low informative level. Hence experimental data of high informative level could be a better means to validate a microkinetic model. Armed with the aim of obtaining data with high informative

level, in this thesis a study of gas-phase OCM in an empty reactor was carried out using the spatially resolved profile reactor developed within the research group in which this thesis was written. Moreover, an attempt to understand the gas-phase OCM data on an atomic scale was committed through microkinetic modeling of the experimental data. Overall, the following tasks were set and solved in this thesis:

- Measurement of spatially resolved species profiles and temperatures in the reaction of gas-phase OCM under high temperatures and pressures;
- Microkinetic modeling of the obtained spatially resolved species profiles and temperatures with the major microkinetic models – developed either for homogeneous hydrocarbons combustion or homogeneous OCM – available in literature;
- Analysis of the applied microkinetic models and recommendations for their improvement on the basis of their performance for various experimental conditions of the thesis.

Scientific novelty of the work is contained in conduction for the first time a gas-phase measurement using the reactor concept different from other concepts like batch, tubular flow, continuously-stirred tank reactors offering analysis of the inlet and outlet data only. Another novelty of the thesis is application of the known microkinetic models to the experimental data that was not known before.

The thesis is presented on d A4-formate pages of printed text and contains 44 Figures, 4 Tables, and includes: **Abstract**; **Acknowledgements**; **Introduction** describing topicality of the thesis; **Chapter 2** that overviews some aspects of methane oxidation, literature review on methane oxidation, particularly on oxidative coupling of methane in gas phase, and aims of the thesis based on literature review; **Chapter 3** presenting experimental materials, techniques and procedure applied in this thesis; **Chapter 4** describing modeling work having been conducted; **Chapter 5** where main results are presented and analysed and conclusions being made out of them; **General Conclusions** section with summarised conclusions from the overall thesis; **Appendix** section in which supporting information such as scripts for various software, plots for calculations done

in this thesis are given; and lastly, **References** listing literature sources cited in the thesis.

Chapter 2

Literature Review and Aims of This Work

2.1 Aspects of Gas-Phase Methane Oxidation

Thermal dehydrogenation (pyrolysis) of methane with subsequent formation of ethylene/acetylene/carbon requires high temperatures ($\approx$ 1500 K [26]), mainly due to high C-H bond energy of 439 kJ mol^{-1} in methane [33]. This value of high temperature can be lowered with the use of molecular oxygen as the reactant, i.e., by oxidation of methane. Pitchai and Klier [34] pointed out that partial oxidation of methane to products such as formaldehyde, methanol or C_2 hydrocarbons is favoured thermodynamically, as can also be seen from the thermochemical data [20] in Table 2.1. Since long it has been known that fuel-rich oxidation of methane in the gas phase without a catalyst can give yield to variety of products, such as those listed in Table 2.1, with the yields to hydrocarbons compared to CO_x products always observed to be low [35; 36]. It is also known that ignition temperatures for gas-phase methane oxidation are lower than temperatures for methane pyrolysis.

A number of authors [30; 34; 37; 38] studied methane oxidation with oxygen in the temperature range from 350 to 750 °C. According to their results, at temperatures of 300 – 650 °C, methanol, formaldehyde and CO represented the main products, while at temperatures exceeding 650 °C, C_2H_6, C_2H_4, C_3H_6 and

Table 2.1: Reaction Gibbs free energies and enthalpies for methane oxidation. Table after Kee et al. [20]

	$\Delta G^0_{r,298}$ kcal $\cdot$ mol^{-1}	$\Delta H^0_{r,298}$ kcal $\cdot$ mol^{-1}
$2CH_4 + O_2 = 2CH_3OH$	-26.7	-30.2
$CH_4 + O_2 = CH_2O + H_2O$	-68.7	-67.6
$4CH_4 + O_2 = 2C_2H_6 + 2H_2O$	-15.3	-21.0
$2CH_4 + O_2 = C_2H_4 + 2H_2O$	-34.3	-33.6
$2CH_4 + 3O_2 = 2CO + 4H_2O$	-129.9	-124.1
$2CH_4 + 4O_2 = 2CO_2 + 4H_2O$	-191.3	-191.7

C_3H_8 predominated. This latter range of products at above 650 °C was not observed from experiments in this thesis, as will be discussed later. In terms of pressure, the other situation is observed: apart from CO_x, formaldehyde is the principal product of gas-phase methane partial oxidation at atmospheric pressure, with only traces of methanol, whereas at high pressures (50-150 atm) significant methanol yields are observed [34; 35; 39].

In the abovementioned works there is a common conclusion from the authors that low-temperature ($300-650$ °C) gas-phase oxidation of methane with oxygen follows a free-radical chain mechanism with degenerate branching. The overall process, akin to other radical-chain gas-phase reactions, is presumed to consist of 4 steps: a) initiation; b) propagation; c) branching (not always present); d) termination.

The initiation step involves formation of a reactive free radical from a stable molecule, e.g., like in R-n 2.1. The initiation step of this particular reaction of methane activation has a rather high activation energy of 230 to 260 kJ/mol, and is viewed to be the first and rate-limiting step in gas-phase methane oxidation [29]. In the chain propagation step(s), the reactive intermediate species react with stable species forming another reactive species, as in R-n 2.2. This is normally a fast step(s), and the radicals are known as chain carriers. Rapid increase in number of chain carriers may lead to a deflagration or to explosion, with the characteristic S-shaped time-conversion curves. Semenov [40] provided a theoretical and kinetic explanation for the resulting S-shaped time-conversion curves, in the study known as the theory of thermal explosions.

In the chain-branching step(s), a reactive species reacts with a stable species forming two reactive species, exemplified by R-n 2.3. In the chain termination step(s), a stable species is formed from two reactive intermediates, as is shown, for instance, by R-n 2.4. For example, generation of a flame in combustion is due to branching reactions predominating over termination reactions, with intensive formation of radicals resulting in decomposition of a fuel [3].

$$\text{Initiation} \quad CH_4 + O_2 \rightarrow CH_3^\bullet + HO_2^\bullet \tag{2.1}$$

$$\text{Chain propagation} \quad CH_3^\bullet + O_2 + M \rightarrow CH_3O_2^\bullet + M \tag{2.2}$$

$$\text{Chain branching} \quad CH_3O_2^\bullet + CH_4 \rightarrow CH_3O^\bullet + OH^\bullet + CH_3^\bullet \tag{2.3}$$

$$\text{Termination} \quad 2CH_3O_2^\bullet \rightarrow CH_2O + CH_3OH + O_2 \tag{2.4}$$

Typical species responsible for branching are reported to be CH_3OOH, H_2O_2, and CH_2O [30; 41]. The intermediate species responsible for branching react more slowly than the free radicals, therefore a certain induction time (ignition delay time) can be observed before the temperature increases rapidly and explosion occurs. This behaviour is contrasting with purely thermal explosion processes which are based on chain-propagation steps, when the temperature increases at once. Fig. 2.1 shows the difference.

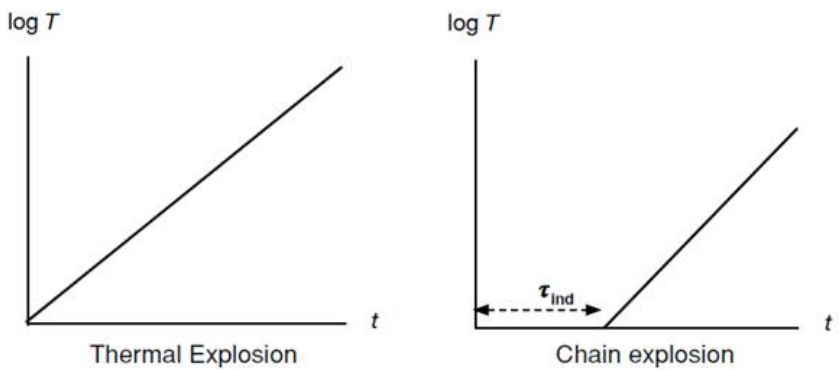

Figure 2.1: Simplified time behaviour of thermal and chain-branching explosion in an adiabatic system. τ_{ind} denotes the induction period. Figure from Warnatz et al. [11].

During the ignition delay time, the content of the radical-pool increases at

an exponential rate. Yet at the same time, the amount of consumed fuel, and hence the amount of released energy, is still too small to be detected. For this reason, the temperature during the induction time remains nearly constant while important chemical reactions (chain branching, formation of radicals) take place. Finally, the radical pool becomes large enough to consume a significant fraction of the fuel. The precise formulation of the induction period depends on the criterion used (consumption of fuel, formation of CO, formation of $OH^{\bullet}$, pressure increase in a constant-volume vessel, temperature increase in an adiabatic vessel, etc.). The length of the induction period is reduced in accordance with kinetic rules by increasing system pressure and temperature. [11].

As can be seen from the R-n 2.3, methylperoxy radicals, $CH_3O_2^{\bullet}$, commence a chain mechanism involving CH_3OOH, which in turn are the precursors of oxygenates. The main reason for products distribution towards oxygenates or $C_2 - C_{2+}$ hydrocarbons depending on temperature is said to lie in the distribution of methylperoxy radicals [42]. Due to the weak O–O bond in CH_3OOH, it is dissociated easily as R-n 2.5:

$$CH_3OOH \rightarrow CH_3O^{\bullet} + OH^{\bullet} \tag{2.5}$$

At 300 °C, for example, this dissociation is reported to be fast, resulting in high rates of oxidation. However, with temperature increase the rate of alkylhydroperoxide dissociation begins to decrease due to increase of the reverse rate of R-n 2.2:

$$CH_3O_2^{\bullet} + M \rightarrow CH_3^{\bullet} + O_2 + M \tag{2.6}$$

At even higher temperatures (above $600 - 650$ °C), the rate of initiation (R-n 2.1) starts to rise again. Finally, the authors conclude that at temperatures of about 900 °C and above the reactions of alkylperoxy radicals or organic peroxides are totally irrelevant.

Another author Mackie [43] in his review introduces the equilibrium constant for R-n 2.2, showing that the ratio of alkylperoxy and alkyl radicals $[RO_2]/[R]$ is directly proportional to pressure and inversely proportional to temperature. Mackie on the basis of the mentioned equilibrium constant calculations suggested that, for example, methylperoxy radicals in particular must be considered in a

mechanism for methane partial oxidation carried out below 750 °C. On application of the equilibrium constant for OCM reaction he suggested that at temperatures above 750 °C and pressures $\leq$ 10.13 bar reactions of methylperoxy radicals can be omitted.

Various types of reactor wall materials were shown to appreciably influence the induction period [44; 45; 46], especially at high pressures. For this reason, some authors, like [47; 48], included, for example, the R-n 2.4 as the deactivation of $CH_3OO^{\bullet}$ radicals on the reactor wall into their microkinetic models of methane oxidation at high pressures (50 bar and higher), with a recommendation to include the deactivation steps for other major radicals as well. The presence of high-surface-area filling materials in the reactor (broken glass, quartz chips, ceramics, etc) is reported to reduce the oxidation rate by chain termination [49] and by causing intermediates react in a non-branching way [37]. At the same time, gas-phase reaction picture was also reported not to have changed when, for example, reaction in an empty quartz reactor or a quartz reactor filled with quartz chips were compared [50].

Most of the above studies of methane oxidation were done in laminar premixed flames, when the fuel and oxidiser are premixed before oxidation and the flow is laminar [3]. Premixed laminar flames are characterised by a fuel-to-oxidiser equivalence ratio, Φ, which is the ratio of moles of a fuel to the mole of an oxidant. If the fuel and oxidiser consume each other completely, forming only carbon dioxide and water, then $\Phi = 1$, and the flame is called stoichiometric. If there is an excess of oxidiser, the flame is called fuel-lean (Φ less than 1); in contrast, if there is an excess of fuel, the flame is called fuel-rich (Φ more than 1). If combustion is fuel-rich, then fuel fragments may collide to form larger hydrocarbons. This process leads to formation of soot, which are agglomerated solid particles. In a hot flame, soot radiates intensely, imparting fuel-rich flames their characteristic yellow colour.

For gas-phase oxidation of hydrocarbons, Warnatz [51] classified two regimes of reaction: radical-poor and radical-rich regime. In the radical-poor regime the overall reaction chemistry is strongly influenced by the rates of chain-initiating

steps, as, for instance by R-ns 2.1, 2.7:

$$CH_4 + M \rightarrow CH_3^{\bullet} + H^{\bullet} + M \tag{2.7}$$

In this case the chemistry is determined by the competition of chain-branching and chain-terminating processes, while radical-radical reactions are unimportant. Whereas in a fully developed combustion reaction radical-radical processes play a key role, in the radical-poor regime the chemistry is little influenced by such radical-radical processes. In the radical-poor regime the chain-terminating steps are also important, such as R-n 2.8:

$$2HO_2^{\bullet} \rightarrow H_2O_2 + O_2 \tag{2.8}$$

The radical-poor regime is pertinent to fuel-rich stoichiometries (in particular at $CH_4 - O_2$ ratios from 2/1 to 20/1, as pointed out by Warnatz [51]) at low methane conversions (with longer ignition-delay times). In this regard, OCM is a typical example of a reaction at the radical-poor, fuel-rich stoichiometry.

To the radical-rich regime Warnatz [51] ascribes fast rates of oxidation and propagation of a flame front. He also notes that very important to this regime are the propagation reactions in which the radicals $H^{\bullet}$, $OH^{\bullet}$, $O^{\bullet}$, $HO_2^{\bullet}$ attack a hydrocarbon. Lastly, the author points out that the radical-rich regime is encountered in stoichiometric or moderately fuel-rich oxidation at significant methane conversion levels.

Asami et al. [52] with R-ns 2.9, 2.10 tried to explain influence of an above-atmospheric pressure and of a third body molecule: promotion of methyl radical formation (bimolecular initiation of the chain) with pressure increase, and stabilisation of vibrationally excited molecules by a third body. For instance, if stabilisation of excited ethane by a third body M does not proceed effectively, the excited ethane is likely to decompose back to methyl radicals quickly because of its excess energy, which is enough to dissociate the carbon-carbon bond. Their C_2 hydrocarbons yield at 1.1 MPa was much higher than that at 0.6 MPa, even when the residence time of the reactant gases in the reaction zone was kept at the same level for the two cases, indicating higher rate of collision with a third

body M with pressure increase.

$$CH_3^{\bullet} + CH_3^{\bullet} \leftrightarrow CH_3 - CH_3^{*} \tag{2.9}$$

$$CH_3 - CH_3^{*} + M \leftrightarrow CH_3 - CH_3 + M^{*} \tag{2.10}$$

Importance of the presence of a third-body molecule, like helium diluent, and, in general, of a gas phase surrounding a catalytic material is also discussed in the study of van Kasteren et al. [53], who noted increase of C_2 hydrocarbons selectivity with increasing helium concentration.

2.2 Gas-Phase Oxidative Coupling of Methane

The seminal point for OCM research is usually ascribed to the work of Keller and Bhasin [54], who observed that methane was converted into a mixture of C_2 hydrocarbons, carbon oxides and water on the catalyst when the reactor was operated in a cyclic mode: the metal oxide catalyst was reduced by feeding pure methane, and then oxidized with oxygen in an alternating manner. Cyclic mode was applied to minimise secondary oxidation of C_2 products.

For some time after this work it was declared that OCM is a typical example of a gas-phase chain reaction catalysed by a solid [55; 56], i.e., methane dimerisation reaction is claimed to occur in the gas phase via surface-initiated methyl radicals. This statement largely came from attempts to identify active centres of methane activation in a catalytic OCM, for example the Li^+/O^- centre on a model Li/MgO catalyst surface was reported to be the active centre [57], with further conclusion that the homogeneous and heterogeneous reaction steps of a catalytic OCM are intrinsically linked, this linkage being that methyl radicals are generated on a catalyst surface with further desorption into the gas phase with subsequent coupling to ethane in the gas phase [58; 59]. However, unambiguous agreement on this active centre was not reached: in the work of Myrach et al. [60] the Li^+/O^- centre was not found experimentally, and its absence was rationalised after theoretical calculations. Thus, no definite answers regarding the active centre even on one model catalyst system was reached. For this reason, as noted in

the Introduction section, it seems more reasonable to concentrate on gas-phase chemistry only as a system of less complexity than a catalyst-gas system.

The article of Lane and Wolf [50], in which they conducted OCM experiments at atmospheric pressure, represents one of the early examples of the overall trends of gas-phase OCM, such as decrease of C_2 hydrocarbons selectivity with increase of methane conversion. They summarised the works of other authors on methane combustion and concluded that the rate-limiting steps (breaking of the first C–H bond in methane) in both the gas-phase and catalytic OCM have the same apparent activation energies of about 55 kcal/mol, thereby underlying inherent importance of gas-phase reactions in case of catalytic OCM. Their gas phase experiments were conducted in a fused silica, high-purity alumina, and stainless steel tubular reactors of 0.95, 0.95, and 10.8 cm I.D., respectively, all of the reactors having 15 cm heated length. The gas phase and catalytic study of Martin et al. [61] performed in a 0.35 cm I.D. quartz tube also shows the main features of OCM, namely in that the main carbon-containing product in the gas phase is carbon monoxide, whereas a catalytic reaction produces carbon dioxide as the dominating product. In both gas-phase and catalytic OCM they showed that ethane is the precursor of ethylene, and proposed that carbon monoxide most likely originates from ethylene oxidation from 600 °C onwards.

Several groups explored the effect of pressure on homogeneous gas-phase OCM through experimental work [30; 52; 61; 62]. Also comparison of gas-phase and catalytic OCM, or concentration on gas-phase chemistry during catalytic OCM at above-atmospheric pressures, were communicated by another group of authors [31; 63; 64; 65]. Studied pressure for gas-phase OCM was atmospheric [61], 4–6 [63], 10 [62], 16 [52] and ultimately 40 bar [30]. Experimental reactors in these works were made of quartz and varied in inner diameter from 3.5 mm [61] to 8 mm [62; 63]. The common findings of these groups were that the rates of the gas-phase reactions increase rapidly with increasing pressure, and that contribution of gas-phase chemistry to overall yield can be reduced by increasing the linear flow velocities of the reactants. Ekstrom et al. [63], for instance, compared the catalysed and non-catalysed OCM, remarking that the rates of the catalysed and blank reactions have different pressure dependencies, making the blank reactions prevailing over the catalysed ones at higher pressures and low linear

velocities (less than 15 cm/s). Moreover, Hutchings et al. [31] credited the gas-phase reactions with notable strength when compared with the catalytic reactions at elevated pressures after observing similar target C_2 products yields regardless of catalyst presence in the gas phase. In addition, a gas-phase reaction inhibition mechanism based on the double role of MgO surface which is simultaneously a source and adsorbent of active species leading to methane coupling products was proposed [64; 65].

Gas-phase methane oxidation, or in particular gas-phase OCM, experiments at above-atmospheric pressure, followed by microkinetic modeling of the experimental data, have been reported in several publications [62; 66; 67; 68]. To mention some of them: Hunter et al. [68] performed experiments at 6.08–10.13 bar in a 24 mm I.D. and 28 mm O.D. quartz tube and developed a model for OCM describing the obtained experimental data. Based on a reaction mechanism developed for methane oxidation, the authors extended it to include reactions pertinent to lower temperature, elevated pressure conditions, in the end having created a mechanism consisting of 207 reactions among 40 species. Sekine et al. [67] performed experiments at 933–1083 K, up to 12 bar pressure and feed rate of 200 mln $\cdot$ min^{-1} in a 4 mm I.D. stainless steel reactor tube lined with quartz. Subsequently they analysed the reaction network by their model compiled from various databases of molecular kinetics. The work of Geerts et al. [69] follows the same approach, but with gas-phase OCM experiments conducted at 1 bar pressure in a ca. 6 mm I.D. quartz reactor.

Another approach of first creating a microkinetic model for gas-phase OCM and then testing the mechanism for experimental data can be seen in the work of Zanthoff and Baerns [7]. They compiled a microkinetic mechanism with elementary reactions and their parameters taken from several sources and with it simulated several kinetic experiments from literature done within the following conditions: $T = 925-1244$ K, $p = 1-41$ bar, $p_{CH_4}/p_{O_2} = 0.5-40$. No fitting the model parameters to experiments was done. Later Tjatjopoulos and Vasalos [70] did differential reaction path analysis for the model of Zanthoff and Baerns, identifying the dominant creative and destructive channels of major species along the reaction path, thus providing valuable insight into the interaction between selective and non-selective sub-mechanisms.

Intermediate between gas-phase and catalytic chemistry can be considered the article of Qiu et al. [71] who investigated catalytic contribution of the reactor wall materials on OCM at atmospheric pressure. They conducted gas-phase reaction in an empty reactor tube of 6 mm diameter and concluded that the surface of a reactor (regarding the choice of material) plays a role in reaction by affecting some of the gas-phase reaction steps.

Attempts to link homogeneous-heterogeneous microkinetic models for OCM are found in a number of works. Mims et al. [5] created a set of 451 elementary gas-phase reactions with 4 catalytic reactions on Li/MgO. They simulated the effect of elevated concentration of CH_3 radicals desorbing from the catalyst surface on homogeneous CH_3 radicals production rate. The microkinetic model of Sun et al. [9] was also created to link gas-phase and catalytic chemistry on Li/MgO in the plug-flow approximation. The gas-phase chemistry part of their model was published earlier by Chen et al. [62] which consisted of 39 elementary reactions. Geerts et al. [69] and Vedeneev et al. [72] also included the catalytic elementary reaction steps into their gas-phase reaction mechanism, commonly concluding that additional generation of CH_3 radicals by a catalytic surface enhances coupling rate to ethane; at the same time, the rate of reactants conversion is reported to decrease by the Li/MgO catalyst that acts not only as a methyl radical producer, but also as an unselective radical consumer [69], or the enhanced ethane concentration due to a catalyst is annihilated by subsequent gas-phase reactions which do not permit to overcome a certain kinetic limit in C_2 yield [72].

Regardless of the purely experimental, modeling, or a combined approaches, gas-phase oxidation of methane (either stoichiometric combustion or OCM) in terms of the system it was studied in can broadly be summarised as that done in static reactors [41; 73; 74], laboratory flow reactors [68; 75; 76; 77; 78; 79; 80; 81], shock tubes [82; 83; 84; 85; 86], and laminar premixed flames [87; 88; 89; 90; 91].

Table 2.2 contains the overview of the major microkinetic models created for methane combustion, or OCM specifically, which were used in this thesis. In general, these models were tested against experimental data in shock tubes and jet-stirred reactors, measurements of laminar flame velocities, laminar flame species profiles, and ignition delay times. Thermodynamic properties file in the models were compiled either from the Thermochemical Database of Burcat [92],

Table 2.2: Compilation of microkinetic reaction models proposed for gas-phase methane oxidation. Unless specified, "flow reactor" denoted implies a variable-pressure flow reactor.

Model	**Acronym**	**Ref.**	**Optimised for**	**Validated against experiments in**	**Species**	**Reactions**
1	Dooley et al.	[1]	Methyl formate oxidation	Shock tube, flow reactor laminar flames	269	1583
2	Lopez et al.	[2]	Ethylene oxidation	High-pressure flow reactor	62	481
3	Warnatz et al.	[3]	$H_2/CO/C_1/C_2$ combustion	Shock tube, flow reactor	34	158
4	GRI-Mech version 3.0	[10]	Methane combustion	Shock tube, flow, stirred reactor, laminar flames	53	325
5	LEEDS & Eötvös University (Hughes et al.)	[8]	Methane combustion	Shock tube, flow reactor, laminar flames	37	351
6	Konnov Mech version 0.5	[4]	$H_2/CO/C_1$–C_3 combustion	Shock tube, flow reactor	127	1207
7	Sun et al.	[9]	OCM on Li/MgO, gas-phase OCM	Atmospheric flow reactor	25	39
8	Zanthoff & Baerns	[7]	Gas-phase OCM	High-pressure flow reactor	32	164
9	Wang et al. (USC Mech version 2.0)	[6]	$H_2/CO/C_1$–C_4 combustion	Shock tube, burner-stabilised flame, flow reactor	111	784
10	Mims et al.	[5]	OCM on Li/MgO, gas-phase OCM	Atmospheric flow reactor	116	451

Table 2.3: Information on species in the microkinetic models proposed for gas-phase methane oxidation which were used in this thesis. Intermediate species are either radicals or atoms.

Model	**Acronym**	**Ref.**	**Species in total**	**Stable species**	**Intermediate species**
1	Dooley et al.	[1]	269	115	154
2	Lopez et al.	[2]	62	19	43
3	Warnatz et al.	[3]	34	14	20
4	GRI-Mech version 3.0	[10]	53	21	32
5	LEEDS & Eötvös University (Hughes et al.)	[8]	37	14	23
6	Konnov Mech version 0.5	[4]	127	37	90
7	Sun et al.	[9]	25	15	10
8	Zanthoff & Baerns	[7]	32	15	17
9	Wang et al. (USC Mech version 2.0)	[6]	111	91	20
10	Mims et al.	[5]	116	40	76

or from CHEMKIN thermochemistry database [93]. Information on stable and intermediate species in the mechanism of each model is presented in Table 2.3. The mechanism of Dooley et al.[1] is the only one which contains elementary reactions with no influence for methane oxidation, viz. 137 reactions of methyl formate chemistry. The majority of reactions in Dooley et al. mechanism involves formic acid chemistry – 1288 reactions, and in this case the formic acid chemistry influences OCM simulations.

Out of this overview, the microkinetic models of Dooley et al. [1] and Lopez et al. [2] contain pressure dependency and third body efficiencies for specific elementary reactions, and those of Wang et al. [6], GRI 3.0 [10] and Hughes et al. [8] embrace only third body efficiencies without pressure dependencies. On the contrary, the model from Warnatz et al. [3] contains only pressure dependencies (from 0.0253 to 50 bar) without third body efficiencies, although the authors warned that the Arrhenius parameters of the pressure-dependent reactions in their model may not have physical meaning for complex reaction schemes.

2.3 Spatial Profiling

Reaction kinetic measurements are a central part of alkane partial oxidation research. Usually such measurements are done in flow tubular reactors that offer construction simplicity and industrially relevant scale-up perspectives. Normally analysis of species in case of laboratory flow tubular reactors is done at the reactor outlet, i.e., only inlet and outlet parameters are measured. In case of temperature measurements, not only data at the inlet and outlet, but also temperature at only one arbitrarily chosen point between the reactor inlet and outlet can be acquired. This brings up the fact that a laboratory flow reactor remains in the role of a "black box", i.e., when temperature, nature of the intermediates and the conversion/selectivity data in the main body of the reactor (between inlet and outlet) remain virtually unknown.

To disclose such unknown data in the main body of the reactor, transient experiments such as steady-state isotopic transient kinetic analysis (SSITKA) [94] or temporal analysis of products (TAP) [95; 96] can be done. However, high prices of isotopes restrict the widespread use of SSITKA. In case of TAP technique, the vacuum-pressure conditions for creation of diffusion regimes are far from industrially relevant conditions, since kinetics at low pressures and low temperatures is hardly translatable to high-pressure/temperature conditions.

In the design by Dagaut et al. [97; 98], spatial species and temperature profiles are obtained by a sonic quartz probe extending up to 5 mm from the reactor outlet. The gaseous samples are rapidly extracted at low pressure (2–10 Torr) and stored in glass bottles. However, the design with a sonic probe was applied to a spherical jet-stirred reactor of 4 cm diameter, which is far from the tubular flow reactor configuration. To obtain profiles in tubular flow reactors, one of the solutions is to install several discrete sampling points along the reactor axis [68; 99; 100], but usually there are not enough of such sampling points (only 10-15 points) to obtain a sufficiently high resolution of data.

The more practical approach to obtain species profile(s) with a needed high axial resolution can be realised with the help of a thin sampling capillary inserted into the reaction zone, with continuous translation of the capillary along the reaction fluid flow, thereby continuously transferring species under reaction into

an analytical device. As for temperature profile(s), their measurement can be linked to the sampling capillary or by other constructive arrangements.

There are several attempts in literature that realised the spatial profiling technique. Partridge et al. [101] are the authors of the SpaciMS technique, which is a spatially resolved capillary-inlet mass spectrometry system that allows to generate spatially resolved maps of species and temperatures of reactions within catalytic monoliths. They proved that SpaciMS is a highly sensitive and minimally invasive technique that can provide reaction maps as well as catalytic transient behaviour. A review on the development and applications of the SpaciMS technique is also given by Sa et al. [102]. Another example is by Bosco and Vogel [103], who constructed an optically accessible channel reactor with a cell prone to IR thermography for catalyst surface temperature measurement, as well as sample withdrawal with a thin capillary for species analysis. The authors used their designed reactor to study carbon oxides methanation.

The main disadvantage of the abovementioned spatially resolved reactor types is the use of an open-end sampling capillary that might interfere in the overall fluid flow pattern. In the design by Horn et al. [104], who built a spatially resolved profile reactor, the capillary has a closed end, whereas sampling is done by a side orifice such that the capillary channel remains always filled during sampling, avoiding possible flow disturbances or by-passing that might be exerted by an open-end capillary. Their design is applicable to open channels and packed beds, and can also be used for spatially resolved spectroscopy, as documented in the patent [105]. A definitely strong point of the spatial reactor of Horn et al. [104] is the possibility to obtain species and temperature profiles at high pressures and high temperatures.

Horn et al. [104] with their first-generation spatially resolved reactor studied methane partial oxidation on rhodium, and in the second improved-construction generation of the spatial reactor studied (experimentally and numerically) methane partial oxidation to syngas on Rh and Pt [106], on Rh [107], and purely numerical modeling on Rh [108]. Combined investigation of methane partial oxidation on Pt, ethane oxidative dehydrogenation to ethylene on Mo oxide catalysts, as well as gas-phase methane oxidative coupling reported recently [109] is done with the spatial profile reactor of the third generation described earlier by Horn et al. [12].

2.4 Aims of This Work

From the above review of literature sources of gas-phase methane combustion or OCM in particular, it became clear that almost all of the authors who performed their experimental studies in conventional tubular flow reactors, performed them at conditions when only reactor inlet and outlet data were known. Accordingly, they modeled their experimental data, or created microkinetic models, based on the reactor inlet and outlet parameters (species composition, temperature).

By conducting experiments in a spatially resolved profile reactor, in this work it is attempted to obtain the data of high axial resolution in the main body of the reactor. The closest attempt to perform spatially resolved profile measurements was done by Hunter et al. [68] who realised 10 sampling points along a 807-mm-long quartz tube, and by Brezinsky et al. [99] with their 15-sampling-point 100 mm O.D. 1000-mm-long reactor. No other work where gas-phase experimental data of high resolution in tubular flow reactors, with validation of a microkinetic mechanism against that data, except partly some data from the own research published in [109], was encountered.

Also it is seen that the significant number of gas-phase studies in this literature review were done in reactor tubes of small inner diameter, when the wall chemistry might interfere with the gas chemistry, whereas it would be preferable to perform gas-phase experiments in a reactor tube of a large diameter to minimise influence of the wall chemistry. Only in the works of Lane and Wolf [50], Brezinsky et al. [99] and Hunter et al. [68] sufficient reactor tube diameters are observed, which is a scarce amount of reference.

Thus, on account of these key shortcomings in the browsed literature sources, the following aims were defined in this thesis:

- Measurement of spatially resolved species profiles and temperatures in the reaction of gas-phase OCM in a reactor tube of sufficiently large diameter (low surface-to-volume ratio) under typical OCM conditions, viz. carbon-to-oxygen atomic ratios corresponding to fuel-rich methane-oxygen mixtures, pressures from atmospheric to moderately elevated, non-isothermal reactor heating profiles. Elevated pressure for OCM reaction is an industrially relevant condition for integration into existing technological processes;

- Analysis of the experimental gas-phase profiles of species in terms of conversion and selectivity;
- Microkinetic modeling of the obtained spatially resolved species profiles and temperatures with the major microkinetic models available in literature – models which were either optimised for stoichiometric methane combustion (including other hydrocarbon(s)) or for fuel-rich methane oxidation. Modeling is to be based on both the plug-flow and boundary-layer flow reactor models using either experimental gas-phase temperature or oven temperature as one of the input parameters;
- Comparison of the performance of the applied microkinetic models on the basis of their description of the experimental data in the thesis;
- Performing detailed analysis of the selected microkinetic models through sensitivity and reaction path analyses, the latter type of analysis based on relative rates of production of species;
- Comparison of the individual elementary reactions of the selected microkinetic models based on sensitivity analysis;
- Drawing conclusions on performance of the applied microkinetic models, as well as recommendations for their improvement on the basis of their description of the experimental results of the thesis;
- Drawing outlook of the thesis, i.e., recommendations and suggestions for future experimental/theoretical work that arose after fulfillment of research in this thesis.

Chapter 3

Experimental Methods and Procedure

3.1 Spatially Resolved Profile Reactor

3.1.1 Introduction

The main experimental accent in this thesis is on conduction of all the experiments using the spatially resolved profile reactor (also referred here as profile reactor). The concept of the spatially resolved profile reactor is to analyse axial species and temperature profiles inside a heterogeneous (catalytic) or homogeneous (gas-phase) reaction system. The detailed description of the profile reactor is reported by Horn et al. [12], from which Figure 3.1 is taken which sketches the profile reactor without an analysis section. The set-up in general allowed to perform experiments at pressures up to 40 bar (4 MPa), oven temperatures up to 900 °C (1173.15 K), and total feed flows up to 10000 mln$\cdot$min^{-1}, when normal conditions in this thesis are defined as temperature of 293.15 K and pressure of 1 bar (100 kPa). In a general composition the set-up consisted of a feed section, reactor section, and analysis section. More detailed description of each particular section of the profile reactor is given further on.

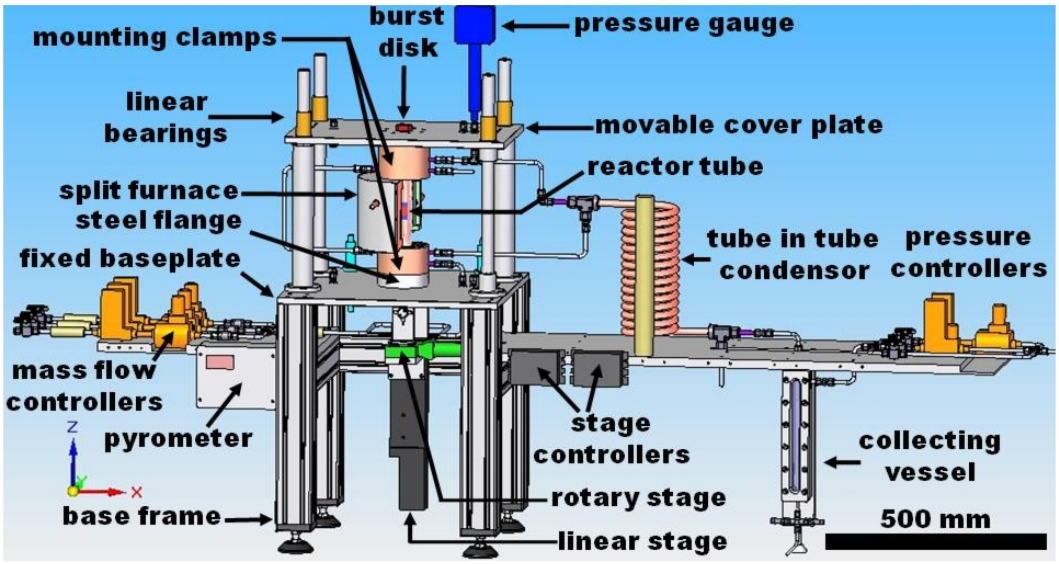

Figure 3.1: Sketch of the spatial profile reactor set-up. Figure adapted from Horn et al. [12].

3.1.2 Feed Section

In the feed section the composition of the feed gases was controlled by a set of thermal high-pressure mass-flow controllers (EL-FLOW, Bronkhorst), pictured in the leftmost part of the sketch in Figure 3.1. The flow of the controllers fluctuated by $\pm$ 5 mln $\cdot$ min^{-1} at highest; calibration of the mass-flow controllers was performed by electronic soap-film flow-meters from HORIBA Corp. Four feed gases were calibrated for the mass-flow controllers (MFCs): methane, oxygen, argon, and 8 vol.% helium in argon mixture. Downstream from the MFCs the gases flew through a one-way valve. All the feed gases were from Westfalen AG with certified 5.0 purity grade for argon and argon/helium mixture, and 4.5 purity grade for methane and oxygen, and were used as purchased. Gas flows from outlets of all three MFCs coalesced into a single feed stainless steel pipe that guided mixed gases to the reactor section. A length of the single feed pipe was sufficient to allow gases mix uniformly before entering the reactor section.

3.1.3 Reactor Section

3.1.3.1 Reactor Vessel

The experimental reactor vessel was a transparent fused silica (quartz) tube of 18 mm inner diameter, 38 mm outer diameter (wall thickness 10 mm), and 205 mm height. This wall thickness was chosen to withstand reaction pressures of at least up to 45 bar. Both ends (22.5 mm each) of the reactor tube were conically shaped, so that the outer diameter was narrowed to 24 mm at the tube edges, whereas the inner diameter remained constant. Specification for impurities from the fused silica tube manufacturer (QSIL AG) included 4.8–7.75 ppm of metals, and 15–45 ppm of thermally stable OH-groups.

The conical parts of the reactor tube were embedded into a pair of water-cooled copper mounting clamps, and the quartz-copper interface was tightly sealed with a vacuum-grade silicon grease to provide pressure-proof conditions. The copper clamps, mounted stationary to alumina cover plates, were constantly cooled to 20 °C during reactor operation. A set of springs (not shown in the sketch) kept the clamps and alumina cover plates tightly sealed with the reactor tube during operation under pressure. The entire reactor section stood on four anchoring legs with bases.

3.1.3.2 Spatial Profiling Part of the Reactor Section

Graphical representation of the spatial profiling part of the reactor section in case of presence of a catalyst was reported by Horn et al. [12], and for the case of absence of a catalyst it is sketched in Figure 3.2.

In the created design, a gas phase or a catalytic media under investigation in the profile reactor tube normally is confined between two reticulated cylindrically shaped $\alpha - Al_2O_3$ foam monoliths (Vesuvius Hi-Tech Ceramics) of tailored porosity and pore diameter. In this work, alumina foams of 80 ppi (pores per linear inch) porosity and 500 μm average pore diameter were used. The struts thickness of these foam monoliths was 100 μm, which is shown in SEM images in [104]. The outer diameter of the foam monolith was slightly less than 18 mm inner diameter of the reactor, therefore the refractory Interam ® mat was wrapped around them for tight insertion into the reactor tube to eliminate any gas chan-

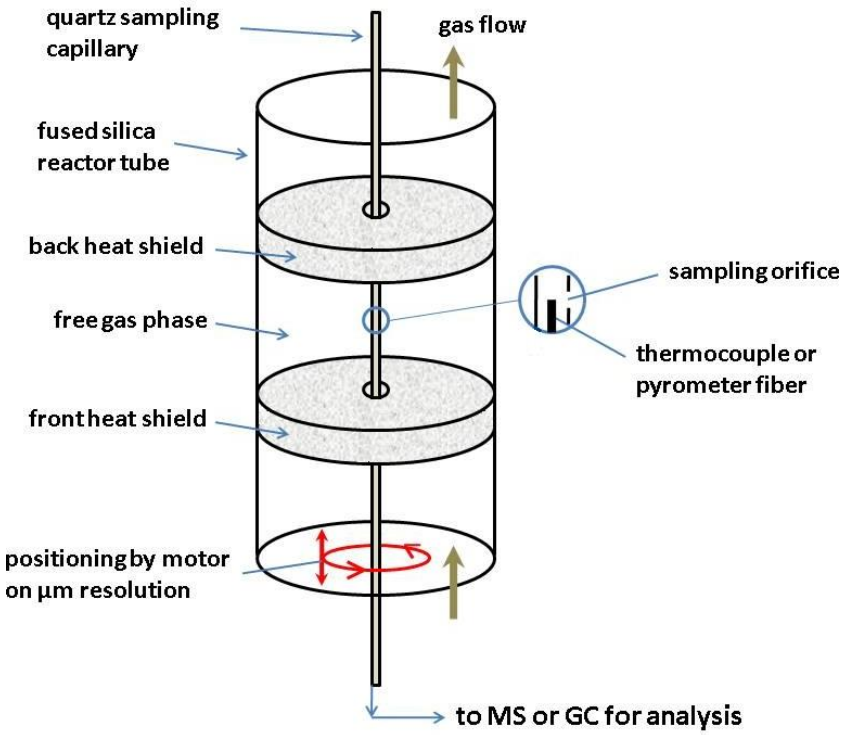

Figure 3.2: Reactor concept for spatially resolved simultaneous profile measurement of kinetic data, gas temperature or solid temperature.

neling possibility. The main functions of the foam monoliths during operation were to support a catalyst in its place, to quantitatively define the homogeneous gas-phase zone, to hold and guide a sampling capillary vertically, to heat up incoming gases, and to provide defined inlet flow pattern (uniform velocity and temperature). Uniformity of the flow pattern is an important required condition for boundary-layer simulations of a reaction in the profile reactor. As the incoming gases flew from bottom to top, the foam that first contacted the incoming gases was titled as 'front heat shield', and the other as 'back heat shield', also abbreviated correspondingly as FHS and BHS.

For measuring high-resolution profiles of gas species and gas/solid temperature, a thin quartz capillary (O.D.=700 μm, I.D.=530 μm, Optronis GmbH) was moved through the axial centerlines of both the reactor tube and foam monoliths. The thin capillary had a laser-drilled sampling orifice of either 25 or 100 μm in diameter located 125 mm below the capillary's upper end that was closed. The

length of 125 mm assured that capillary was always within the drilled axial centerline hole of the foams. The lower end of the capillary was open and connected to a micro-volume stainless steel 4-way cross (1/16" bore, Valco Instruments), which in turn was connected to a stainless steel holder. The stainless steel holder was mounted to a rotary stage, and the rotary stage was mounted to a linear stage. With this arrangement it was possible to move the sampling capillary with a micrometer resolution up and down and to rotate it. Such micrometer-resolved movement was provided by a high-precision motor (M-060 Series rotary stage and M-4036 Series linear stage controlled by C-862 Mercury stage controllers, all from Physik Instrumente GmbH). Rotation of the capillary provided averaging across different scan points; such averaging becomes helpful, for instance, in case of catalytic measurements when some catalyst geometries (e.g., reticulated foams) result in irregular flow patterns across a particular horizontal plane.

To seal the capillary against the ambient conditions, but still to allow movement with a minimum force, the capillary ran through a silicon grease pit located between two stainless steel liners (1/16") which had a slightly larger diameter than the capillary. When the capillary was inserted into these liners, its outer surface picked up a thin grease layer from the pit. The annular gap between the capillary and the steel liners was small enough to withstand maximum reactor operation pressure of 40 bar. Apart from sealing properties, the silicone grease offered smooth movement with least resistance for the relatively fragile sampling capillary.

Gas species sampling was accomplished by means of a transfer line (1/16", made of polyimide, Valco Instruments) connected to one of the exits of the micro-volume stainless steel cross. The transfer capillary served as a connection between sampling quartz capillary and analysis section, and did this connection either directly, or via a membrane pump that evacuated the transport capillary at ca. 5 $\mathrm{mln} \cdot \mathrm{min}^{-1}$ rate. Evacuation procedure was necessary for rapid gas transport to the analysis section, as well as to avoid blocking the transport capillary by condensation of condensable species (e.g., water). A needle valve was placed on the transfer capillary to diminish oversampling at high pressures. Figure 3.4 schematises connection between the reactor and analysis sections.

Profiles of gas temperature can be measured by a thin thermocouple (type

K, Inconel ® 600 sheath material, Thermocoax GmbH) of 340 μm O.D., and profiles of solid-body temperature by a low-OH-level silica fiber connected to a two-wavelength pyrometer (IMPAC Infrared GmbH) of 350 μm O.D. Either of these two temperature sensors were inserted into the sampling capillary until the point when the sensor tip was horizontally aligned with the sampling orifice in order to simultaneously measure the temperature of a being sampled gas species composition (with thermocouple) or of a solid material (with pyrometer). A two-wavelength pyrometer is necessary to account for possible emissivity change along a scan length.

3.1.3.3 Heating, Pressure and Safety Control of the Reactor Section

As can be seen in Figure 3.1, the reactor quartz tube was enclosed along its 160 mm length by a tubular split electric-resistance (DC current) furnace which had 3 horizontally planed circumferential coils uniformly distributed along the 160 mm height of the furnace. The furnace output amounted to maximal 450 W heating power, 1150 °C heating temperature, and its temperature was controlled by a PID controller (Eurotherm 2704, Invensys Systems GmbH). The furnace control thermocouple (type K) was placed in a narrow gap ($\approx$ 3 mm) between the reactor tube and the furnace inner shell. On a vertical plane the control thermocouple was placed in the middle of the furnace height.

Gas flow through the profile reactor was designed to proceed from left to right and from bottom to top of the reactor section. The outlet of the reactor was connected to a tube-in-tube spiral heat exchanger to trap condensable components of a reaction. Condensable components in the liquid form were collected in a reservoir which could be emptied via a needle valve during reactor operation without any pressure loss. The overall reactor pressure was controlled by a pair of pressure regulators (EL-PRESS, Bronkhorst) installed between the heat exchanger and the reactor outlet to atmosphere: one for pressures between 1 and 7 bar, and the other for pressures between 7 and 45 bar. Apart from these two pressure regulators, a third by-pass line could be chosen to operate the reactor at atmospheric pressure. The overall reactor pressure was measured by a digital pressure transducer (model LabDDM, AEP Transducers S.r.l.).

The reactor section was designed to operate with explosive mixtures under high pressures, therefore a number of constructive safety precautions were taken. First, a 1/2" safety burst-disk was installed on the upper copper clamp, vertically above the reactor tube, to instantaneously release pressures higher than maximally limited 45 bar. Secondly, the above-mentioned set of springs allowed the reactor vessel itself to function as a pressure-release valve, as number and strength of the springs between the cover plates determined the leak pressure of the reactor section. Thirdly, to protect an operator in case of reactor explosion, the tubular split furnace surrounding the reactor tube was enclosed in a metal housing, shielded by a safety screen (not shown in Figure 3.1), and continuously filled with nitrogen. Lastly, the molar ratio of methane to oxygen fed through the MFCs was not set below 4 in compliance with the Flammability Limit Diagram for methane-oxygen-nitrogen ternary mixture at 1 bar pressure shown in Figure 3.3.

The diagram is a graphically modified open-source version (http://en.wikipedia.org/wiki/Flammability_diagram) of that reported by Zabetakis [13]. Considering the standard air composition (78 vol.% nitrogen and 21 vol.% oxygen), any proportion of methane and air will lie on the straight blue "air-line" shown in the graph. The upper and lower flammability limits (UFL and LFL) of methane in air are denoted on it as well (they are equal to 15 and 5 vol.% methane in air, respectively). The upper and lower flammability limits of methane in pure oxygen without nitrogen at 20 °C are 5.1 and 61 vol.%, respectively, as one can infer from the diagram. Moreover, from the stoichiometric combustion of methane: $CH_4 + 2O_2 \rightarrow CO_2 + 2H_2O$, concentration of methane in oxygen is 1/(1+2) = 33%. Any stoichiometric mixture of methane and oxygen will lie on the straight line between pure nitrogen (and zero percent methane) and 33 percent methane (and 67 percent oxygen) - this is shown as the red stoichiometric line. The nose of the envelope (red area) defines the limiting oxygen concentration (LOC) of 12 vol.%.

Vanderstraeten et al. [110] derived numerical expressions for pressure (Eq. 3.1) and temperature (Eq. 3.2) dependences of UFL:

$$UFL(p_1) = UFL(p_0)\left[1 + a\left(\frac{p_1}{p_0} - 1\right) + b\left(\frac{p_1}{p_0} - 1\right)^2\right] \tag{3.1}$$

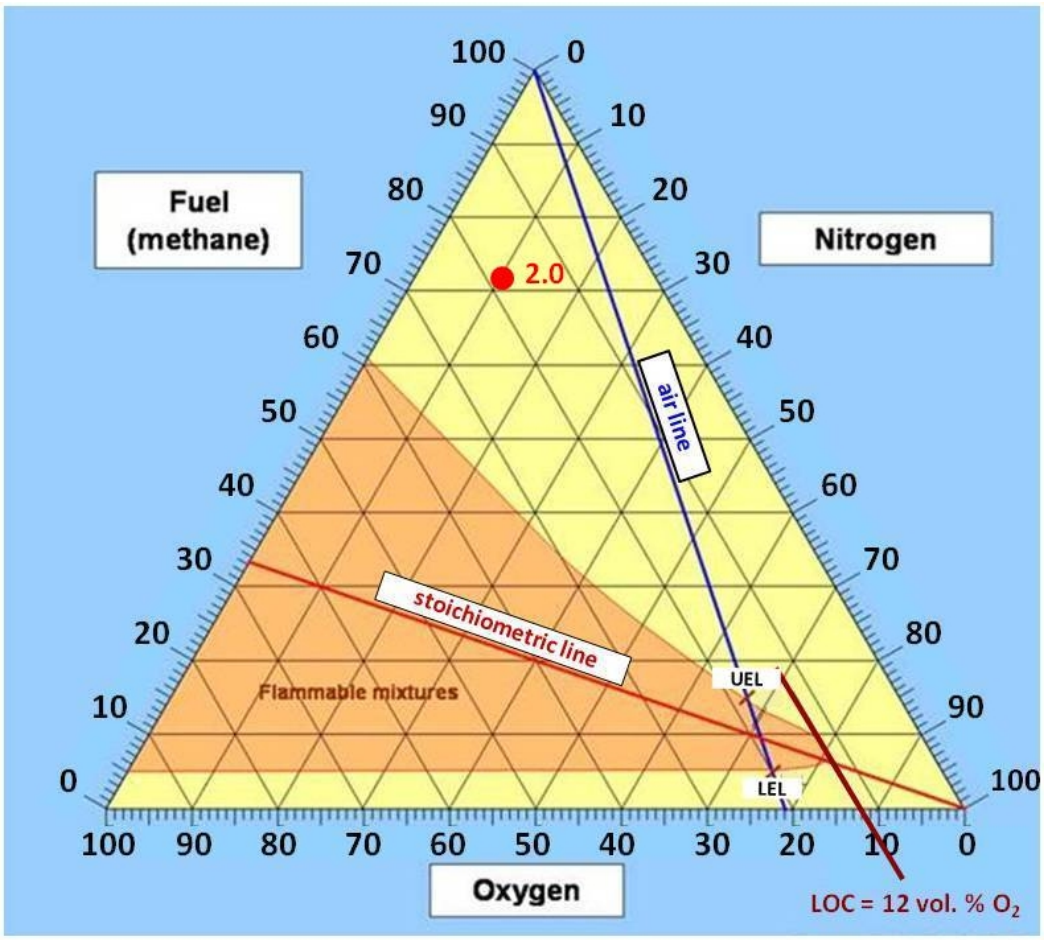

Figure 3.3: Flammability diagram for methane-oxygen-nitrogen gaseous mixture at atmospheric pressure and 20 °C. Upper Flammability Limit (UFL) and Lower Flammability Limit (LFL) are used interchangeably with Upper Explosive Limit (UEL) and Lower Explosive Limit (LEL). Red dot corresponds to C/O ratio of 2.0. Figure is a re-drawn version from Zabetakis [13].

with the coefficients: $a = 0.0466$ and $b = -0.000269$, and where p_i is the pressure of interest, p_0 is 1 bar pressure.

$$UFL(T_1) = UFL(T_0)\left[1 + c\left(\frac{T_1 - T_0}{100}\right)\right] \tag{3.2}$$

with $c = 0.0854$ K^{-1}.

According to these expressions, for example, for a pressure of 1 bar the UFL would increase from 15.7 vol.% to 18.1 vol.% methane in air while increasing the temperature from 25 to 200 °C. At 138 °C the LFL for methane would reduce from 5.1 to 4.4 vol.%. At 4 bar pressure and 72, 18 and 10 vol. percentages of respective methane, oxygen and inert gas, set in this thesis experiments and which corresponded to C/O ratio of 2.0 (red dot in the graph), UFL for methane increased from 61 to 69% and thus the envelope of flammability region became very close to the C/O stoichiometry of 2.0.

3.1.4 Analysis Section

The analysis section consisted of a micro gas chromatograph (Varian 490-GC) equipped with a thermal conductivity detector, and a separate mass spectrometer (Balzers Prisma QME 200) with impact electron ioniser, QMA 200 M2 quadrupole mass analyser and electron multiplier detector. The above-mentioned membrane pump sampled gaseous species into the mass spectrometer at ca. 5 mln $\cdot$ min^{-1} rate at normal conditions. Continuous scanning mode recorded mass spectra at $\approx$ 100 ms time resolution.

The micro gas chromatograph had the following four elution columns: Molsieve 5A (10 metres) for analysis of CH_4, O_2, CO and H_2; PoraPLOT U (10 m) for CO_x and CH_4; Al_2O_3/KClPLOT (10 m) column for C_2–C_4 hydrocarbons; and CP-Sil 5CB (4 m) column for C_3 – C_6 species. Carrier/flush gases provided were Ar (5.0, Westfalen AG) for Molsieve 5A column, and He (5.0, Westfalen AG) for the other columns. Carrier/flush gases were purified from traces of oxygen and water by an adsorber trap (Alphagaz Purifier, Air Liquide) before entering the instrument. Figure 3.4 schematically shows the analysis section.

Detailed description of the functioning principles of the specific components

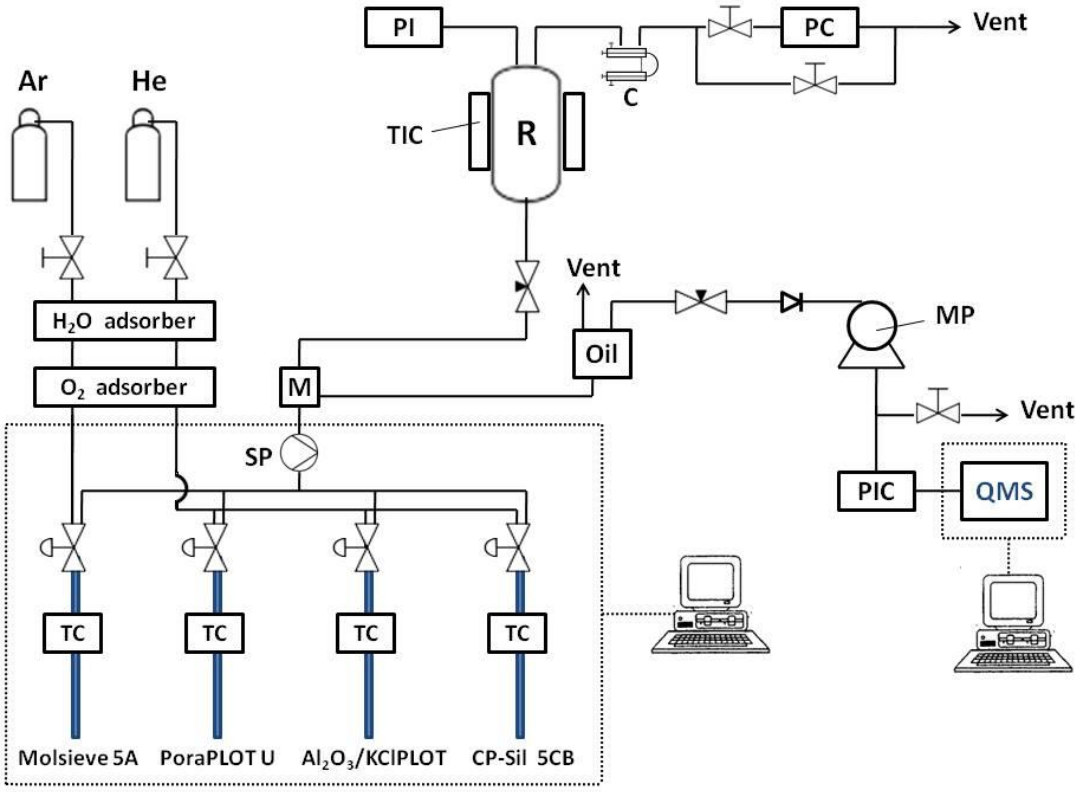

Figure 3.4: Schematic of connection arrangement between reactor and analysis sections. Symbols: **R** - reactor; **TIC/PIC** - temperature/pressure indicator and controller; **C** - tube-in-tube condensor; **M** - water-proof membrane; **SP/MP** - sampling/membrane pumps; **QMS** - quadrupole mass spectrometer.

used in the mass spectrometer and gas chromatograph of the Analysis Section is given in the following sub-sections.

3.2 Mass Spectrometry

Mass spectrometry (MS) is an analytical technique that is used to identify charged particles according to their mass-to-charge ratio. It allows both qualitative and quantitative analysis and is used for determining masses of particles, elemental composition (including isotopic composition), and for elucidating the chemical structures of molecules, such as peptides and other chemical compounds, by

observing their fragmentation pattern. The general principle of the technique is ionisation of chemical compounds to generate charged molecules or molecule fragments and measuring their mass-to-charge ratios. A typical procedure of MS analysis thus includes the following steps:

1. Vapourisation of a sample loaded into MS.
2. Ionisation of the sample with one of various methods available, which results in formation of ions.
3. Separation of ions according to their mass-to-charge ratio (m/z) in a mass analyser by electromagnetic field.
4. Detection of the separated ions.
5. Processing of the detector signal into mass spectra.

Ionisation of a sample can be done by various methods. Electron ionisation, chemical ionisation, field ionisation are applied for gas-phase molecules which are thermally stable. For compounds which are thermally labile but do not have sufficient vapour pressure and are in liquid or solid phase, the direct ionisation methods can be applied. For example, electrospray, atmospheric pressure chemical ionisation and atmospheric pressure photoionisation serve to extract ions which are in solution. In case of a solid-phase ions sources, the analyte is in an involatile deposit, and can be desorbed by irradiation with energetic photons or particles. The desorbed ions can be extracted by electric field and directed to the analyser. Matrix-assisted laser desorption, secondary ion mass spectrometry, plasma desorption, and field desorption employ the latter strategy to provide analyte ions [14].

Electron ionisation, also called electron impact, is a commonly used ionisation technique. Upon bombardment (impact) of a gas-phase molecule by electrons, gas-phase ions are produced [14]:

$$\mathrm{M} + \mathrm{e}^- \rightarrow \mathrm{M}^{\bullet +} + 2\mathrm{e}^-$$

The formed radical cation has odd number of electrons and can fragment to form either a cation with an even number of electrons, or a new radical cation and a

neutral molecule:

$$\mathrm{EE^{+}(Even\ Ion)\ +\ R^{\bullet}(Radical) \longleftarrow M^{\bullet +} \longrightarrow OE^{\bullet +}(Odd\ Ion)\ +\ N(Molecule)}$$

Each secondary ion derived from the primary radical cation can undergo fragmentation, and so on. Most of the positive ions have a charge corresponding to loss of one electron. For large molecules, multiply charged ions can also be obtained. Negatively charged ions can be derived too by electron affinity to the impacting electron at low energies. All these formed ions are separated according to their mass-to-charge ratio, and subsequently detected in proportion to their abundance. Mass-to-charge separation is carried out in a mass analyser.

Mass analysers can roughly be divided into two main classes on the basis of a number of properties. The first class, scanning analysers, transmit the ions of different masses successively along a time scale. To this class belong magnetic sector instruments with a flight tube in the magnetic field, and also quadrupole instruments; both instruments allow only the ions of a given mass-to-charge ratio to go through at a given time. The other class of analysers allow simultaneous transmission of all ions. Among this class are the dispersive magnetic analyser, the TOF mass analyser, the trapped-ion mass analyser, or the ion cyclotron resonance or orbitrap instruments. Analysers can also be grouped based on other features, as for example ion-beam versus ion-trapping types, continuous versus pulsed analysis, low versus high kinetic energies.

The quadrupole mass analyser is one of the most commonly used type of analysers which employs stability trajectories of ions in oscillating electric fields to separate ions according to their m/z ratios. A simplified schematic view of a quadrupole mass analyser, in combination with an illustrative ionisation source and detector, is shown in Figure 3.5(a). It consists of four perfectly parallel rods of circular or hyperbolic cross-section. Ions entering the middle space between the rods are affected by the influence of a total electric field made up of quadrupolar alternating radio frequency (RF) field superimposed on constant direct current (DC) field resulting from the application of the potentials upon the rods shown

in Figure 3.5(b) with the signs "+" and "-" :

$$\Phi_0 = +(U \ - \ V cos(\omega t)) \quad \text{and} \quad -\Phi_0 = -(U \ - \ V cos(\omega t))$$

In these equations, Φ_0 is the potential applied to the rods, ω is the angular frequency (in radians per second = $2\pi\nu$, where ν is the frequency of the RF field), U is the direct potential and V is the "zero-to-peak" amplitude of the RF voltage. The applied potentials on the opposed pairs of rods varies sinusoidally at $cos(\omega t)$ cycles with time t. This effects in ions being able to cross the field-free region along the central axis of the rods but with oscillations amongst the poles themselves. Specific alternating combinations of the potentials U and V and frequency ω of the RF field result in ions of a particular m/z having a stable trajectory pass through the quadrupole to the detector and thus build up a mass spectrum. All other m/z values that have unstable trajectories discharge themselves upon hitting the quadrupole rods and not be detected. Typically U varies from 500 to 2000 V, and V from 0 to 3000 V (from -3000 to +3000 V peak to peak). The trajectory of the ions passing through a quadrupole is more complex than that shown in Figure 3.5(a). The mass range and resolution of an instrument is determined by the length and diameter of the rods. The inlet and exit slits depicted can either be slits or focusing electromagnetic lenses.

The final part of an MS instrument is detector that is able to generate from the incident ions an electric current that is proportional to their abundance. Detection of ions is always based on their charge, or mass, or velocity. Some detectors (like Faraday cup) are based on the measurement of direct charge current that is produced when an ion hits a surface and is neutralised. Other types (electron multipliers or electro-optical ion detectors) are based on the kinetic energy transfer of incident ions by collision with a surface that in turn generates secondary electrons, which are subsequently amplified to yield an electronic current.

Ion detectors can be divided into two classes. Some detectors are designed to count ions of a single mass at a time and therefore detect the incidence of all ions sequentially at one point (point ion collectors). Other detectors, such as photographic plates image current detectors or array detectors, can count multiple masses and detect incidence of all ions simultaneously along a plane

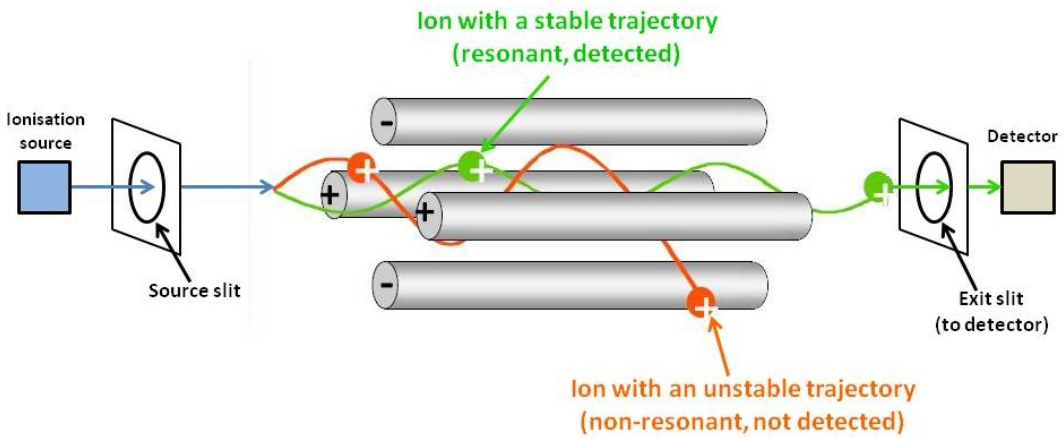

(a)

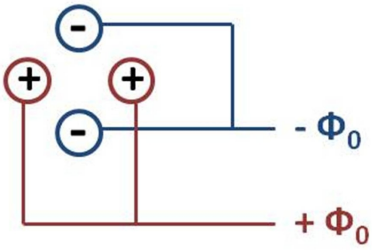

(b)

Figure 3.5: Schematic of (a) Quadrupole mass analyser in combination with ion source, focusing slits (lenses) and detector; (b) Quadrupole rods of circular cross-section with applied potentials.

(array collectors). Generally efficiency of an ion detector decreases when the mass of an ion increases. To allow an ion reach the detector without collision with other gaseous molecules, MS should function under high vacuum. Ion-molecule collision could result in unwanted reactions and hence increase spectrum complexity.

Electron multiplier (EM) is one of the most widely used type of modern detectors. In this type of detector, ions from the mass analyser are accelerated to a high velocity in order to increase detection efficiency. This is achieved by applying a high potential ranging from ± 3 to ± 30 kV to an electrode called the conversion dynode, the applied charge being opposite to the charge of the detected ions. A positive or negative ion hitting the conversion dynode causes emission of several secondary particles. These secondary particles can be positive

or negative ions, electrons or neutrals. When a positive ion hits the negative high-voltage conversion dynode, the secondary particles of interest are negative ions and electrons. With a negative ion it is the opposite. The secondary particles are converted to electrons at the first dynode. Electrons, in turn, are amplified by a cascade effect in the EM to generate a current. The EM may be of either discrete dynode or continuous dynode type (channeltron, microchannel plate or microsphere plate).

A schematic example of a continuous-dynode electron multiplier (CDEM, or channeltron) is sketched in Figure 3.6. It is a curve-shaped narrowing-diameter tube with inner thin surface of a semi-conducting material having good secondary emission properties. Since the walls of the tube have a uniform electric resistance, a voltage applied between two extremities of the tube produces a continuous accelerating field along its length. Usually the negative high voltage is applied at the wider input end, and positive voltage near ground is applied at the narrower output end of the tube. The field accelerates secondary electrons emitted upon collision of the secondary particles with the tube surface. The accelerated cascade of secondary electrons is collected by a metal anode at the detector exit and the measured current is processed into signal-spectrum.

The amplifying power is the product of the conversion factor (number of secondary particles emitted by the conversion dynode for one incoming ion) and the multiplying factor of the CDEM. Advantages of channeltrons are high amplification and fast response time, allowing fast scanning rate of the analyser. However, the conversion factor is strongly dependent on the impact velocity of the detected ions and on their nature (mass, charge and structure), therefore channeltrons are not as precise as Faraday cups. For example, large ions have low velocity, therefore produce fewer secondary electrons - efficiency decreases with increasing mass of the ion. Nevertheless, modern high-voltage conversion dynodes mitigate this disadvantage by accelerating high-mass ions or the ones delivered at low kinetic energy, such as from quadrupoles or ion traps.

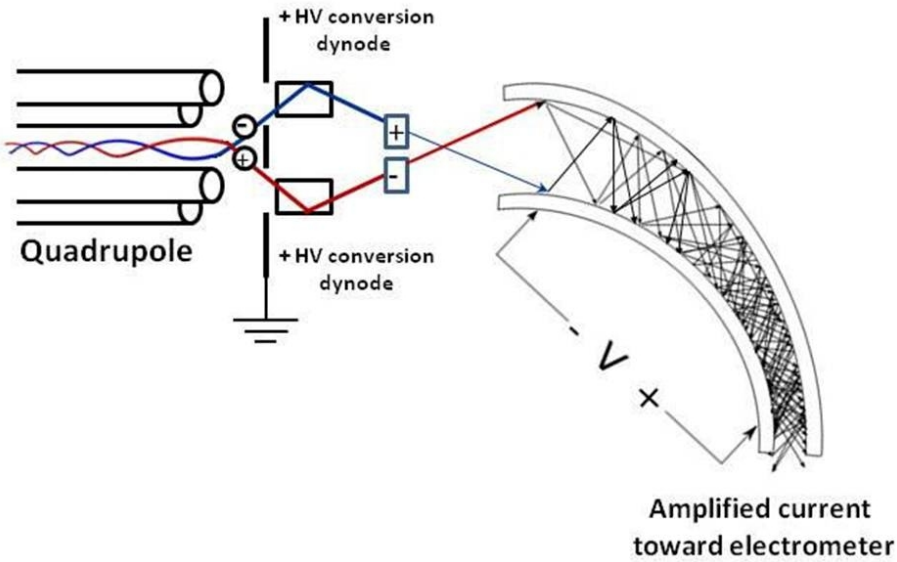

Figure 3.6: Continuous dynode electron multiplier, also known as channeltron. Circles - incident ions, squares - secondary particles. Figure adapted from [14] and modified.

3.3 Gas Chromatography

Gas chromatography is an analytical method based on differences in the partition coefficients of substances distributed between a static phase, usually of great surface area, and a moving fluid phase. It is widely used for testing the purity of a substance, separating, analysing and quantifying different components of a mixture.

If two immiscible phases A and B are in contact and some substance, miscible with both, is added it will be distributed between the two phases, equilibrium being attained when its free energy is the same in each. For these two phases, the partition coefficient, or distribution ratio, is given by Eq. 3.3:

$$K = \frac{C_A}{C_B} = \Delta\mu^0 \tag{3.3}$$

where C_A and C_B are the concentrations, and $\Delta\mu^0$ difference of standard chemical potentials of phases A and B. The partition coefficient is constant at constant temperature, since $\Delta\mu^0$ has a fixed value.

There are three main chromatography techniques listed, all of them based on

differences in the partition coefficients of mixed species [16]. First, in the elution technique (also called elution development), a discrete sample of a mixture is introduced into a stationary column, after which it is flushed through by an inert, flowing phase. Partition of the mixed species between the flowing and fixed phase occurs several times during residence time in the column, and, as a result, separation of components takes place.

In the second technique known as the displacement development a discrete sample of a mixture is introduced into a column, but the flowing phase contains, or may fully consist of, some gas, vapour or liquid which is much more strongly adsorbed by the fixed phase than any component of the mixture. As a result, there is competition for the fixed phase between the flowing phase and the components of the mixture, leading to the components being progressively displaced along the column at different rates.

In the third technique, called frontal development, a continuous stream of the mixture, which may or may not be diluted at constant initial concentration in an inert carrier fluid, is being analysed. The mixture components are sorbed by the fixed phase until the adsorption equilibrium for each component is established and the moving front of the mobile phase is depleted of the mixture components in direct proportion to their partition coefficients. The overall result is a separation in the moving front and appearance of the components at the column outlet at different times. Figure 3.7 schematises all the three techniques on the example of two components A and B.

Out of these three techniques, the elution technique is usually the most widely used one due to the fact that the other two techniques depend upon sorptive competition which introduces uncertainty and in practice may act detrimental to effectiveness of separation. In the leftmost part of Figure 3.7 the zones occupied by the components A and B in F originally may overlap, but they travel down the column at different speeds in accordance with the strength of adsorption. If the difference in adsorption strength is sufficient, the process ultimately results in separation of A and B in the form of "bands" of substance in eluent solution. By admitting a further amount of eluent, the bands successively emerge from the column.

The effluent of the column reaches a detector. One of the widely used types

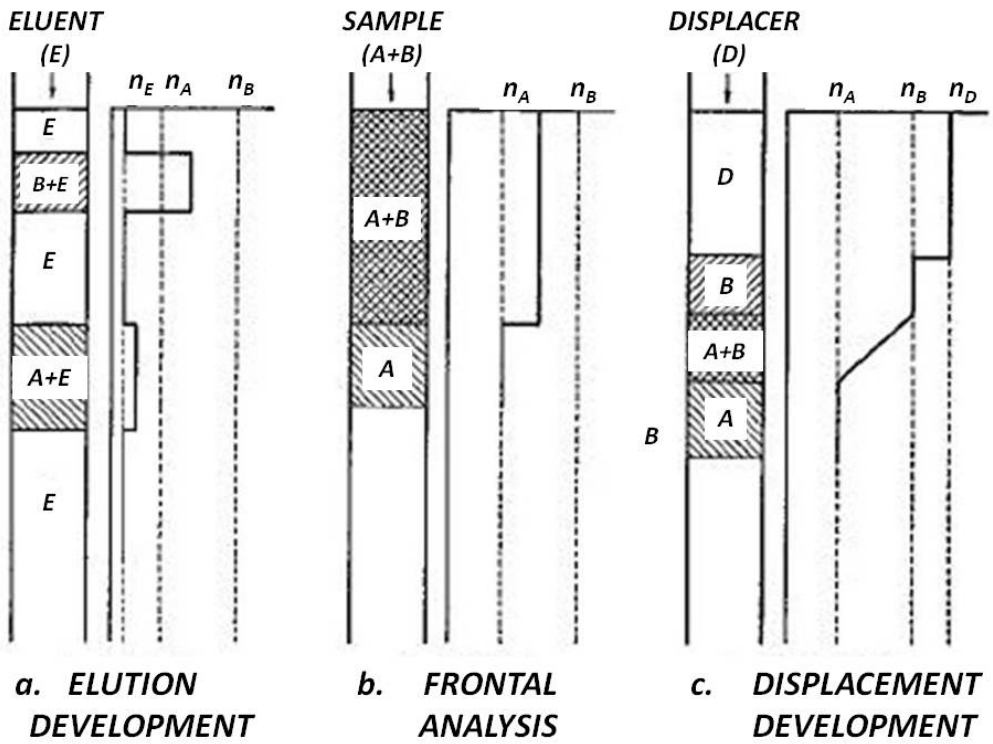

Figure 3.7: Schematic of the three chromatographic techniques on the example of samples A and B, eluent E and displacer D. Figure adapted from Keulemans [15]

of detectors are Thermal Conductivity Detectors (TCD), or, Katharometers. Katharometers contain a wire(s) of some metal having a high temperature coefficient of resistance, mounted axially in a temperature-controlled gas space. The wire (filament) is heated by a constant electric current. The conductivity of the surrounding gas is a factor determining filament temperature and consequently its resistance; the latter property is measured, which can be expressed in the mathematical form as Eq. 3.4:

$$\frac{I^2 R}{J} = \frac{2\pi \Delta\lambda L (T_f - T_c)}{\ln r_c / r_f} + S' \tag{3.4}$$

where I is the filament current, R is the filament resistance at the given temperature, J is the mechanical equivalent of heat, also known as Joule's constant ($4.1550\ \mathrm{J} \cdot \mathrm{cal}^{-1}$), T_f and r_f are the temperature and radius of the filament of

length L, whereas T_c and r_c are the corresponding quantities for the cylinder into which filament is placed. The term S' is the sum of heat losses by conduction through the electrodes, radiation, free convection, and forced convection when gas is flowing. The term S' should be as minimal as possible for accurate measurements. The term $\Delta\lambda$ is the difference between the thermal conductivities of the carrier (usually He or H_2) and analyte gases.

If the filament forms part of the Wheatstone bridge, shown in Figure 3.8, changes of thermal conductivity are converted into proportional electric signals with linear correlation. In the bridge the detector senses changes in the thermal conductivity of the column effluent and compares it to a reference flow of carrier gas, i.e., the term $\Delta\lambda$ in the form of potential difference. Apart from the detector and reference, two external resistors of quite large ohmage (100 Ω or even more) in parallel connection are used to compensate for drift due to flow or temperature fluctuations.

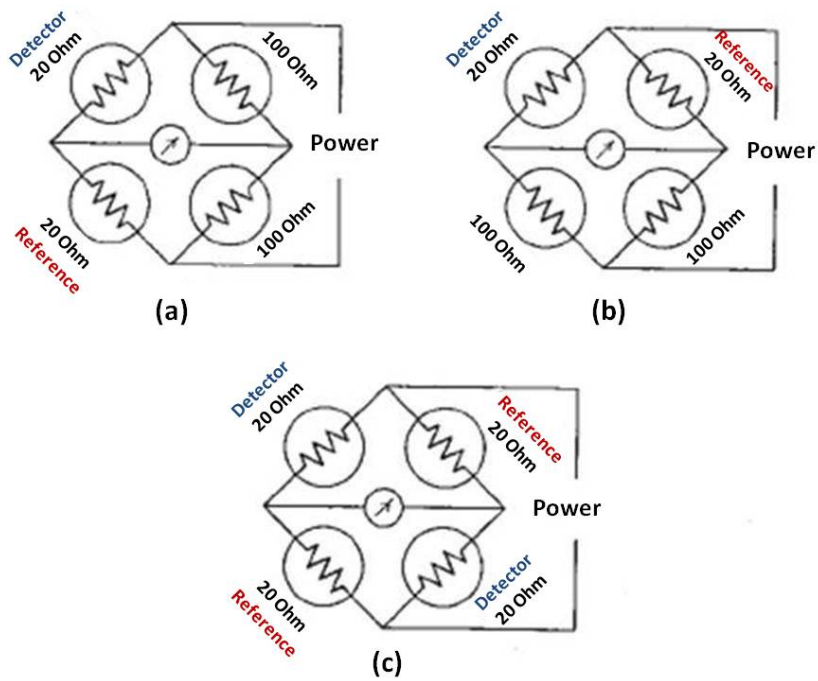

Figure 3.8: Conventional Wheatstone bridge circuits for multi-channel katharometers. Figure from Purnell [16] with slight graphical changes.

The sequence of equilibration in the elution technique leads to binominal, Pois-

son or Gaussian distributions of the analytes. In consequence of this, the characteristic chromatogram obtained from the elution column has the form shown in Figure 3.9.

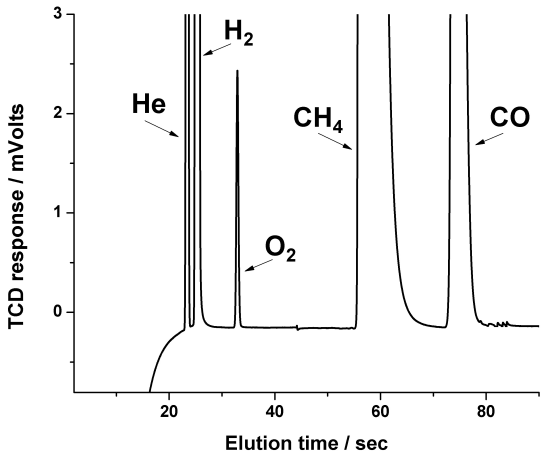

Figure 3.9: A typical elution chromatogram: CH_4, O_2, H_2 and CO are eluted by He at 100 °C from a 10-m Molsieve 5A column. Detection by direct-flow katharometer. Figure from experimental raw data in this thesis.

3.4 Gas Phase Methane Oxidative Coupling Measurements

Prior to all gas-phase experiments, the reactor tube, sampling capillary and $\alpha-Al_2O_3$ foams were pre-treated to remove any metal traces and organic contaminations. Pre-treatment included washing the parts with acetone, then dipping in 0.5M solution of HNO_3 overnight, rinsing in demineralised water (18 mΩ, Millipore) until the pH of wash-water was neutral, and finally drying: $\alpha - Al_2O_3$ foams at 200 °C for 6 hours, all other parts in vented oven at 60 °C overnight.

Figure 3.10 shows the schematic and real picture of the spatial profile reactor tube adjusted to the gas-phase OCM experiments with dimensions and the approximate height of the oven coils. The reactor dimensions were chosen in such a way that the surface-to-volume ratio of the reactor tube was low in order to have

minimal influence of the reactor walls on OCM chemistry. The heights of the front and back heat shields were 20 and 10 mm, respectively, and the gas space (titled Free Gas Phase) between the shields was on average 80 mm (it varied from experiment to experiment). Taking into account the heights of the heat shields, the total sampling length summed to ca. 110 mm.

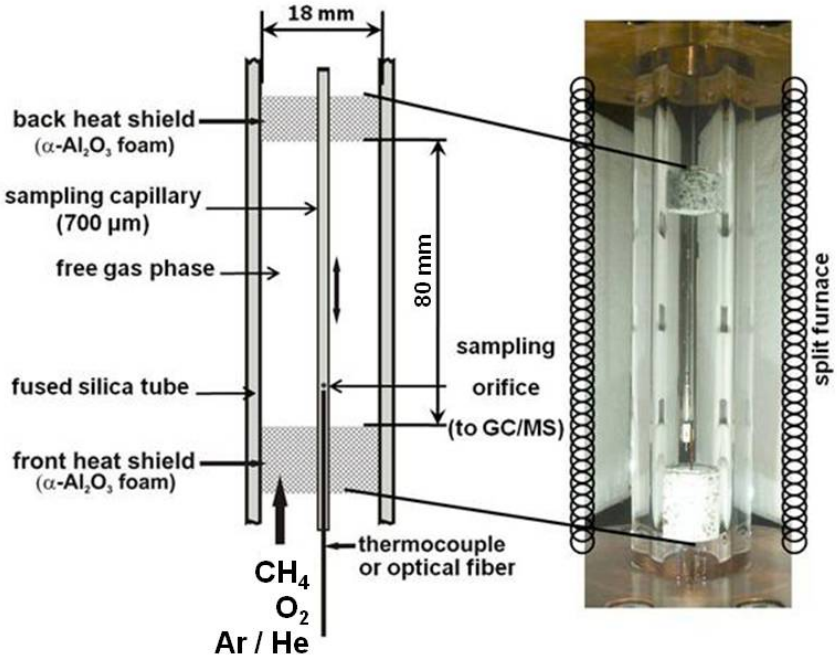

Figure 3.10: Schematic of spatial profile reactor for gas phase experiments.

Species sampling was done via a sampling orifice in the quartz sampling capillary that was either 25 μm in case of experiments with mass-spectrometric analysis, or 100 μm in case of gas-chromatographic analysis.

For gas-phase OCM experimental procedure the following parameters were varied: carbon-to-oxygen equivalence ratio (C/O ratio), inlet volumetric flow rate, pressure and temperature.

Carbon-to-oxygen equivalence ratio (C/O ratio) was defined as in Eq. 3.5:

$$\frac{C}{O} = \frac{\dot{V}_{CH_{4,0}}}{2\dot{V}_{O_{2,0}}} \tag{3.5}$$

where $\dot{V}_{CH_{4,0}}$ and $\dot{V}_{O_{2,0}}$ are the initial volumetric flow rates of methane and oxygen, $\text{mln} \cdot \text{min}^{-1}$. C/O ratios of 2, 4, 6, and 8 were investigated.

The combined volumetric flow rates of methane, oxygen and argon (or 8 vol.% He in Ar mixture) were set as 500, 1000, 2000 and 4000 $\text{mln} \cdot \text{min}^{-1}$. Argon or 8 vol.% He in Ar mixture was 10 vol.% from all set total flows, i.e., 50, 100, 200 and 400 $\text{mln} \cdot \text{min}^{-1}$. The space time for these total volumetric flow rates was calculated according to Eq. 3.6:

$$\tau_0 = \frac{V_{GP}}{\dot{V}_{total}} \tag{3.6}$$

where V_{GP} is the gas phase volume in which experiments are conducted; $\dot{V}_{total}$ is the total volumetric flow rate. As the average length of the free gas phase region was 80 mm, the space time for the set 4 volumetric flow rates varied from 6.4 to 0.79 s for 500 and 4000 $\text{mln} \cdot \text{min}^{-1}$ flow rates, respectively. The Reynolds number for these experimental conditions were calculated with Eq. 3.7:

$$Re = \frac{\rho v d_H}{\mu} \tag{3.7}$$

in which v is the fluid average linear velocity, $\text{m} \cdot \text{s}^{-1}$, d_H - hydraulic diameter, m, and μ is the fluid average dynamic viscosity, $\text{Pa} \cdot \text{s}$, was from 37 to 590.5 (laminar regime) for the corresponding lowest (500 $\text{mln} \cdot \text{min}^{-1}$) and highest (4000 $\text{mln} \cdot \text{min}^{-1}$) flow rates. All the parameters for the Reynolds number were calculated using actual temperature and pressure of the gaseous mixture.

The residence time was calculated according to Plehiers and Froment [111], who showed that the residence time is a function of the axial temperature profile in a reactor:

$$\tau_{res} = \int_0^V \frac{p_{total}\ dV}{F_0 R T} \cong \frac{A_c\ p_{total}}{F_0 R} \int_0^l \frac{dz}{T} \tag{3.8}$$

where V - volume of the reactor, m^3; p_{total} - total pressure, Pa; F_0 - total inlet

molar flow rate, $\mathrm{mol \cdot s^{-1}}$; R - universal gas constant, $\mathrm{J \cdot mol^{-1} \cdot K^{-1}}$; T - axial temperature profile, K; A_c - reactor cross-sectional surface area, $\mathrm{m^2}$; z - the reactor axial coordinate, m; l - total length of the reactor.

The scanning speed of the sampling capillary was varied from 14 to 88 $\mu\mathrm{m \cdot s^{-1}}$. For most experiments the scanning rate was set 17.5 $\mu\mathrm{m \cdot s^{-1}}$.

The pressure range set was from 1 to 20 bar. Oven temperature was set either by allowing the oven vary in heating power so that the temperature of the K-type thermocouple placed at the sampling orifice (thermocouple within capillary) was constant and maintained at 500 or 600 °C at the point of 2 mm above the front heat shield, or so that the K-type thermocouple of the oven (fixed between the reactor tube and oven heating shell) was constant and maintained at 750 °C.

Species were analysed either by the mass spectrometer only, using Ar as the internal standard, or with the mass spectrometer together with the micro gas chromatograph using 8 vol.% He in 92% Ar mixture (Ar for mass spectrometer, He for micro gas chromatograph). The internal standards were involved to calculate output molar flow rates of species. Analyte species of interest were CH_4, O_2, CO_x, H_2, C_2H_6, C_2H_4. Presence of $C_3 - C_4$ hydrocarbons was analysed too, but these hydrocarbons were detected in negligible concentrations and therefore omitted from discussion. Direct measurement of water concentration was not possible with both instruments, therefore water concentration was calculated from the oxygen species balance: lost oxygen atoms in oxygen balance were considered to be in water.

The molar flow rate of each species was calculated according to Eq. 3.9:

$$F_i = \frac{A_i}{A_{cal}} \frac{F_{cal}}{r_i} \tag{3.9}$$

where F_i and F_{cal} are the respective molar flow rates of species i and of internal standard (Ar or He), $\mathrm{mol \cdot min^{-1}}$: Ar for MS, He for micro GC; similarly, A_i and A_{cal} stand for peak area of the species i and of internal standard, mVolts; r_i is the response factor from instrument calibration, which was calculated according to Eq. 3.10:

$$r_i = \frac{A_i}{A_{st}} \frac{F_{st}}{F_i} \tag{3.10}$$

As can be seen, the calibration response factor r_i is equal to the slope of a least-squares linear fit of peak areas ratio versus molar flow rates ratio. Calibration curves for species of interest are given in Appendix A. Calculation of the molar flow rates was done using the volumetric flow rates according to the ideal gas law, Eq. 3.11:

$$P\dot{V}_i = F_i RT \tag{3.11}$$

where $\dot{V}_i$ and F_i are the volumetric ($\text{mln} \cdot \text{min}^{-1}$) and molar flow rates of species i; R - universal gas constant, 8.314 $\text{J} \cdot \text{mol}^{-1} \cdot \text{K}^{-1}$; T - temperature of MFCs calibration, 293.15 K. The gas was assumed to be ideal according to Hayes and Kolaczkowski [112], in which for simple gases and mixtures, such as air, assumption is accurate to within 1% for temperatures from 300 to 1800 K and pressures from 1 to 20 bar (100 to 2000 kPa).

Conversion of the reactants was calculated as in Eq. 3.13:

$$X_i = \frac{F_{i,0} - F_{i,z}}{F_{i,0}} \cdot 100\% \tag{3.12}$$

where $F_{i,0}$ and $F_{i,z}$ are the molar flow rates of CH_4 or O_2 at the inlet and at any axial position z, respectively.

Selectivity of carbon-containing products was calculated either on the basis of total methane conversion, Eq. 3.13:

$$S_i = \frac{n_i(F_{i,z} - F_{i,0})}{F_{CH_4,0} - F_{CH_4,z}} \cdot 100\% \tag{3.13}$$

in which n_i is the number of carbon atoms in the product species i, or on the basis of the sum of all carbon-containing products, Eq. 3.14:

$$S_i = \frac{n_i F_{i,z}}{\sum_i^K n_i F_{C,i,z}} \cdot 100\% \tag{3.14}$$

where $F_{C,i,z}$ is the molar flow rate of the ith carbon-containing product at any position z.

Yield of the ith component is calculated with selectivity on methane conversion

basis, and is given in Eq. 3.15:

$$Y_i = X_i \cdot S_i = \frac{n_i(F_{i,z} - F_{i,0})}{F_{CH_4,0}} \cdot 100\% \tag{3.15}$$

Mass balances of carbon (Eq. 3.16), hydrogen (Eq. 3.17) and oxygen (Eq. 3.18) were accepted if they closed to within ± 5%; n_i in these equations represents the number of carbon/hydrogen/oxygen atoms in the products.

$$MB_C = \frac{F_{CH_4,in} - \sum n_{C,out} F_{C,out}}{F_{CH_4,in}} \cdot 100\% \tag{3.16}$$

$$MB_H = \frac{4F_{CH_4,in} - \sum n_{H,out} F_{H,out}}{4F_{CH_4,in}} \cdot 100\% \tag{3.17}$$

$$MB_O = \frac{2F_{O_2,in} - \sum n_{O,out} F_{O,out}}{2F_{O_2,in}} \cdot 100\% \tag{3.18}$$

Species and temperature profiles usually consisted of many experimental points for plots (thousands in case of mass-spectrometric analysis). For fast analysis of profile raw data, a MATLAB script was written by O. Korup [113] and successfully applied in this thesis. The script is presented in Appendix B.

Chapter 4

Microkinetic Modeling and Modeling Procedure

4.1 Microkinetic Modeling of a Chemical Reaction

4.1.1 Introduction

A microkinetic model is a sequence of elementary steps (reactions) that attempts to describe at a molecular level the manner in which the catalytic reaction takes place [114]. Thus, a microkinetic model for a reaction is usually based on the kinetics of a network of elementary reactions. Prediction of product concentration profiles from a detailed microkinetic model includes numerical solution for a set of coupled partial differential rate equations for the contributing species, together with conservation equations for the appropriate reaction system: flow or static reactor, shock tube, etc.

Normally a network of elementary reactions in a microkinetic model may consist of tens to thousands of elementary reactions, i.e., tens to thousands of differential equations to solve, which is normally done using computer calculations. Computer calculations are based usually on software packages designed for that purpose, for example one of such packages is the Fortran code CHEMKIN from Sandia National Laboratories [115], which translates chemical nomenclature into

a code for processing with a stiff differential equation solution code LSODE [116] for a case-specific situation. For fast solution of large sets of ordinary differential equations usually the Gear algorithm is used [117]. Among other packages to be mentioned is CRESLAF that was used in this thesis [118].

Each ordinary differential equation to be solved out of a microkinetic mechanism is represented by the rate of progress for each reaction as in Eq. 4.1:

$$R_j = k_{fj} \prod_{i=1}^{K} [C_i]^{\nu'_{ij}} \; - \; k_{rj} \prod_{i=1}^{K} [C_i]^{\nu''_{ij}} \tag{4.1}$$

where $[C_i]$ is the molar concentration of the ith species, k_{fj} and k_{rj} are the forward and the reverse rate constants of the jth reaction, and ν_{ij} is the stoichiometric coefficient of the ith species in the jth reaction. The single and double prime indicate forward and reverse reactions, respectively. The forward and reverse rate constants for each elementary reaction are described by an extended Arrhenius equation.

The rate of production of each species in the overall model is the sum of the rate of progress for all reactions (reversible and irreversible) which contain the target species of interest. For example, for N reversible reactions containing K chemical species the rate of production $\dot{\omega}_i$ of the ith chemical species will be Eq. 4.2 [119]:

$$\dot{\omega}_i = \sum_{j=1}^{N} \nu_{ij} R_j \qquad (j = 1, 2, ..., N) \tag{4.2}$$

where ν_{ij} is the stoichiometric coefficient of the ith species in the jth chemical reaction; R_j is the rate of progress for the jth reaction.

4.1.2 Temperature Dependence of the Rate Constant

The extended Arrhenius expression representing dependence of the rate constant on temperature has the form given in Eq. 4.3:

$$k = A \; T^b \; exp\left(\frac{-E_{act}}{RT}\right) \tag{4.3}$$

in which A - pre-exponential (frequency) factor; T - absolute temperature, K; b – nonlinearity coefficient, also called temperature exponent, (-); E_{act} – apparent activation energy, $\mathrm{J \cdot mol^{-1}}$; R - universal gas constant, $\mathrm{J \cdot mol^{-1} \cdot K^{-1}}$; and the units for A are $\mathrm{s^{-1}}$ for a first-order reaction, $\mathrm{m^3 \cdot mol^{-1} \cdot s^{-1}}$ for a second-order reaction, and $\mathrm{m^6 \cdot mol^{-2} \cdot s^{-1}}$ for a third-order reaction.

The parameters of the rate constant should lie within boundaries of reasonable chemical and physical meaning, i.e., should be consistent with theoretical and empirical calculations. For example, collision theory and transition-state theory provide useful estimates of pre-exponential factors for elementary reactions. Activation energy, on the other hand, may rely more on experimental data than on theory, and is calculated from the slope of $\ln k$ versus $1/T$ [114].

4.1.3 Pressure Dependence of the Rate Constant

Apart from dependence of the reaction constant on temperature, expressed by the Arrhenius equation shown above, for some unimolecular reactions it has been observed that under certain conditions the reaction rate constant depends strongly on pressure. These reactions are referred to as dissociation/recombination fall-off reactions and chemically activated bimolecular reactions. In the first ones, the reaction rate increases with pressure, while for the second type it decreases when pressure increases. In the simplest form, pressure dependency of the unimolecular reaction rate constant is well described by the Lindemann theory [120]. An example herebelow to describe the Lindemann theory is taken from Warnatz et al. [11]. To decompose the molecule A to the product P, energy should be added to A by collision with a third-body (bath molecule) M (e.g., for excitation of the molecular vibrations). The excited molecule either decomposes into the product, or deactivates through a collision,

$$\mathrm{A + M \rightarrow A^* + M} \quad (\text{activation}, k_a) \tag{4.4}$$

$$\mathrm{A^* + M \rightarrow A + M} \quad (\text{deactivation}, k_{-a}) \tag{4.5}$$

$$\mathrm{A^* \rightarrow P} \quad (\text{unimolecular reaction}, k_u) \tag{4.6}$$

The rate equations in this case are given as:

$$\frac{d[\mathrm{P}]}{dt} = k_u[\mathrm{A}^*] \tag{4.7}$$

$$\frac{d[\mathrm{A}^*]}{dt} = k_a[\mathrm{A}][\mathrm{M}] - k_{-a}[\mathrm{A}^*][\mathrm{M}] - k_u[\mathrm{A}^*] \tag{4.8}$$

Assuming that the concentration of the reactive intermediate A^* is in a quasi-steady-state,

$$\frac{d[\mathrm{A}^*]}{dt} = 0, \tag{4.9}$$

one expresses the concentration of the activated species $[\mathrm{A}^*]$ and the formation of the product P as

$$[\mathrm{A}^*] = \frac{k_a[\mathrm{A}][\mathrm{M}]}{k_{-a}[\mathrm{M}] + k_u} \tag{4.10}$$

$$\frac{d[\mathrm{P}]}{dt} = \frac{k_u k_a[\mathrm{A}][\mathrm{M}]}{k_{-a}[\mathrm{M}] + k_u} \tag{4.11}$$

There are two limits for a reaction: low-pressure and high-pressure limits. In the low-pressure limit, the concentration of the collision partners M is very small; if $k_{-a}[\mathrm{M}] \ll k_u$, one obtains a second-order rate law:

$$\frac{d[\mathrm{P}]}{dt} = k_a[\mathrm{A}][\mathrm{M}] = k_0[\mathrm{A}][\mathrm{M}] \tag{4.12}$$

with the low-pressure rate constant usually denoted as k_0. Thus, the reaction rate is proportional to the concentration of species A and the collision partner M, because the activation is slow (rate-limiting) at low pressures.

In the high-pressure limit, the concentration of the collision partner M is large, and with $k_{-a}[M] \gg k_u$ one obtains the first-order rate law:

$$\frac{d[\mathrm{P}]}{dt} = \frac{k_u k_a[\mathrm{A}]}{k_{-a}} = k_\infty[\mathrm{A}] \tag{4.13}$$

with a high-pressure rate constant k_∞. At the high-pressure limit, the reaction rate does not depend on the concentration of collision partners M, because at high pressures collisions occur very often, therefore the decomposition of the activates

species A is rate-limiting instead of activation.

Between the high- and low-pressure regions, there is a "fall-off" region represented by a fall-off equation

$$p_r = \frac{k_0[\mathrm{M}]}{k_\infty} = \frac{[\mathrm{M}]}{[\mathrm{M}]_c} \tag{4.14}$$

where p_r is the reduced pressure (units not in bar), $[\mathrm{M}]_c$ is the centre of the fall-off curve and indicates the third-body concentration for which the extrapolated k_0 would be equal to k/k_∞. The rate constant at any pressure within the fall-off region is given as the equation:

$$k = \frac{k_0 k_\infty [\mathrm{M}]}{k_0[\mathrm{M}] + k_\infty} F \tag{4.15}$$

in which F is called the broadening factor. If this factor is unity, then this is the Lindemann form. In the Troe [121] form, the factor F is given by

$$\log(F) = \frac{\log(F_{cent})}{1 + [(\log(p_r) \ + \ c)/(n \ - \ d(\log(p_r) \ + \ c))]^2} \tag{4.16}$$

with coefficients

$\mathrm{c} = 0.4 - 0.67 \log \mathrm{F_{cent}}$

$\mathrm{n} = 0.75 - 1.27 \log \mathrm{F_{cent}}$

$\mathrm{d} = 0.14$

where F_{cent} is an approximation for the temperature dependence of the broadening factor, calculated as:

$$F_{cent} = (1 - a) \ exp\left(-\frac{T}{T^{***}}\right) + a \ exp\left(-\frac{T}{T^{*}}\right) + exp\left(-\frac{T^{**}}{T}\right) \tag{4.17}$$

The four adjustable parameters (a, T^{***}, T^{*}, and T^{**}) must be specified as auxiliary data in the input file of the microkinetic mechanism. In combination with the parameters of the modified Arrhenius equation (A, β, E_a) for both the low- and high-pressure rate constants, the overall fall-off representation requires 10 parameters. An example of the rate constant dependence on pressure, as well as temperature, in the pressure fall-off region is shown in Figure 4.1 The SRI formal-

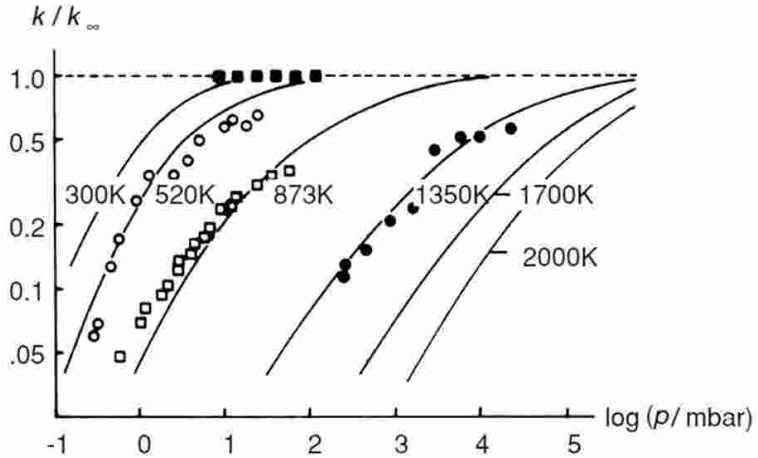

Figure 4.1: Rate constant as a function of pressure at various temperature for a unimolecular reaction $C_2H_6 \rightarrow CH_3 + CH_3$. Figure adapted from Warnatz et al. [11].

ism, introduced by Stewart et al. [122], has the broadening factor F approximated differently:

$$F = d\left[a\ exp\left(-\frac{b}{T}\right) + exp\left(-\frac{T}{c}\right)\right]^{x}\ T^{e} \tag{4.18}$$

where

$$x = \frac{1}{1 + (\log p_r)^2} \tag{4.19}$$

Thus, the SRI approximation contains the four adjustable parameters a, b, c, x. The implementation of the fifth parameter, d, is specific in case of using the method with the CHEMKIN software. In total 11 parameters are available to provide a good fit to the data.

In addition to these 3 formalisms mentioned above, several other parameterisations to represent pressure-dependent rate constants based on k_0 and k_∞ are known, such as those of Wang and Frenklach [123], Gardiner [124], Poole and Gilbert [125], etc. However, these methods are not widespread and are not implemented in the CHEMKIN software.

4.1.4 Thermodynamic Data

Each species in a reaction must be associated with thermodynamic properties which are tabulated as a function of temperature. These thermodynamic data are obtained from calorimetric measurements (only few of the values are obtained in this way), or by theory using the group additivity theory [126] or by spectroscopic data (most of the data are derived from the two latter sources). Thermodynamic tables such as those of Stull and Prophet (JANAF Tables) [127], Burcat [92], and Sandia CHEMKIN (Kee et al.) [20] are usually used.

The thermodynamic data are used to calculate equilibrium constants (Eq. 4.20) and reverse-rate coefficients for a reaction:

$$K_{Cj} = \frac{k_{fj}}{k_{rj}} = K_{pj} \left(\frac{P_{atm}}{RT} \right)^{\sum_{j=1}^{N} \nu_{ij}} \tag{4.20}$$

with the equilibrium constant in concentration units K_{Cj}, and where the equilibrium constant in pressure units K_{pj} is determined from Eq. 4.21:

$$K_{pj} = exp \left(\frac{\Delta S_j^0}{R} - \frac{\Delta H_j^0}{RT} \right) \tag{4.21}$$

The Δ refers to the change that occurs in passing completely from reactants to products in the jth reaction having S_j^0 and H_j^0 entropy and enthalpy at standard conditions (p = 1 bar and the considered temperature), respectively. Specifically, each term in Eq. 4.21 is equal to Eq. 4.22, 4.23:

$$\frac{\Delta S_j^0}{R} = \sum_{i=1}^{K} \nu_{ij} \frac{\Delta S_i^0}{R} \tag{4.22}$$

$$\frac{\Delta H_j^0}{R} = \sum_{i=1}^{K} \nu_{ij} \frac{\Delta H_i^0}{R} \tag{4.23}$$

Enthalpy, entropy and heat capacity of each species are calculated from NASA polynomials in the temperature range from 300 to 5000 K. The NASA polynomials have the form:

$$\frac{C_{p(i)}}{R} = a_1 + a_2 T + a_3 T^2 + a_4 T^3 + a_5 T^4, \tag{4.24}$$

$$\frac{H_i}{RT} = a_1 + a_2\frac{T}{2} + a_3\frac{T^2}{3} + a_4\frac{T^3}{4} + a_5\frac{T^4}{5} + \frac{a_6}{T}, \tag{4.25}$$

$$\frac{S_i}{T} = a_1 \ln T + a_2 T + a_3\frac{T^2}{2} + a_4\frac{T^3}{3} + a_5\frac{T^4}{4} + a_7, \tag{4.26}$$

where a_1, a_2,..., a_7 are the polynomial fitting coefficients for low (300 – 1000 K) and high (1000 – 5000 K) temperature range (total 14 coefficients) supplied in the thermodynamic files.

4.1.5 Transport Data

The transport data normally consists of 7 columns. They are in the following order (from left to right) [118]:

- Graphical representation of the species;
- An index indicating if the molecule has a monoatomic, linear or non-linear geometrical configuration. For single-atom molecule, the index is 0. For linear and non-linear molecules the indices are 1 and 2, respectively;
- The Lennard-Jones potential well depth ϵ/k_B in Kelvins;
- The Lennard-Jones collision diameter σ in angstroms;
- The dipole moment μ in Debye;
- The polarisability α in cubic angstroms;
- The rotational relaxation collision number Z_{rot} at 298.15 K temperature;
- A comment line that has either a period (.), slash (/), or exclamation mark (!) as the first blank character;

Some of the numbers in such a transport database have been determined by computing "best fits" to experimental measurements of a macroscopic transport property (e.g., viscosity). In other cases the Lennard-Jones parameters have been estimated following the methods outlined in Svehla [128]. In other cases they have been determined by computational chemistry techniques.

4.1.6 Analysis of Microkinetic Models

Detailed analysis of a microkinetic model can be carried out by the kinetic sensitivity, reaction flow, and eigenvector analyses which are usually a built-in options in simulation softwares. The sensitivity analysis determines influence of each elementary reaction on the product distribution. The principle of the method is that the pre-exponential factor (A_j) of each elementary reaction in turn is varied and the effect of this variation on the concentration of each product (C_i) is quantified by a set of first-order normalised sensitivity factors/coefficients (s_{ij}), which can be absolute sensitivity coefficients, calculated as in Eq. 4.27:

$$s_{ij} = \frac{\partial C_i}{\partial A_j}, \tag{4.27}$$

or relative sensitivity coefficents, calculated as in Eq. 4.28:

$$s_{ij} = \frac{A_j}{C_i}\frac{\partial C_i}{\partial A_j} \tag{4.28}$$

where s_{ij} stands for reaction-rate sensitivity coefficient of C_i to the step j. So, the sensitivity analysis of a microkinetic model provides important information about rate-determining reactions.

According to Warnatz et al. [3]..."Reaction flow analysis determines the characteristic reaction paths by considering the percentage of the contributions of different reactions j ($j = 1, ..., J$) to the formation (or consumption) of the chemical species i ($i = 1, ..., I$). Flow analysis can be integral – considers the overall formation or consumption during the combustion process, when the results for homogeneous time-dependent systems are integrated over the whole reaction time - as well as local - considers the species formation and consumption locally, i.e., at specific times in time-dependent problems (e.g., homogeneous ignition process) or at specific locations in steady processes (e.g., a flat flame). Eigenvector analysis determines the characteristic time scales and directions of the chemical reactions. Eigenvalues and eigenvectors of the Jacobian matrix, for example, reveal information about reactions time scale and about species in steady state or reactions in partial equilibrium"...

On account of sensitivity, flow and eigenvector analyses, only significant reac-

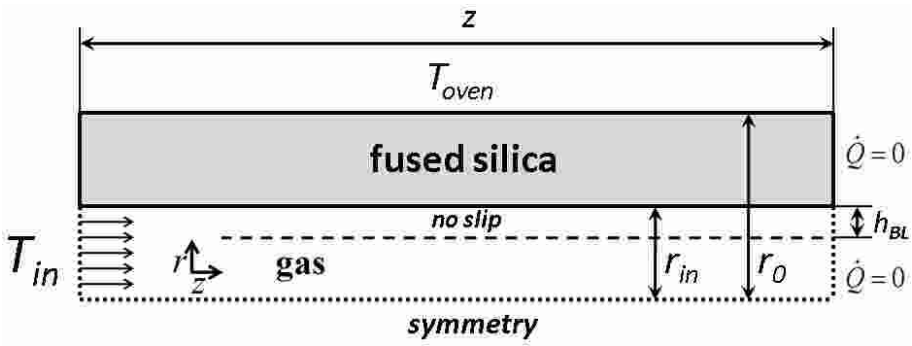

Figure 4.2: Computational domain for microkinetic modeling in the profile reactor. Reactor radius r_{in} = 9 mm, reactor radius with reactor wall r_0 = 9 mm, axial computational length z = 80.5 mm, h_{BL} – boundary layer thickness.

tions for product distributions can be selected, leading to shortening of a model. Usually acceptance of a model is done by comparison with the experimental data, by goodness of fit. Statistical analysis can further strengthen confidence in favour of a model.

4.2 Microkinetic Modeling of Gas-Phase Methane Oxidative Coupling Measurements

4.2.1 Setting Modeling Parameters

CHEMKIN Pro software, release 15101 [118] with CRESLAF code was used for modeling. The simulations used two-dimensional parabolic (boundary-layer) model applied through the cylindrical-shear-flow reactor model. The boundary condition was the measured maximal oven temperature set as the ambient temperature in the Chemkin window.

Fig. 4.2 shows the computational domain for simulation with the cylindrical-shear-flow reactor model. A number of uniform grid points of 50 in radial direction with stretch parameter of 1.0 were set, and mixture-averaged transport properties with no-slip velocity at the wall were chosen. Boundary layer thickness was chosen to be 100 μm (h_{BL} in the sketch), that is equal to the struts thickness of the α-Al_2O_3 foams [104]. Lump error was calculated to the main bath gas argon.

Justification for each chosen modeling parameter is given in the subsequent sub-sections. In general, advantages of the chosen code (CRESLAF) and the reactor model (boundary-layer) is non-limited number of chemical species for modeling, inclusion of heat and mass diffusion in radial direction, of heat loss and gain through the fused silica wall. Disadvantages are neglection of heat and mass diffusion in axial direction, of heat conduction in the fused silica wall.

4.2.2 Application of Flow Equations

Flow equations describe reacting flow situations in which a reactive stream flows interior of a channel or duct. In a traditional chemical engineering sense, tubular flow reactors are implied as channels. The most comprehensive description of a flow in a tubular reactor, taking into account both axial and radial mass, momentum, and energy balances, would be that based on solving the complete Navier-Stokes equations (Eq. 4.29-4.34, [129]), which are complicated to set for computer run, and which also require significant computation times to converge to solution.

The Navier-Stokes equations:

Mass continuity:

$$\frac{\partial \rho u}{\partial z} + \frac{1}{r}\frac{\partial r \rho \upsilon}{\partial r} = 0. \tag{4.29}$$

Axial momentum:

$$\begin{aligned} \rho u \frac{\partial u}{\partial z} + \rho \upsilon \frac{\partial u}{\partial r} = -\frac{\partial p}{\partial z} + \frac{\partial}{\partial z}\left[\frac{4}{3}\mu\frac{\partial u}{\partial z} - \frac{2}{3}\mu\frac{1}{r}\frac{\partial r\upsilon}{\partial r}\right] + \\ + \frac{1}{r}\frac{\partial}{\partial r}\left[\mu r\left(\frac{\partial \upsilon}{\partial z} + \frac{\partial u}{\partial r}\right)\right]. \end{aligned} \tag{4.30}$$

Radial momentum:

$$\begin{aligned} \rho u \frac{\partial \upsilon}{\partial z} + \rho \upsilon \frac{\partial \upsilon}{\partial r} = -\frac{\partial p}{\partial r} + \frac{\partial}{\partial z}\left[\mu\left(\frac{\partial \upsilon}{\partial z} + \frac{\partial u}{\partial r}\right)\right] + \\ + \frac{\partial}{\partial r}\left[\frac{4}{3}\mu\frac{\partial \upsilon}{\partial r} - \frac{2}{3}\mu\left(\frac{\partial u}{\partial z} + \frac{\upsilon}{r}\right)\right] + \frac{2\mu}{r}\left[\frac{\partial \upsilon}{\partial r} - \frac{\upsilon}{r}\right]. \end{aligned} \tag{4.31}$$

where the divergence of the velocity field in these equations,

$$\nabla \cdot \mathsf{V} = \frac{\partial u}{\partial z} + \frac{\partial \upsilon}{\partial r} + \frac{\upsilon}{r}. \tag{4.32}$$

has been explicitly incorporated.

Species continuity:

$$\begin{aligned} &\rho u \frac{\partial Y_i}{\partial z} + \rho \upsilon \frac{\partial Y_i}{\partial r} = \left(\frac{\partial \dot{J}_{i,z}}{\partial z} + \frac{1}{r} \frac{\partial (r \dot{J}_{i,r})}{\partial r} \right) + \dot{\omega}_i W_i, \\ &(i = 1, ..., \ K_g). \end{aligned} \tag{4.33}$$

Thermal energy:

$$\begin{aligned} &\rho c_p \left(u \frac{\partial T}{\partial z} + \upsilon \frac{\partial T}{\partial r} \right) = u \frac{\partial p}{\partial z} + \frac{\partial}{\partial z} \left(\lambda \frac{\partial T}{\partial z} \right) + \\ &+ \frac{1}{r} \frac{\partial}{\partial r} \left(r \lambda \frac{\partial T}{\partial r} \right) - \sum_{i=1}^{K} c_{p,i} \left(\dot{J}_{i,z} \frac{\partial T}{\partial z} + \dot{J}_{i,r} \frac{\partial T}{\partial r} \right) - \\ &- \sum_{i=1}^{K} h_i \dot{\omega}_i W_i. \end{aligned} \tag{4.34}$$

In these equations the independent variables are the axial (z) and radial (r) spatial coordinates. Axial velocity u, radial velocity υ, species mass fractions Y_i, temperature T and pressure p are dependent variables. Other variables are: mass density ρ, viscosity μ, thermal conductivity λ, species enthalpies h_i, and specific heat capacity c_p. W_i, $\dot{J}$, and $\dot{\omega}_i$ are species molecular weights, diffusive flux, and gas-phase species production by homogeneous chemical reaction, respectively.

The boundary-layer equations (Eq. 4.35-4.39), on the other hand, offer simplifications and, as a result, a shorter computation time. With boundary-layer approximations, the characteristics of the steady-state governing equations change from elliptic to parabolic, which is a significant simplification. In other words, the radial momentum equation is shifted to assumption that there can be no pressure variation across the channel radius. Furthermore, the axial diffusive transport is neglected in relation to axial convective transport, resulting in elim-

ination of all the second derivatives in axial coordinate z. After finite-difference or finite-volume discretization, the resulting problem may be solved numerically by the method of lines as a differential algebraic system. The boundary-layer equations conserve a full two-dimensional representation of all the field variables and non-linear behaviour of the Navier-Stokes equations [129].

The boundary-layer equations:

Mass continuity:

$$\frac{\partial \rho u}{\partial z} + \frac{1}{r}\frac{\partial r \rho \upsilon}{\partial r} = 0. \tag{4.35}$$

Axial momentum:

$$\rho u \frac{\partial u}{\partial z} + \rho \upsilon \frac{\partial u}{\partial r} = -\frac{\partial p}{\partial z} + \frac{1}{r}\frac{\partial}{\partial r}\left(\mu r \frac{\partial u}{\partial r}\right). \tag{4.36}$$

Radial momentum:

$$\frac{\partial p}{\partial r} = 0. \tag{4.37}$$

Species continuity:

$$\rho u \frac{\partial Y_i}{\partial z} + \rho \upsilon \frac{\partial Y_i}{\partial r} = -\frac{1}{r}\frac{\partial r \dot{J}_{i,r}}{\partial r} + \dot{\omega}_i W_i, \ (i = 1, ..., \ K_g). \tag{4.38}$$

Thermal energy:

$$\begin{aligned} \rho c_p \left(u \frac{\partial T}{\partial z} + \upsilon \frac{\partial T}{\partial r}\right) = u \frac{\partial p}{\partial z} + \frac{1}{r}\frac{\partial}{\partial r}\left(r \lambda \frac{\partial T}{\partial r}\right) - \\ - \sum_{i=1}^{K} c_{p,i} \dot{J}_{i,r} \frac{\partial T}{\partial r} - \sum_{i=1}^{K} h_i \dot{\omega}_i W_i. \end{aligned} \tag{4.39}$$

Even more simpler flow equations are those based on the plug-flow assumptions, when diffusion in the axial direction is assumed to be small compared to axial convective transport. In this regard, plug-flow equations are similar to boundary-layer equations. In the radial direction, however, diffusion is assumed to be infinitely fast, therefore there are no diffusive terms in the radial coordinate r. The plug-flow equations (Eq. 4.40-4.43) are given below.

The plug-flow equations:

Mass continuity:

$$\frac{d\rho u}{dz} = 0. \tag{4.40}$$

Axial momentum:

$$\rho u \frac{du}{dz} = -\frac{du}{dz} - \frac{P}{A_c}\tau_w. \tag{4.41}$$

with P and A_c being the perimeter and cross-sectional area of the tube, respectively, and τ_w is the wall shear stress, Pa.

Species continuity:

$$\rho u \frac{dY_i}{dz} = \dot{\omega}_i W_i, \ (i = 1, ..., \ K_g). \tag{4.42}$$

Thermal energy:

$$\rho u c_p \frac{dT}{dz} = \frac{\hat{h}P}{A_c}(T_w - T) - \sum_{i=1}^{K} h_i \dot{\omega}_i W_i. \tag{4.43}$$

where $\hat{h}$ is the heat transfer coefficient from the wall of temperature T_w to the fluid with temperature T inside the reactor. Plug-flow equations, however, are not applicable to our experimental flow conditions according to the Cleland and Wilhelm [19] criterion for laminar flow developed to justify assumption of plug flow limit in an empty tube, as shown in Eq. 4.44. This criterion was derived from the solution of a complete continuity equation which takes into account the flow by convection, axial and radial diffusion, and a first-order reaction, and is shown in Eq. 4.44:

$$\frac{D\tau_{res}}{r_t^2} > 1 \tag{4.44}$$

In this equation, τ_{res} is the residence time calculated according to Plehiers and Froment [111], s, r_t is the tube radius, m, and D is the mass diffusion coefficient for the assumed $CH_4 - O_2$ binary mixture, $m^2 \cdot s^{-1}$, calculated according to Bird

et al. [17] by Eq. 4.45:

$$D_{CH_4-O_2} = 0.0018583\sqrt{T^3\left(\frac{1}{M_{CH_4}}+\frac{1}{M_{O_2}}\right)}\frac{1}{p\sigma^2_{CH_4-O_2}\Omega_{D_{CH_4-O_2}}} \tag{4.45}$$

with p being total pressure in atm, and $\sigma_{CH_4-O_2}$ (Å) and $\Omega_{D_{CH_4-O_2}}$ (unitless) being the collision integral for diffusion and the Lennard-Jones parameter, respectively. For further comparison and verification, the diffusion coefficient was also calculated according to Fuller et al. [18]:

$$D_{CH_4-O_2} = \frac{1.013\times10^{-2}T^{1.75}\left(\frac{1}{M_{CH_4}}+\frac{1}{M_{O_2}}\right)^{\frac{1}{2}}}{p\left[\left(\sum v_i\right)^{1/3}_{CH_4}+\left(\sum v_i\right)^{1/3}_{O_2}\right]^2} \tag{4.46}$$

in which p is the total pressure in Pa, and v_i are the diffusional volumes calculated from diffusional volume increments of each atom in an ith molecule. Calculations of the mass diffusion coefficients and of Cleland and Wilhelm criterion are shown in Appendix D.

4.2.3 Boundary Conditions

The boundary conditions for simulation was the oven temperature set as ambient temperature in the CHEMKIN Pro input window. Separate experimentation to measure the oven temperature profiles at different oven heating power values was done by the following sequential steps[1]: 1) filling the reactor tube with a 150-mm-long stack of graphite cylinders, which served as black body; 2) setting the oven to certain heating power values, and then by waiting till thermal equilibration between the graphite and oven was reached for each oven power value; 3) measuring the temperature of the graphite cylinders by a two-wavelength pyrometer. The pyrometer fiber was translated vertically across a central axial bore hole in the cylinders. The experimental oven temperature profiles were then fitted by a third-order polynomial function to obtain a continuous temperature profile as a function of heating power and axial position, shown in Figure 4.3[2]:

[1] Oven temperature profiles were measured by Oliver Korup, FHI
[2] Fitting in MATLAB software was done by Dr. R. Horn, FHI

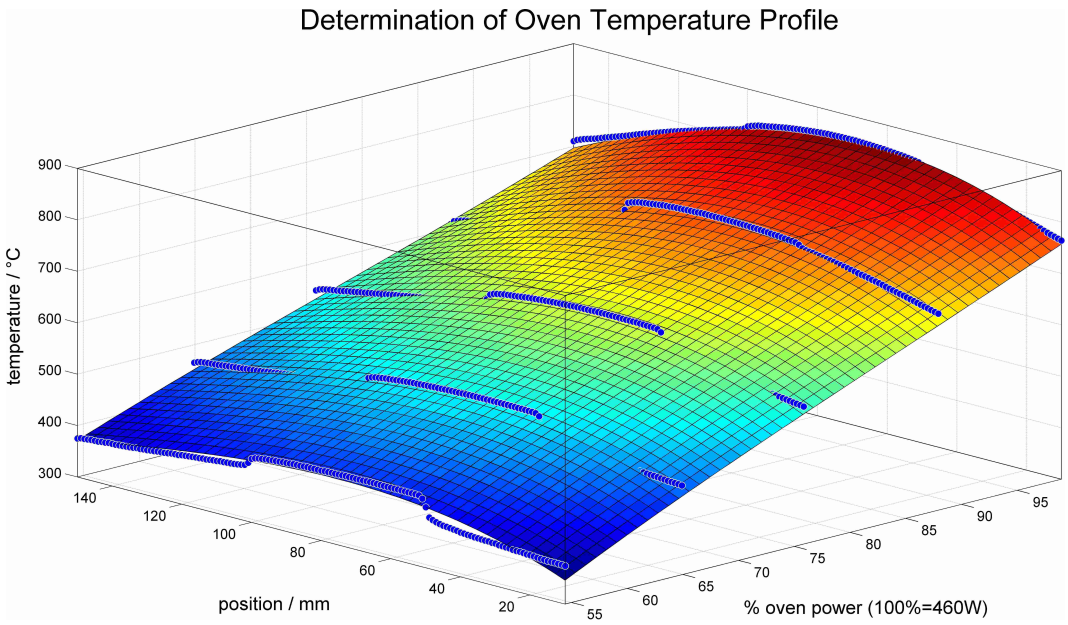

Figure 4.3: Five oven temperature profiles measured along the 150-mm stack of three graphite cylinders and fitted by a third-order polynomial in MATLAB to obtain a continuous profile of temperature as a function of oven heating power and stack position. Temperature profiles were measured and adapted from O. Korup, FHI. MATLAB fitting script is given in Appendix C.

The resulting oven temperature as a function of oven heating power P and axial position z is shown in Eq. 4.47:

$$\frac{T_{oven}(P,z)}{°\mathrm{C}} = -558.9 + 23.63\ P + 2.604\ z - 0.1761\ P^2 + 0.777 \times 10^{-2}\ P\ z - \\ - 1.652 \times 10^{-2}\ z^2 + 6.831 \times 10^{-4}\ P^3 + 1.067 \times 10^{-4}\ P^2\ z - \\ - 2.361 \times 10^{-4}\ P\ z^2 + 6.378 \times 10^{-5}\ P^3 \tag{4.47}$$

The maximal temperature from the oven temperature profile was chosen as the boundary condition. The boundary condition was of Dirichlet type. The heat transfer coefficient required to be set along with the ambient temperature was calculated for fused silica, the reactor wall material. For heat transfer calculation, the polynomial dependence of fused silica thermal conductivity on temperature derived by Bityukov and Petrov [130] for the temperature range of 600-1500 K

was used (Eq. 4.48):

$$\begin{aligned}\lambda = 0.27698 \ + \ 0.00574\, T \ - \ 9.33005 \times 10^{-6}\, T^2 + \\ + 7.26615 \times 10^{-9}\, T^3 \ - \ 1.84084 \times 10^{-12}\, T^4\end{aligned} \tag{4.48}$$

where λ is expressed in $\mathrm{W \cdot m^{-1} \cdot K^{-1}}$, and T in K. The authors obtained $\lambda(T)$ by the least square fit of thermal conductivity data for fused silica from various literature sources. Besides, calculation of the heat transfer coefficient took into account tube curvature [131] and was of the form shown in Eq. 4.49:

$$h = \frac{\lambda}{r_i \ln\left(r_0/r_i\right)} \tag{4.49}$$

with r_0 and r_i as the outer and inner tube radii, respectively. The final estimation of the calculated heat-transfer coefficient was done by comparison of the experimental and simulated temperature profiles of pure methane and argon, i.e., in the absence of chemical reaction, at atmospheric pressure and oven temperature of about 300 and 880 °C in case of Ar, for instance. A good agreement (Figure 4.4) proves correct estimation of the heat-transfer coefficient, although agreement decreases as the volumetric flow rate increases.

4.2.4 Microkinetic Models

For modeling the experimental data the microkinetic models outlined in Table 2.2 were used. Some of the mechanisms from these models contain pressure-dependent elementary reactions, and a user of the mechanism is required to select the correct rate constant parameters for the considered pressure. In this thesis, such a selection was automatised for the use with the CHEMKIN software by introducing the PLOG formalism which plots the logarithm of the rate constant parameters versus the logarithm of the available pressures. Such a plot in essence interpolates the rate constant parameters to any pressure in case the mechanism does not offer the choice of the exact pressure. The notation for PLOG formalism was followed from CHEMKIN software Manuals.

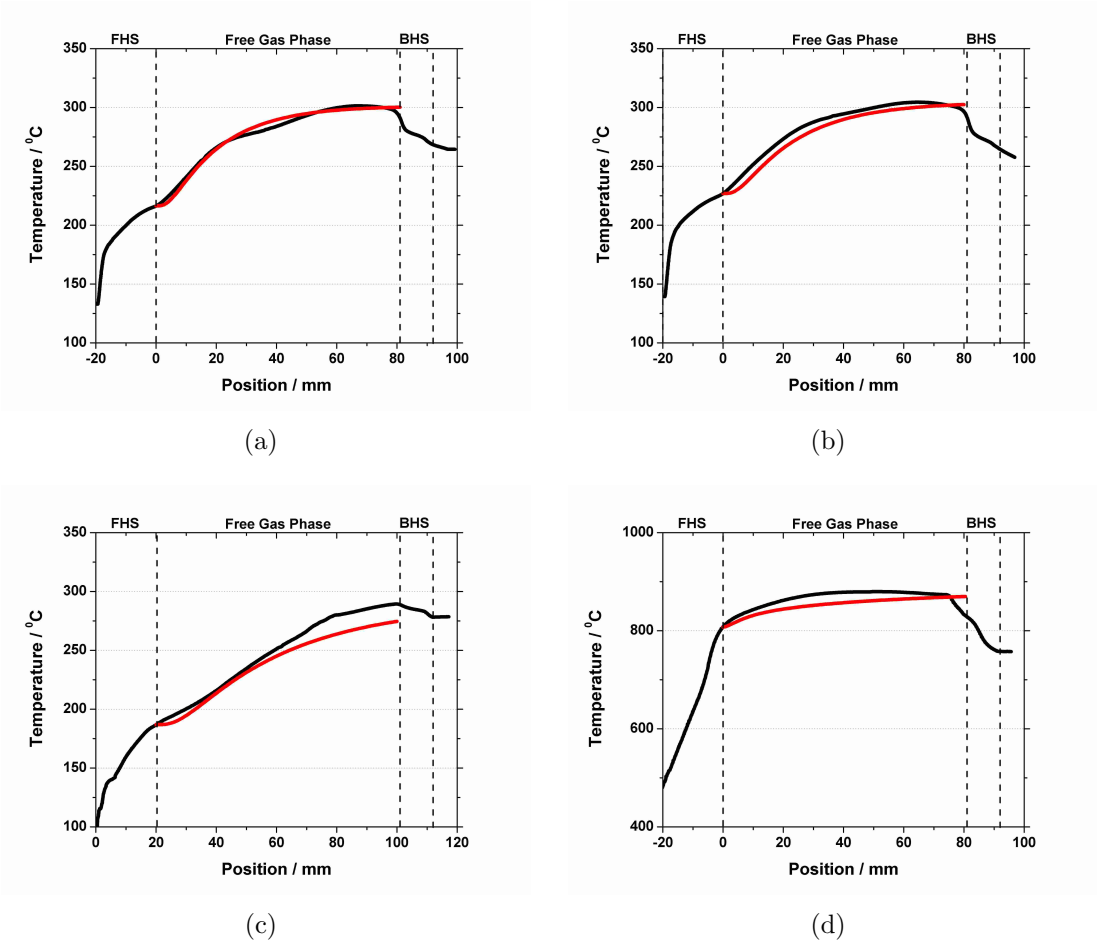

Figure 4.4: Temperature profiles at 1 bar pressure in the reactor with a) 500 mln · min^{-1} CH_4 at 40% oven power; (b) 500 mln · min^{-1} Ar at 40% oven power; (c) 1000 mln · min^{-1} CH_4 at 40% oven power; (d) 2000 mln · min^{-1} Ar at 100% oven power. Black lines - experimental temperature; red lines - simulated temperature in the free gas phase region.

4.2.5 Caveats and Assumptions for Microkinetic Modeling

In the process of microkinetic reactor modeling, certain aspects of experimental data and mathematical modeling remained unresolved and therefore assumed, which should be taken into account and mentioned. The description of each point is given below.

1) Gas-Phase Temperature Profile Measurement

Since the reactor tube was the transparent fused silica, the gas-phase temperature measured by the in-capillary thermocouple might be not precisely the real temperature of the gas, but a combination of the real temperature of the gas and infra-red radiation from the hot oven coils. Such a case might yield a gas temperature which is higher that the actual temperature. Besides, infra-red light absorption by gaseous molecules (mainly by methane) was not taken into account.

2) Oven Temperature Profile Measurement

During the measurement of oven temperature profiles through graphite cylinders, it was assumed that graphite is equilibrated with oven heat transferred from coils to the reactor tube in horizontal direction. In reality heat can also be transferred in vertical direction and dissipated, thus having not been measured by the pyrometer and consequently leading to a lower oven temperature than the actual one.

3) Assumption of Parabolic Flow Pattern

In the microkinetic modeling of experimental gas-phase profiles, the cylindrical shear-flow model was used. For this model, ignoring the presence of the central gas sampling capillary the fully developed front of a fluid flow inside the profile reactor should have a parabolic shape shown Figure 4.5(a). In reality the fluid front profile in the presence of the central capillary is that of flow in an annulus depicted in Figure 4.5(b). This assumption could give discrepancy of experimental and simulated data, especially at the reactor axial centerline.

4) Sampling Volume through Capillary Orifice

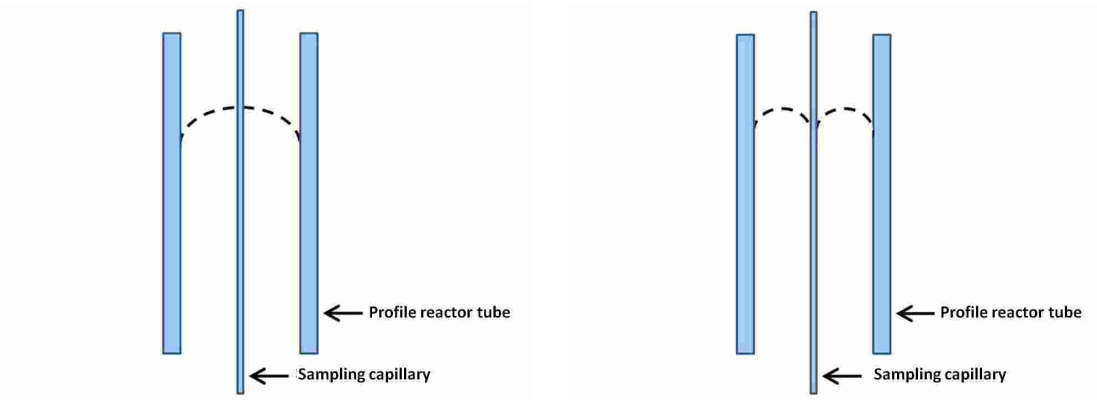

(a) (b)

Figure 4.5: Fluid front profile in modeling: (a) Assumed; (b) Realistic.

To compare with the two-dimensional experimental data, simulation results corresponding only to the reactor centerline were plotted, assuming that the sampling volume through the orifice is not large and thus in the closest vicinity to capillary. However, the exact sampling gas volume through the orifice should be determined by modeling with available tools, e.g., by computational fluid dynamics (CFD), and such modeling is the outlook of this thesis.

Chapter 5

Results and Discussion

5.1 Gas-Phase OCM Experimental Results

Table 5.1 outlines all the experimental conditions for gas-phase OCM experiments done with two capillary orifice diameters. Prior to discussion of experimental results, it should be noted that each profile was measured twice to verify reproducibility of the data. Reproducibility was excellent, and only one out of the doubly measured profiles for each experimental condition is shown in the thesis. Each measurement point in the profiles conveys the reaction at steady state.

Figure 5.1 presents reaction species and temperature profiles at three C/O ratios, as well as two pressure, total flow rate, and temperature values. Positions (mm) of the sampling length between the ordinate axes and dashed vertical lines correspond to the heights of the front and back heat shields. All the sub-figures in this figure are the examples of the earliest experiments done with the 25 μm sampling orifice of a capillary and analysed by the mass spectrometer. In Fig. 5.1(a), oven heating was automatically regulated so that temperature of 500 °C at 2 mm distance above the front heat shield was maintained.

As can be seen, at 1 bar pressure and C/O ratio of 4 in Fig. 5.1(a), reactants conversion does not proceed, as the reaction conditions do not lead to the ignition point upon which chemistry begins. Absence of gas-phase OCM chemistry at 1 bar and typical OCM temperatures was also reported elsewhere [50; 56], and in general can be explained by the Flammability Diagram in Fig. 3.3, according

Table 5.1: Experimental conditions and capillary orifice diameter for gas-phase OCM. Oven temperature indicates the temperature measured in the middle of the oven height, in-capillary temperature is the temperature measured inside the capillary. Given temperatures represent the set temperature as parameter, which is also indicated in labels of plots.

Orifice diameter μ**m**	**C/O ratio**	$\dot{V}_{total}$ **mln · min**$^{-1}$	**p** **bar**	**T in-capillary at 2 mm above FHS** **°C**	**T oven at middle part** **°C**
25	2	2000	4	500	–
25	4	500	1	500	–
25	4	4000	8	400	–
25	4	4000	20	–	880
25	6	4000	20	–	880
25	8	4000	20	–	880
100	2	2000	4	500	–
100	4	2000	4	–	750
100	4	2000	8	–	750
100	4	4000	8	–	750
100	8	2000	8	–	750

to which these conditions render the reactants mixture outside the flammability "envelope". Negative mole fraction values in the sub-figures are due to mass spectra overlapping; for example, some of the oxygenates, like formaldehyde, have the mass-to-charge ratio (m/z) of 30 in a mass spectrum according to the NIST reference spectra [132]. And since ethane (m/z of 30) has a fragment with $m/z = 27$ that should be subtracted from the main ethylene peak area at also $m/z = 27$, it is clear that in the end a higher value of the ethane fragment than necessary is subtracted, making the ethylene flow rate negative. Thus, whereas negativity of the ethylene curve is presumed as the collective formation of oxygenates, deflection of the curve towards positive values of the ordinate axis must indicate ethylene formation. From this particular sub-figure no ethylene formation can be concluded, since the numerical values of the ethylene curve do not increase.

To shed light on what oxygenate species are formed during experiments, the reaction aqueous condensate was analysed after one of the experiments (at C/O=4, 8 bar, 4000 mln·min^{-1}, 880 °C oven temperature), and the analysis result is shown

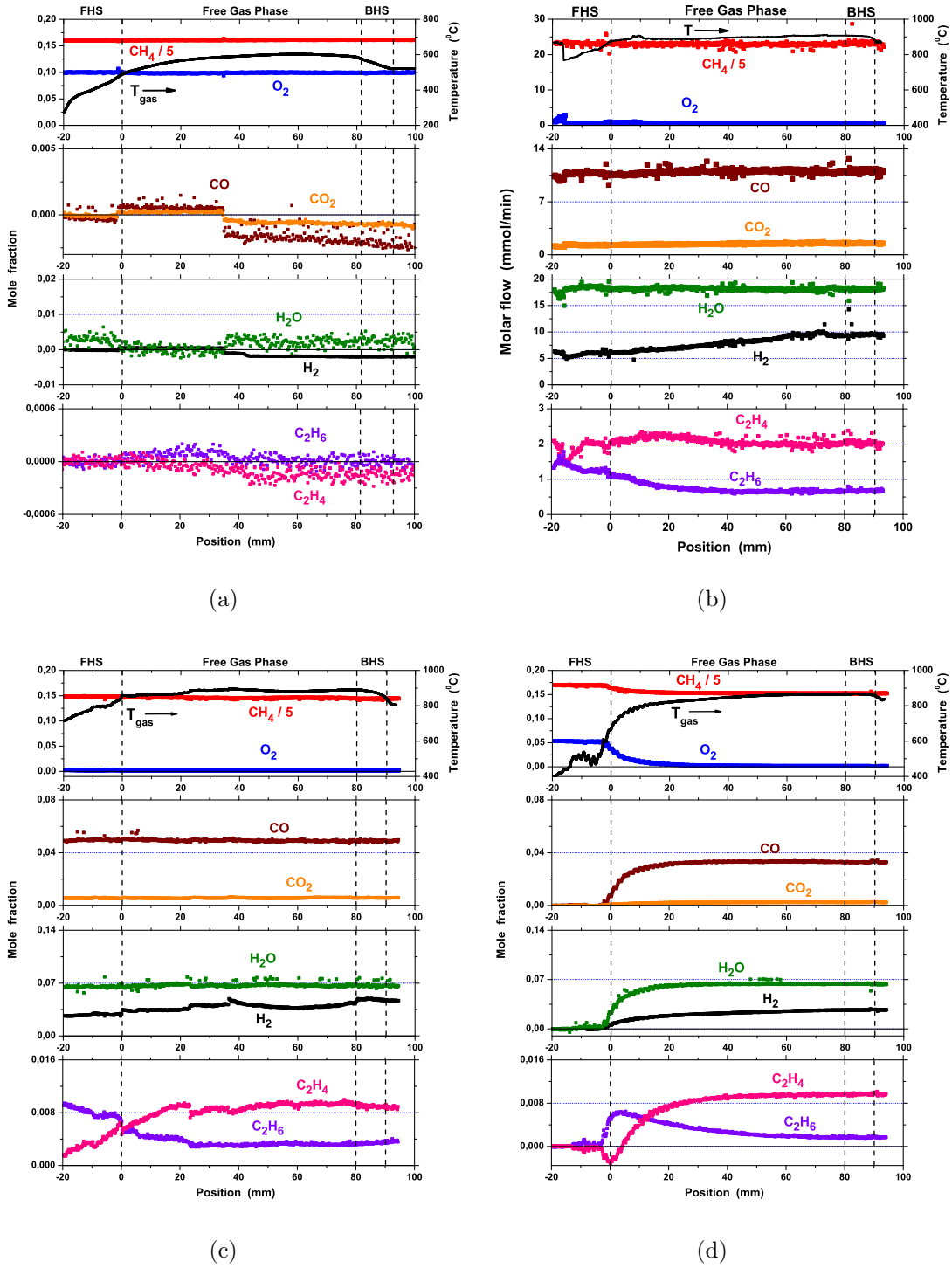

Figure 5.1: Species and temperature profiles at (a) C/O=4, 1 bar, 500 mln·min^{-1} total flow rate and 500 °C at FHS; (b) C/O=4, 20 bar, 4000 mln · min^{-1} and 880 °C; (c) C/O=6, 20 bar, 4000 mln · min^{-1} and 880 °C; (d) C/O=8, 20 bar, 4000 mln · min^{-1} and 880 °C. Species are analysed with the mass spectrometer.

in Figure 5.2. Analysis was done only for one experimental condition and therefore was not systematic [1]. As is seen, the range of formed oxygenates is diverse, and formaldehyde with methanol constitute the major oxygenated hydrocarbons.

At 20 bar pressure and C/O ratios of 4 and 6, however, reaction takes place even before reaching the expected reaction zone: the sub-figures impart the situation at already complete oxygen conversion. It was possible to shift the reaction front into the reactor zone at 20 bar only at the C/O ratio of 8. These results at 20 bar pressure and various stoichiometries allowed to determine the boundaries of experimental conditions for further measurements.

The next set of experiments was performed with a capillary having the 100 μm sampling orifice, and the experimental data is given as symbols and black line in the graphs below. In total, these experimental results represent 5 measurement conditions. The reason for choice of a bigger orifice diameter than 25 μm is to measure gas-phase temperatures more accurately by flushing more gaseous mixture over the in-capillary thermocouple tip. Indeed, the difference in temperature measurements through the two orifice diameters is clearly seen in Figure 5.3. In particular, in the plots that show temperature profiles measured via the 25 μm orifice, temperature slope does not change upon entering the free gas phase. In the plots showing temperature profiles obtained using the 100 μm orifice, however, the temperature slope decreases abruptly on entering the free gas phase. Out of these plots, temperature measured through the 100 μm orifice demonstrates a more physically reasonable situation: heat transfer from the walls of the foam channels to the thermocouple should be higher than from the reactor wall in the bulk free gas phase, therefore temperature decreases. In case of the 25 μm orifice, there seems to be not sufficient heat flux to the thermocouple, and thus contribution from infra-red radiation emitted by the hot oven coils becomes dominant, masking the picture of the real gas temperature. It should be noted that species profiles measured through the both orifices at similar conditions were also similar, although the species profiles corresponding to the temperatures measured via the 25 μm orifice are not shown here.

Moreover, during experiments, blockage of the 25 μm orifice with a blackish liquefied substance was observed – the substance most probably being polycyclic

[1] GC-MS analysis was performed by PhD student Lenard Csepei, FHI.

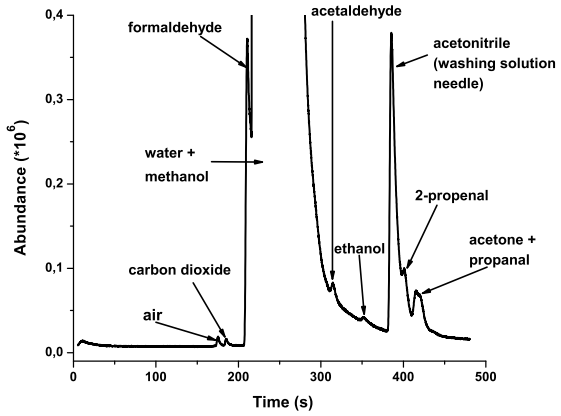

(a)

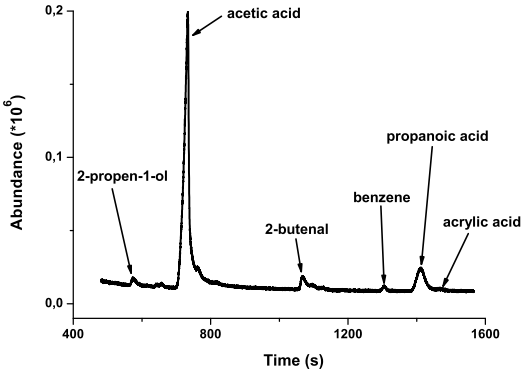

(b)

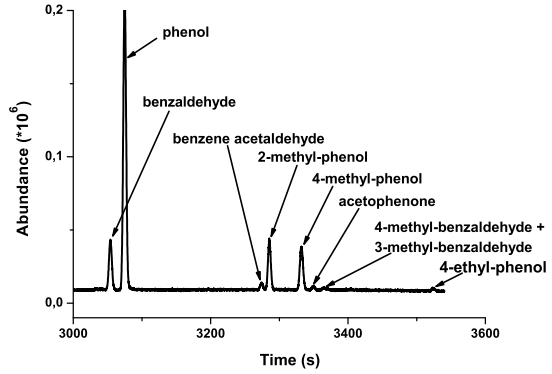

(c)

Figure 5.2: GC-MS (Agilent Technologies) analysis of the aqueous condensate after OCM reaction at C/O=4, 8 bar, 4000 mln $\cdot$ min^{-1}, 880 °C oven temperature conditions. (a) Part I; (b) Part II; (c) Part III. Analysis column: DB – 1

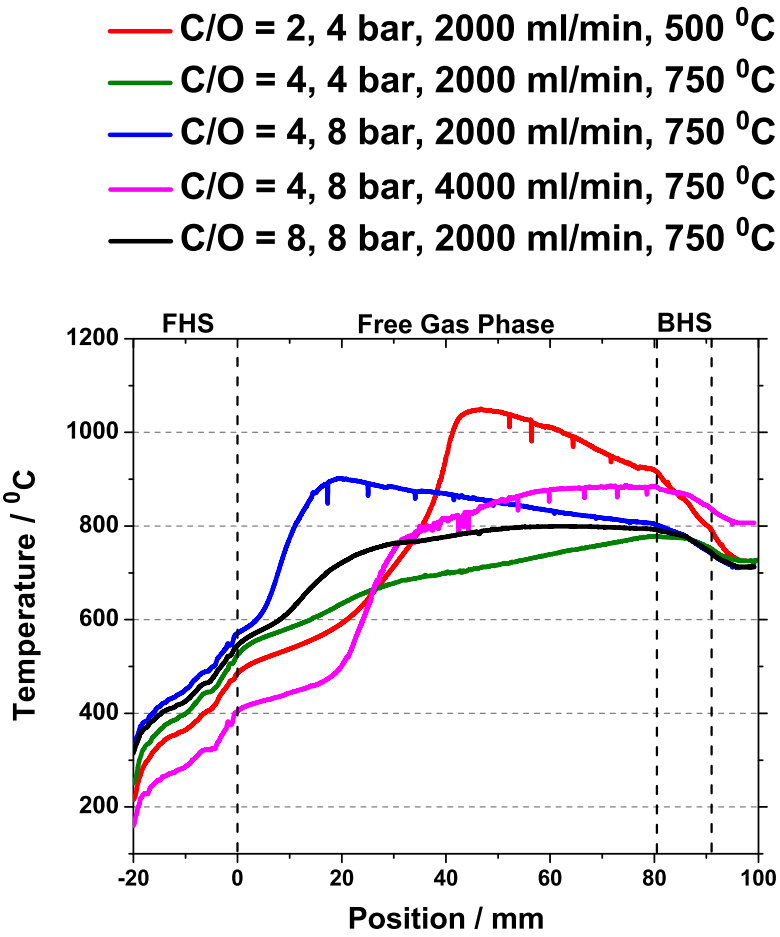

Figure 5.3: Experimental temperature profiles measured within the 25 μm (dashed lines) and 100 μm (continuous lines) orifice capillaries. Colour coding is used for similar conditions.

aromatic hydrocarbons and soot, the formation of which was extensively measured and modeled by some research groups ([80] and references therein). This fact also inspired usage of a larger-diameter orifice.

It should be remembered that in all the graphs showing experimental data obtained with the 100 μm orifice capillary, the temperature of 750 °C corresponds to set oven temperature, whereas the temperature of 500 °C at C/O=2, 4 bar and 2000 mln $\cdot$ min^{-1} flow rate conditions corresponds to in-capillary temperature, as was outlined above in Table 5.1.

The oxygen conversion and product selectivities for experimental data mea-

sured through the 100 μm orifice are given in Figure 5.4. Conversion of oxygen was plotted because it is the limiting reactant, i.e., it is consumed faster than methane. In general, increase of conversion leads to increae of total and partial oxidation products: CO_x, H_2, H_2O. Decrease of ethane selectivity is accompanied by increase of ethylene selectivity, confirming the proposed hypothesis [50] according to which ethylene originates from ethane via consecutive oxidative dehydrogenation. From the standpoint of C_2 hydrocarbons selectivities, the C/O ratio of 8 shows highest selectivities, in compliance with the discussions [29] that lower oxygen partial pressure leads to preservation of the target hydrocarbons from oxidation, albeit at the expense of reactants conversion. Maximal combined yields of C_2 hydrocarbons amounts to 5.2% at C/O = 8 and 7.3% at C/O = 2.

The net specific production rate of an ith component, r_i, in a differentially operated reactor equals the ratio of the moles of species i produced per unit volume of gas phase (for homogeneous system) per second ($\mathrm{mol} \cdot \mathrm{m}^{-3} \cdot \mathrm{s}^{-1}$):

$$r_i = \frac{(F_i - F_{i,0})}{V_{GP}} \tag{5.1}$$

When the yield expression in Eq. 3.15 is substituted into the above equation, the following formula is obtained:

$$r_i = \frac{Y_i \; F_{CH_4,0}}{n_i \; V_{GP}} \tag{5.2}$$

If a reactor operates in an integral mode, these expressions are no longer rates, but rather are defined as space-time yield, STY, of the ith species.

Weisz [133] observed that the space-time yields of most processes of the petrochemical industry fall in a window of approximately 1 to 10 $\mathrm{mol} \cdot \mathrm{m}^{-3} \cdot \mathrm{s}^{-1}$ on an integral-mode reactor operation basis. The lower limit of the window corresponds to prohibitively high investment costs, while the upper limit denotes mass/heat transport limitations. Due to integral mode of spatial profile reactor operation (complete oxygen conversion), the net specific production rates are calculated from the experimental profiles and plotted in Figure 5.5 in order to compare with the STY window of Weisz. For this reason, the ordinate axis in the figure is labeled as space-time yield. From the plots it is seen that the combined STY

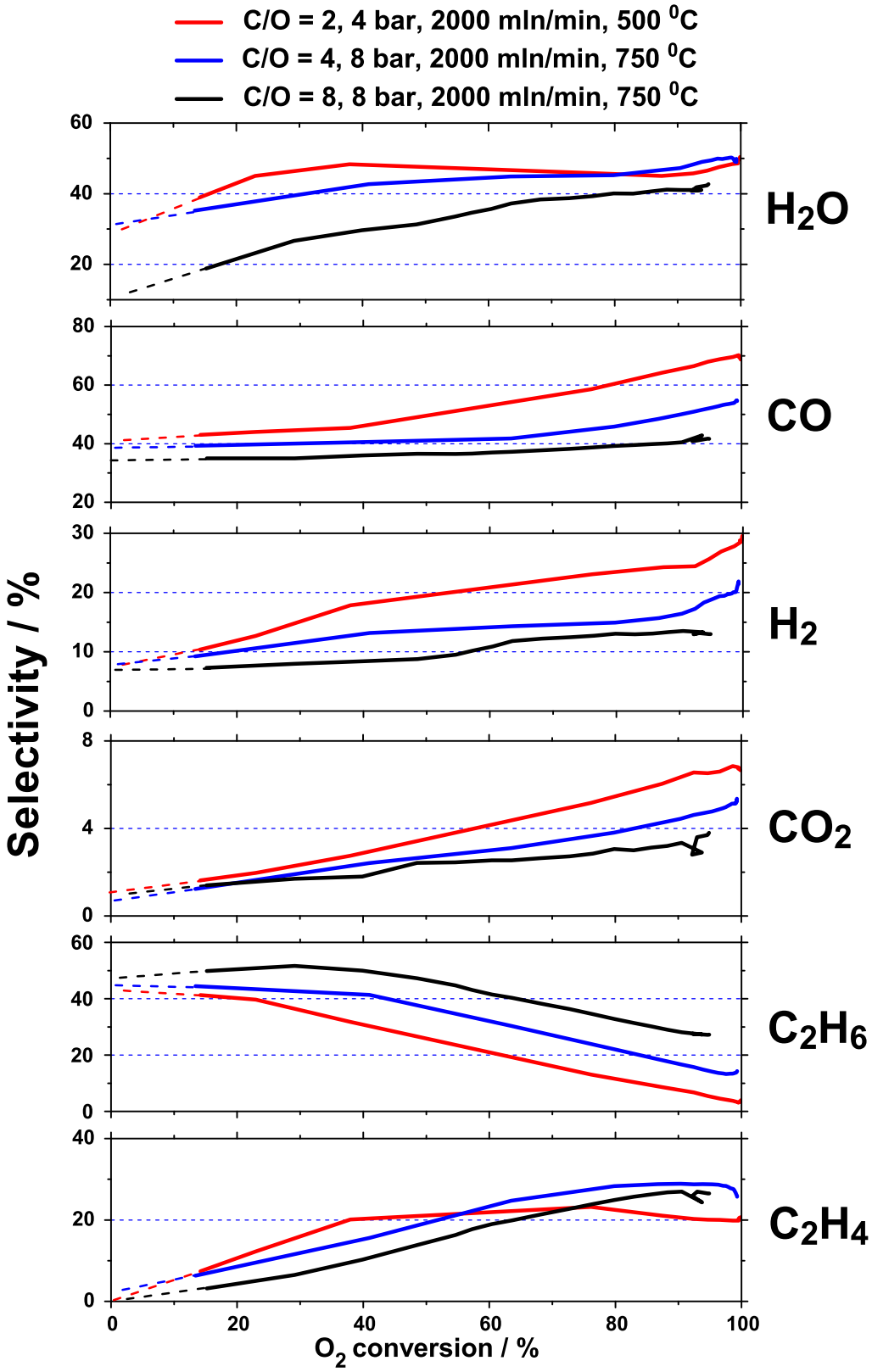

Figure 5.4: Experimental conversion and selectivity (on summed carbon products basis) values. Dashed lines – extrapolation to 0% oxygen conversion.

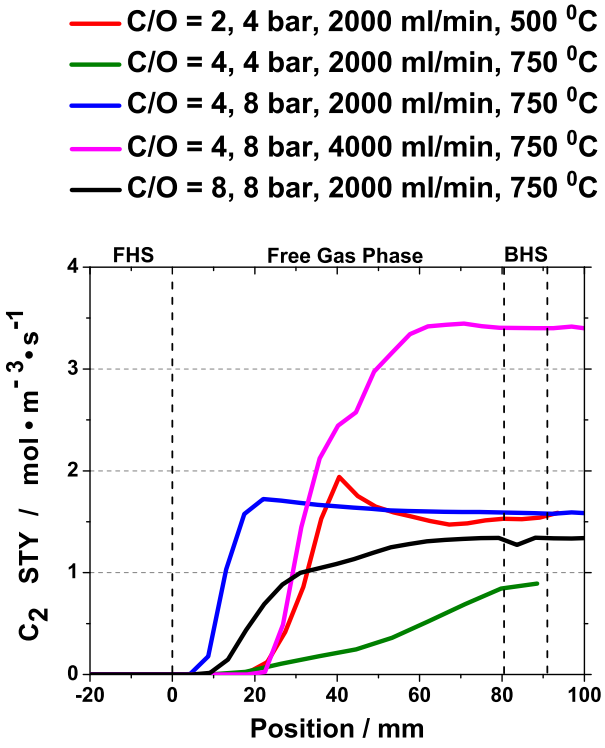

(a)

Figure 5.5: Space-time yield profiles of the target C_2 hydrocarbons at different conditions. Calculated gas-phase volume is that corresponding to the Free Gas Phase.

of ethane and ethylene are within the window for industrial applicability at the pressure of 8 bar, and at 4 bar only at the C/O ratio of 2. Raising the volumetric flow rate twice increases the space-time yield accordingly. Couwenberg [56] noted from his gas-phase OCM experiments in an 8 mm I.D. quartz tubular reactor that the space-time yields of C_2 products are one order of magnitude higher at an inlet methane-to-oxygen molar ratio of 5 than at the ratio of 10. However, in this thesis such a drastic difference in space-time yields depending on the C/O ratio is not observed.

5.2 Modeling the Experimental Gas-Phase OCM Results

5.2.1 Modeling with Dooley et al. [1] Model

The model from Dooley et al. is a very comprehensive, state-of-the-art microkinetic model including H_2, and C_1 – C_4 oxidation chemistry. Comparison of the experimental and simulated results done with the Dooley et al. model is demonstrated in Figure 5.6. Performance of the microkinetic model for all the experimental conditions shows very good qualitative (in shape) agreement of the simulated and experimental temperature profiles. One can conclude good description of the products mole fractions except for fractions of ethane and ethylene based on best agreement of the experimental and simulated temperature profiles in Fig. 5.6(d) at the end of the free gas phase (axial position between 70 and 80.5 mm). At the same time, even better agreement of the temperature profiles within a longer axial interval at C/O ratio of 8 shown in Fig. 5.7(a) does not show such a good simulated description for any of the product mole fractions.

The model captures the crossing of C_2H_6 and C_2H_4 (relative rates of ethane and ethene formation) quite well, and the concentration of ethane is underpredicted in all cases. Ethylene concentration, on the other hand, is predicted well at 4 bar pressure conditions, with underprediction at 8 bar.

The mechanism of Dooley et al. is quite large, containing hundreds of species and more than a thousand reactions. Some computer programmes require a limited number of species; for example, Fluent CFD software can handle maximum of 50 species. This means the original large mechanism should be reduced without significant harm to its performance. In case of mechanisms in this thesis, such reduction was done using the Reaction Mechanism Generator (RMG) software[1] developed in the group of Prof. W. Green at MIT [134]. The reduction procedure included the following steps: CHEMKIN plug-flow reactor simulations for C/O ratios of 2, 4, and 8 were performed. For each simulation, the sensitivity coefficients for the eight species considered – i.e., O_2, CH_4, CO, CO_2, H_2, H_2O, C_2H_4, and C_2H_6 – for all of the reactions were computed. For each species, the reactions

[1]Operations with RMG software were done by Dr. C. F. Goldsmith, FHI

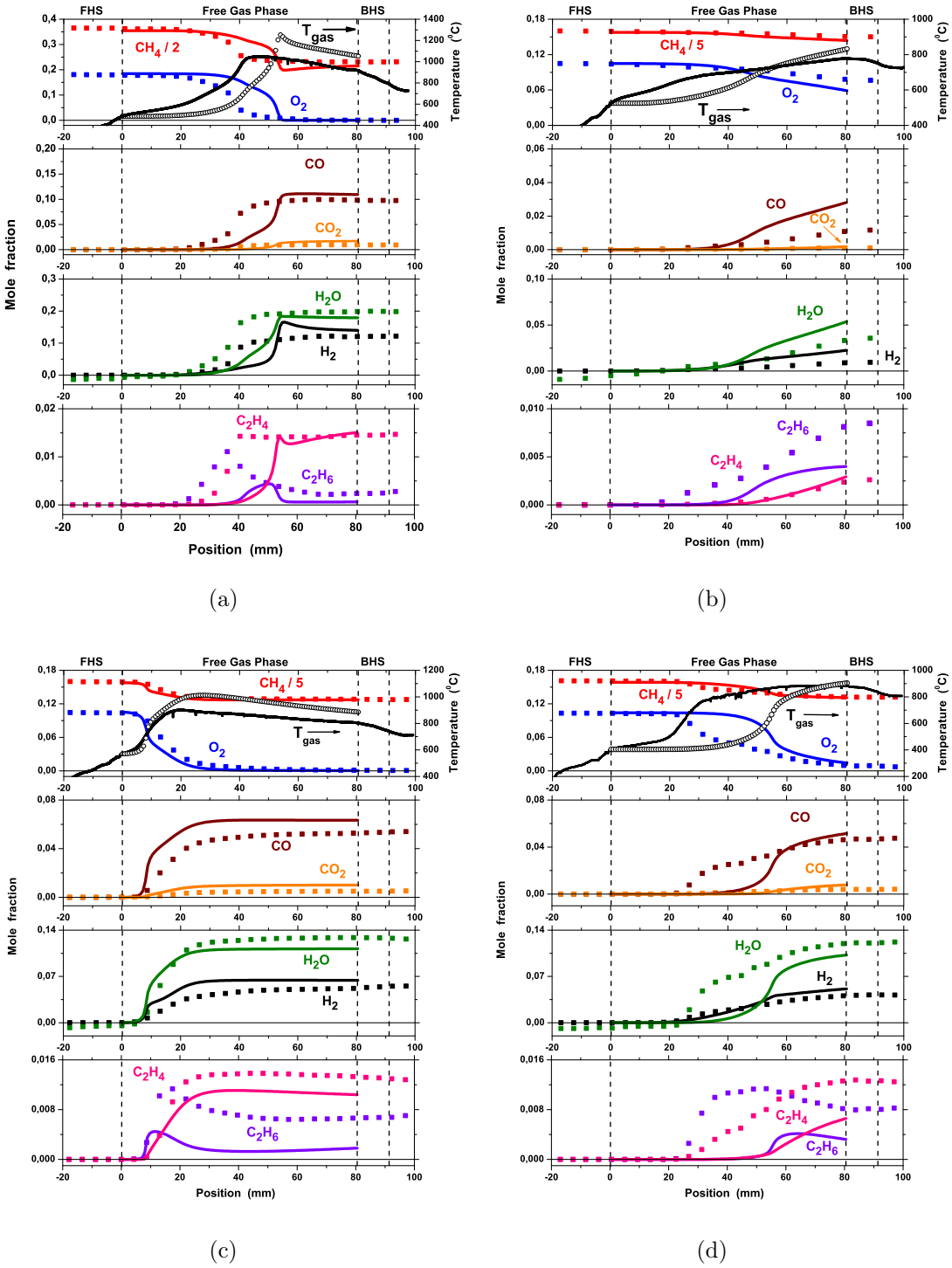

Figure 5.6: Experimental and simulated species and temperature profiles at (a) C/O=2, 4 bar, 2000 mln $\cdot$ min^{-1} and 500 °C; (b) C/O=4, 4 bar, 2000 mln $\cdot$ min^{-1}, 750 °C; (c) C/O=4, 8 bar, 2000 mln $\cdot$ min^{-1}, 750 °C; (d) C/O=4, 8 bar, 4000 mln $\cdot$ min^{-1}, 750 °C. Filled symbols and black line temperature – experimental data; lines and open circle temperature – modeled data. Model of Dooley et al. [1].

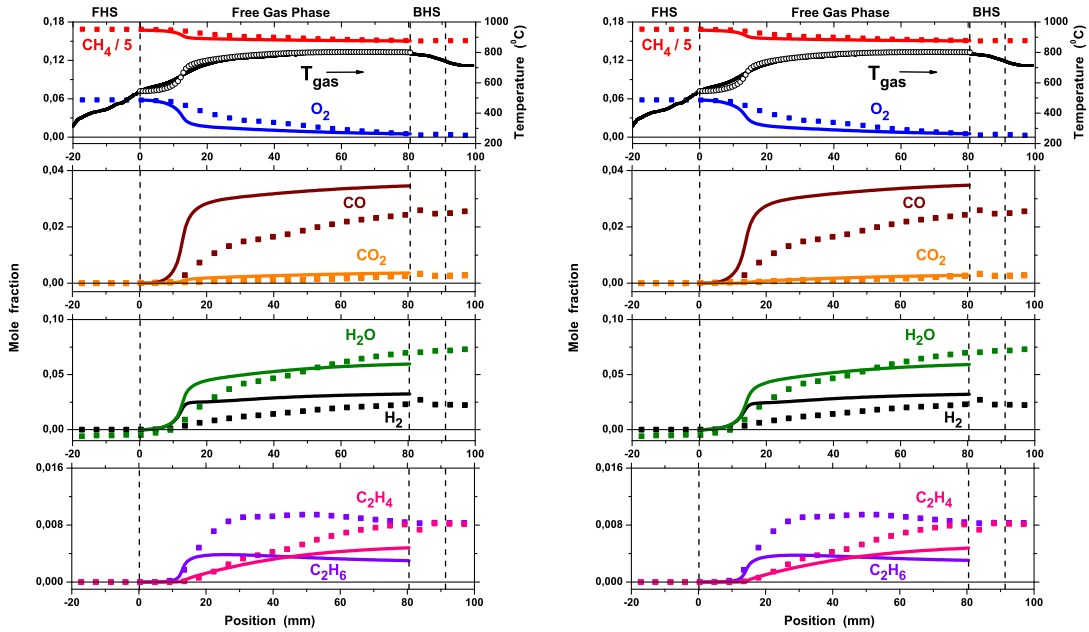

(a) (b)

Figure 5.7: Performance comparison of the full (a) and RMG-reduced (b) Dooley et al. mechanisms for C/O=8, 8 bar, 2000 mln $\cdot$ min^{-1}, and 750 °C temperature conditions. Filled symbols and black line temperature – experimental data; lines and open circle temperature – modeled data.

were sorted in order of descending sensitivity (i.e., most sensitive reactions first). Then this ranking was used to sort each species in the mechanism according to its location in the list of sorted sensitivities (i.e., species that participate in the most sensitive reactions come first). This process was repeated for all 8 species in all 3 reaction conditions. From all the lists of sorted species the average based upon their position in each list was taken. Lower average value indicated higher global sensitivity. For a 50-species mechanism, for example, the first 49 values (Ar being the 50th) were taken. In conclusion, by discarding the least sensitive reactions containing highest average number of locations of a particular species, the original mechanism with 269 species and 1583 elementary reactions was reduced to a mechanism of 50 species and 332 reactions.

Performance comparison of the full and RMG-reduced Dooley et al. mech-

anism in the model is seen in Figure 5.7. Compared graphs can be said to be identical, showing such model reduction approach to be viable.

5.2.2 Modeling with Lopez et al. [2] Model

Few modifications to the mechanism of Lopez et al. were done prior to modeling. Firstly, similarly to the modification to the mechanism of Dooley et al. [1], the PLOG formalism was used for pressure-dependent reactions. Secondly, two reactions were removed from the mechanism: $CH_2OOH^\bullet = CH_2O + OH^\bullet$ and $CH_3CHOOH^\bullet = CH_3CHO + OH^\bullet$. The species $CH_2OOH^\bullet$ and $CH_3CHOOH^\bullet$, correspondingly known to be alpha- and beta-hydroperoxyalkyl radicals, are at most meta-stable points on a potential energy surface, therefore are unlikely to exist and can be removed from the mechanism(s) [135]. While formaldehyde and acetaldehyde may react with OH radicals, they certainly will not form these two removed species. This is important not only because it is physically significant, but also because one cannot estimate transport properties for metastable species. These two radicals are not involved in any other reactions, so removing the two reactions with their participation effectively removes them from the mechanism.

Thirdly, the original mechanism includes the same species with two different names: CH_2CCH_3 and CH_3CCH_2. The former is not included in a single reaction, and was removed from the species list. Lastly, the following three species were not included in the transport file of the original mechanism: OCHCHO (glyoxal), CH_2CHOO (vynylperoxyl), and CYCOOC. (a cyclic isomer for vinylperoxyl). For these three species, the transport properties were computed using the RMG [134] software.

Figure 5.8 presents modeling results with the Lopez et al. model. In Fig. 5.8(a) the higher simulated H_2 concentration than that of H_2O at the highest simulated temperature might give a supposition of approach to thermodynamic equilibrium, at which H_2 and CO are the favoured major products [106]. However, thermodynamic equilibrium calculations with EQUIL package of CHEMKIN shows that thermodynamic equilibrium is still not attained. Change of the slopes of the experimental reactants curves is sensitive to a change of the experimental temperature profile. However, in none of the experimental reactant curves the slope

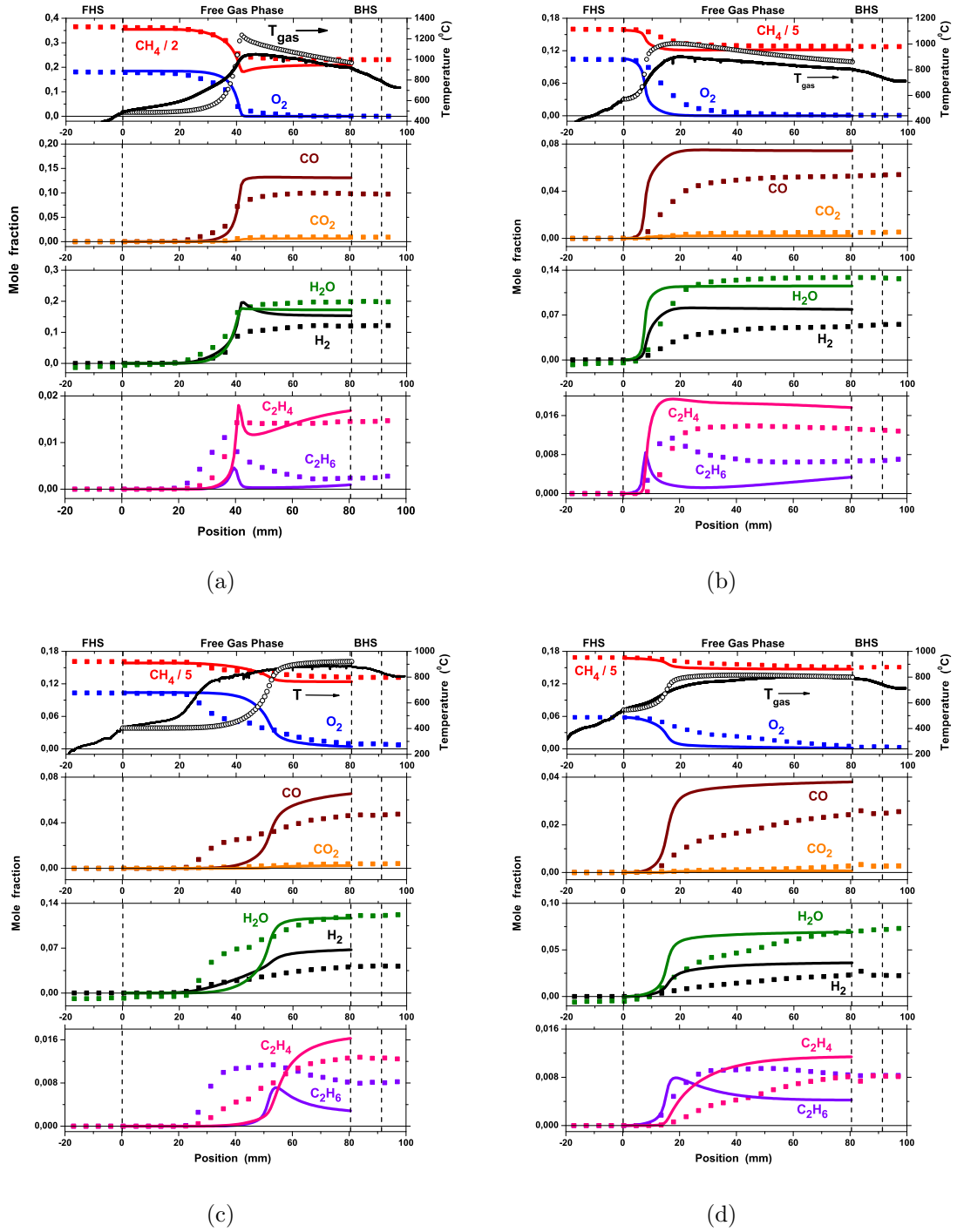

Figure 5.8: Experimental and simulated species and temperature profiles at (a) C/O=2, 4 bar, 2000 mln · min^{-1} and 500 °C; (b) C/O=4, 8 bar, 2000 mln · min^{-1} and 750 °C; (c) C/O=4, 8 bar, 4000 mln · min^{-1}, 750 °C; (d) C/O=8, 8 bar, 2000 mln · min^{-1}, 750 °C. Filled symbols and black line temperature – experimental data; lines and open circle temperature – modeled data. Model of Lopez et al. [2].

changes so abruptly as compared to modeled slopes of the reactants after modeling with the two demonstrated models: the experimental reactants curves are smooth with more or less constant slopes even when the slope of the temperature curve changes substantially. Such a result of the simulation is not at all surprising, because axial diffusion is neglected per definition for the cylindrical shear-flow model. Nevertheless, from comparison, Lopez et al. model shows even a higher sensitivity of the reactant curves slopes to temperature than Dooley et al. model does. The latter mechanism demonstrates better agreement of the slopes of the simulated and experimental reactants profiles.

Analogous comparison of the experimental and simulated data in relation to the reaction products and with simulated product profiles from Dooley et al. model can be done with profiles at 8 bar pressure in Fig. 5.8(c) and 5.8(d), where the simulated temperature profiles qualitatively and partially quantitatively agree well with the experimental temperature profiles. This comparison shows that Lopez et al. model overpredicts CO, H_2 concentrations and the rate of C_2H_6 oxy-dehydrogenation to ethylene.

5.2.3 Modeling with Warnatz et al. [3] Model

Figure 5.9 demonstrates the modeling data when the model of Warnatz et al. [3] was used. As in modeling results with the previous two mechanisms, the best agreement for experimental and modeled temperatures is observed at C/O ratio of 8, 8 bar and 2000 $\text{mln} \cdot \text{min}^{-1}$ conditions; similarly, the simulated temperature development at C/O=4, 8 bar and 4000 $\text{mln} \cdot \text{min}^{-1}$ conditions shows striking resemblance to the temperatures of the previous two models.

Despite the concerted underprediction of the C_2 hydrocarbons molar fractions, their qualitative development along the whole length of the axial coordinate and the relative molar fractions (relative to each other) at the end of the free gas phase is predicted quite precisely. At the same time, the crossing point of the C_2 hydrocarbons is simulated poorly, which is expressed in their simultaneous formation whilst the experimental curves show clear offset between them. Despite its design for stoichiometric combustion, the model simulates methane-rich chemistry quite satisfactorily.

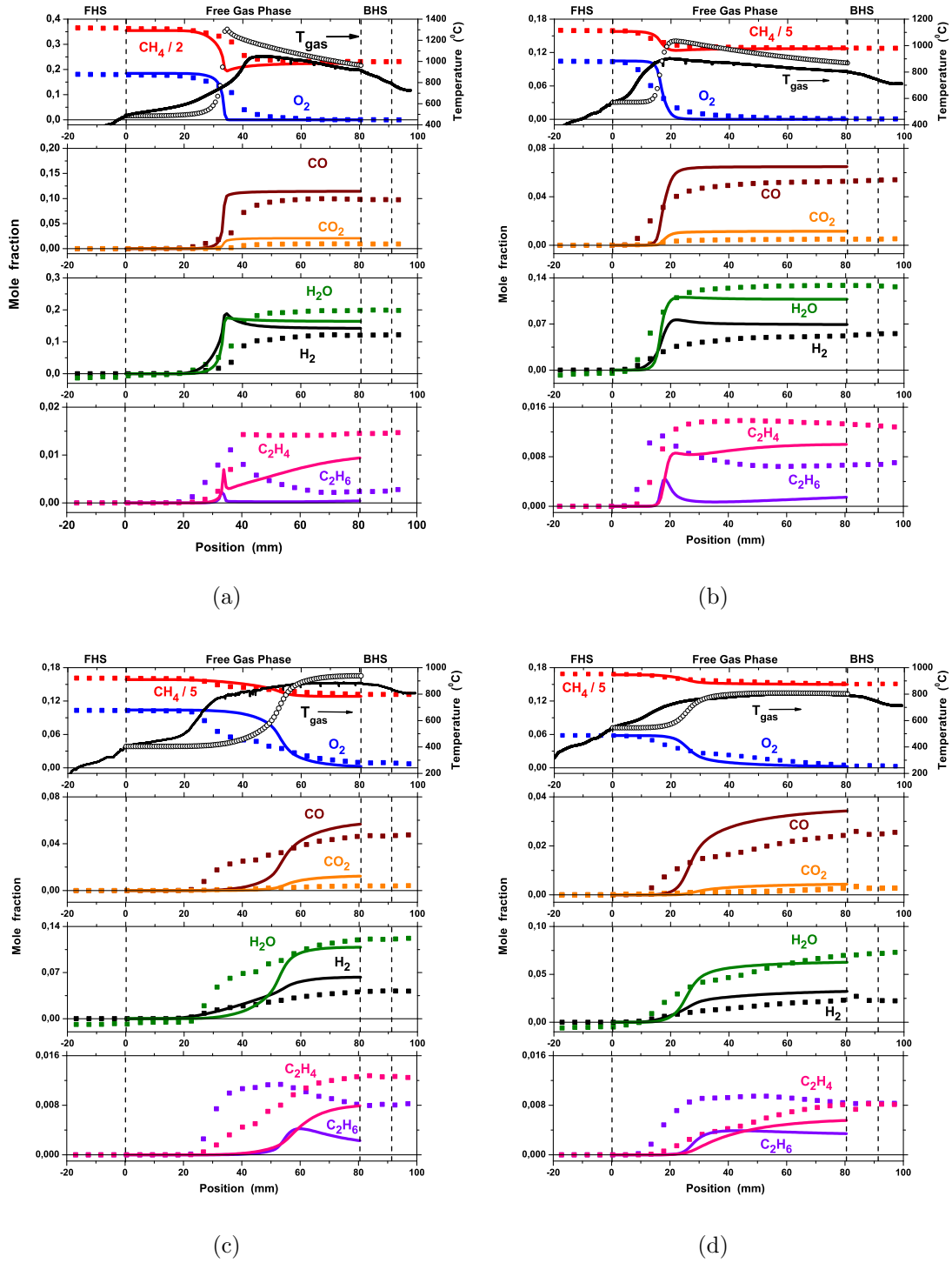

Figure 5.9: Experimental and simulated species and temperature profiles at (a) C/O=2, 4 bar, 2000 mln · min^{-1} total flow rate and 500 °C; (b) C/O=4, 8 bar, 2000 mln·min^{-1}, 750 °C; (c) C/O=4, 8 bar, 4000 mln·min^{-1}, 750 °C; (d) C/O=8, 8 bar, 2000 mln · min^{-1}, 750 °C. Filled symbols and black line temperature – experimental data, lines and open circle temperature – modeled data. Model of Warnatz et al. [3].

5.2.4 Modeling with Konnov [4] Model

The model of Konnov et al. [4] is optimised for modeling combustion of small hydrocarbons. Figure 5.10 shows the results of modeling using the mechanism from Konnov [4]. More or less best prediction of experimental mole fractions is observed at C/O ratio of 8, and the modeling results look similar to those obtained using the mechanism of Warnatz et al. [3]. This is a somewhat unexpected result, since performance of the model for C/O ratio of 8 is better than for the lower C/O ratios which are closer to methane combustion stoichiometry (C/O = 0.25).

Comparison of the rate constant parameters of some arbitrarily selected elementary reactions of these two mechanisms shows almost identical values of pre-exponential factors and temperature exponents, although the activation energies often differ substantially. At the same time, the crossing point of ethane and ethylene is better described by Konnov mechanism. In general, the Konnov mechanism, as the previously discussed ones, also underpredicts concentrations of the C_2 hydrocarbons.

5.2.5 Modeling with Mims et al. [5] Model

Even though pressure dependencies and third-body efficiencies are ignored in the model of Mims et al., it in general gives good simulated mole fractions at the end of the free gas phase for most of the reaction products at correct temperature values, as is demonstrated in the simulation results in Figure 5.11. Indeed, at roughly correctly predicted temperature at axial position interval of 70–80 mm, the experimental and simulated product mole fractions coincide well except for the mole fraction of ethane. Also the familiar overprediction of the simulated H_2 mole fraction profile at C/O ratio of 2 (Fig. 5.11(a)) is accompanied by overpredicted profile of only C_2H_4 species, with correct quantitative prediction for CO species profile.

5.2.6 Modeling with Wang et al. [6] Model

Many elementary reactions in the mechanism of Wang et al. [6] were adopted from GRI 3.0 mechanism and thus contain pressure dependencies and third body

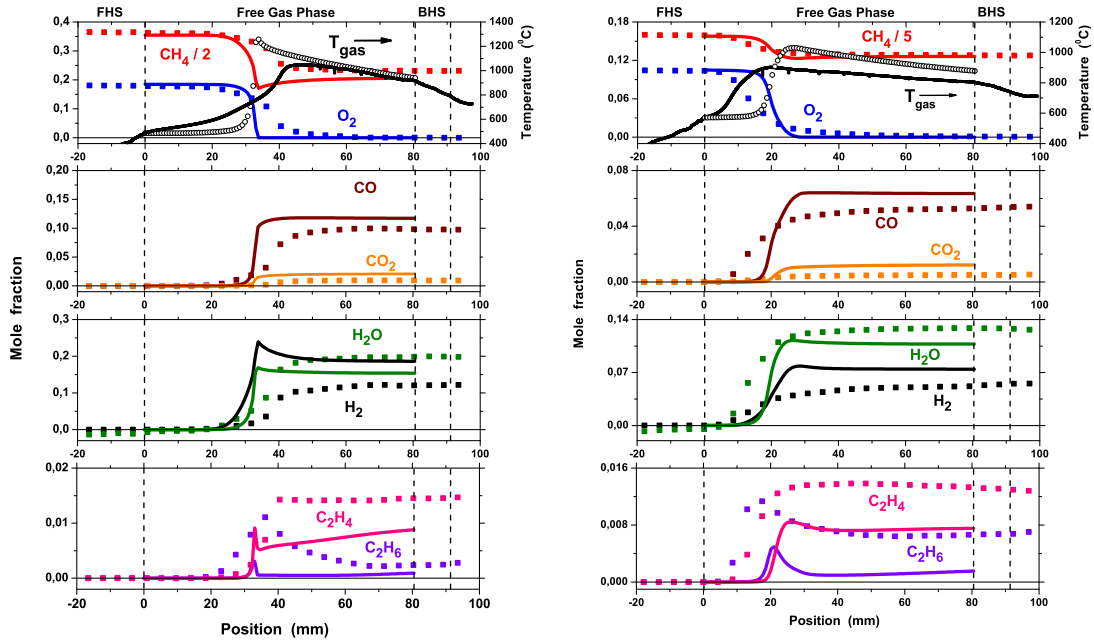

(a)

(b)

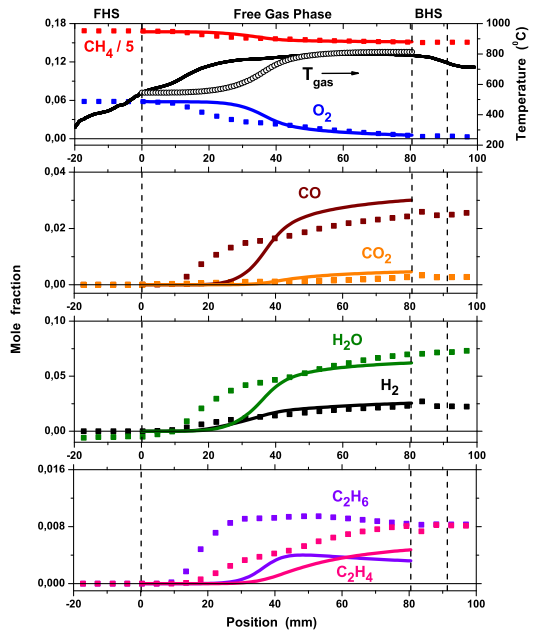

(c)

Figure 5.10: Experimental and simulated species and temperature profiles at (a) C/O=2, 4 bar, 2000 mln $\cdot$ min^{-1} total flow rate and 500 °C; (b) C/O=4, 8 bar, 2000 mln $\cdot$ min^{-1}, 750 °C; (c) C/O=8, 8 bar, 2000 mln $\cdot$ min^{-1}, 750 °C. Filled symbols and black line temperature – experimental data, lines and open circle temperature – modelled data. Model of Konnov [4].

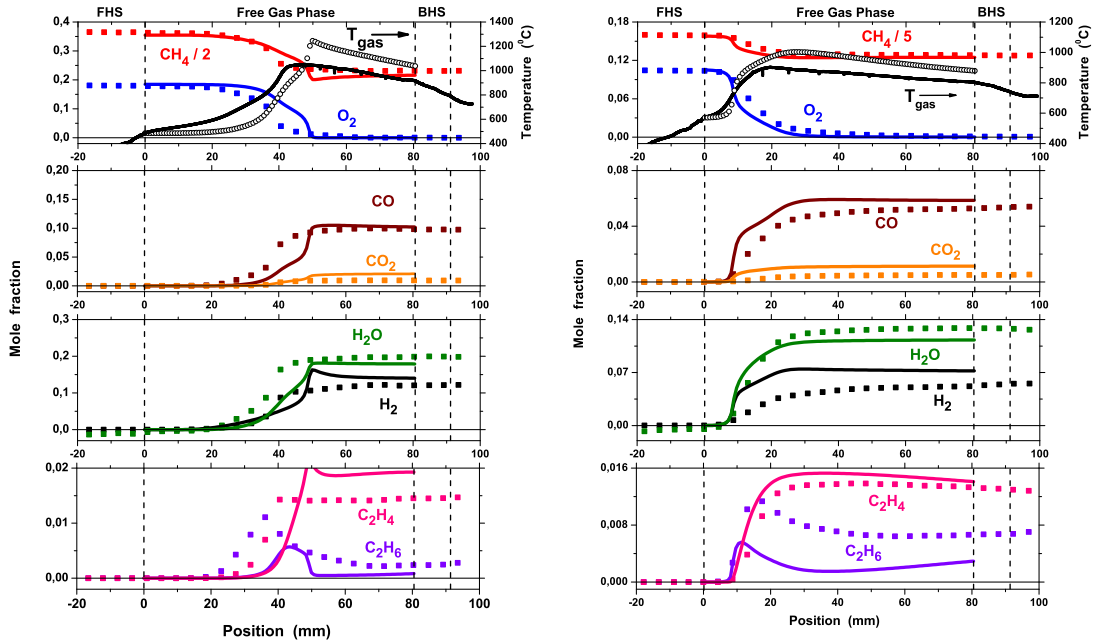

(a)

(b)

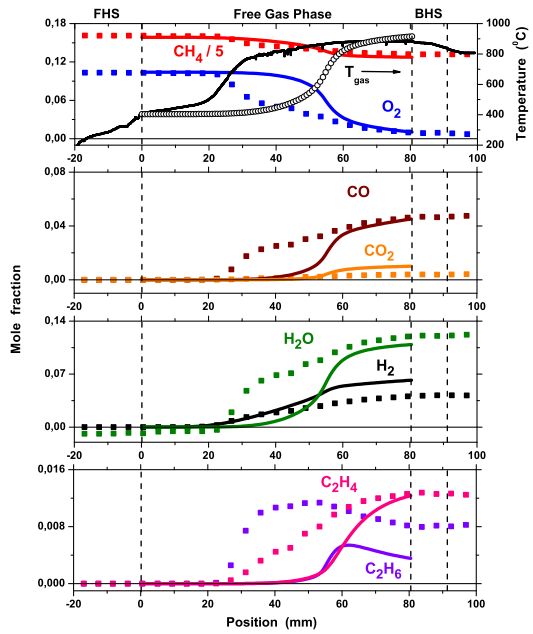

(c)

Figure 5.11: Experimental and simulated species and temperature profiles at (a) C/O=2, 4 bar, 2000 mln $\cdot$ min^{-1} total flow rate and 500 °C; (b) C/O=4, 8 bar, 2000 mln $\cdot$ min^{-1}, 750 °C; (c) C/O=4, 8 bar, 4000 mln $\cdot$ min^{-1}, 750 °C. Filled symbols and black line temperature – experimental data, lines and open circle temperature – modelled data. Model of Mims et al. [5].

efficiencies. Owing to this pressure dependency, comparison of the experimental and simulated results, as given in Figure 5.12, shows the model to be more sensitive to pressure than to C/O ratio, as is seen from a drastic difference of simulated results at 4 and 8 bar pressures. Simulated profiles at 8 bar (Fig. 5.12(c)) demonstrate the rate of ethane oxy-dehydrogenation to ethylene is too high, as is inferred from over- and under-predicted ethylene and ethane profiles, respectively. The model of Wang et al. was comprehensively validated against various experimental reactor set-ups and parameters. Nevertheless, despite its comprehensiveness, the model exhibits poor performance in modeling fuel-rich methane oxidation.

5.2.7 Modeling with Zanthoff and Baerns [7] Model

The mechanism of Zanthoff and Baerns [7] is rather simple, embracing species up to maximum 3 carbon atoms and containing reactions with no pressure dependencies nor third body efficiencies. In spite of its specific creation for OCM, i.e, fuel-rich methane oxidation, the results as given in Figure 5.13 at 4 bar pressure do not show ignition of reaction, resembling performance of a model designed for methane combustion (model by Wang et al. [6], for instance). Very rapid chemistry at 8 bar pressure is a highly improbable occurrence for a cylindrical shear-flow model and is rather a numerical artefact suggesting re-evaluation of kinetic parameters in the mechanism.

5.2.8 Comparison of Models and Conclusions from Models Testing

The models of Hughes et al. [8], GRI 3.0 [10] showed numerical instabilities and could not converge to solution for cylindrical shear-flow model. For these models, plug-flow reactor model simulations were performed to get insight into their overall performance. Figure 5.14 shows comparison of the performance of the models on the basis of how well they predict the experimental reactant profiles when the cylindrical shear-flow reactor model (CSFM) equations were applied. Additionally the microkinetic model of Sun et al. [9] is added to the comparison

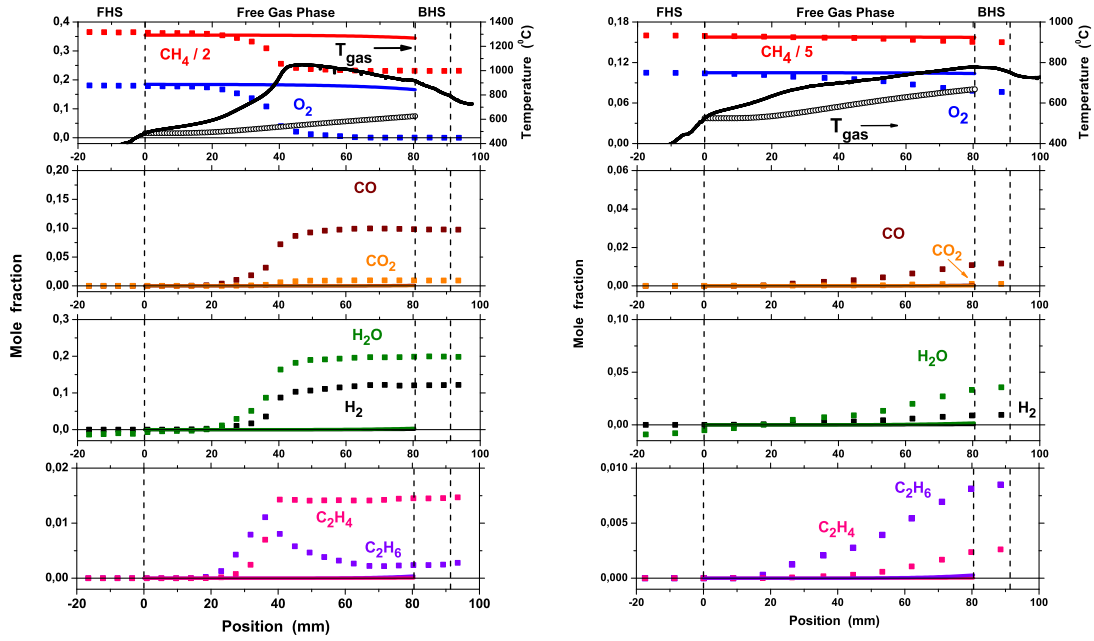

(a) (b)

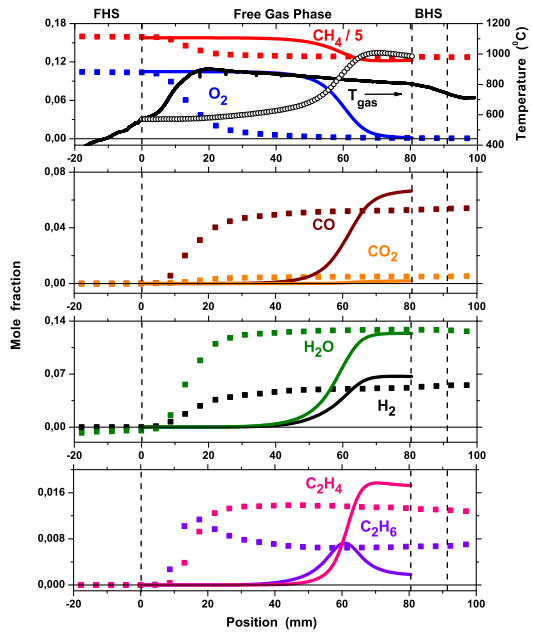

(c)

Figure 5.12: Experimental and simulated species and temperature profiles at (a) C/O=2, 4 bar, 2000 mln $\cdot$ min^{-1} total flow rate and 500 °C; (b) C/O=4, 4 bar, 2000 mln $\cdot$ min^{-1}, 750 °C; (c) C/O=4, 8 bar, 2000 mln $\cdot$ min^{-1}, 750 °C. Filled symbols and black line temperature – experimental data, lines and open circle temperature – modelled data. Model of Wang et al. [6].

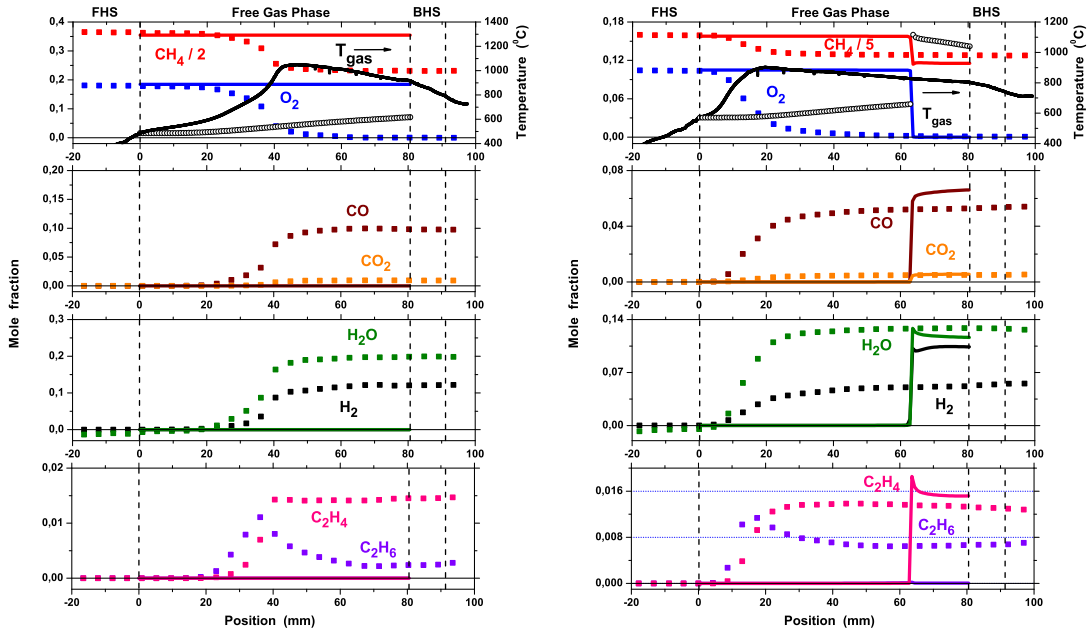

(a) (b)

Figure 5.13: Experimental and simulated species and temperature profiles at (a) C/O=2, 4 bar, 2000 mln · min^{-1} total flow rate and 500 °C; (b) C/O=4, 8 bar, 2000 mln · min^{-1}, 750 °C. Filled symbols and black line temperature – experimental data, lines and open circle temperature – modeled data. Model of Zanthoff and Baerns [7].

plots.

From comparison it is seen that the models of Zanthoff and Baerns, Wang et al. and Sun et al. deviate widely from the experimental curve, showing too little conversion. The models of Warnatz et al., Konnov and Lopez et al. demonstrate too high rates of conversion. Qualitatively, models of Mims et al. and Dooley et al. yield slopes closest to the slope of the experimental curve. The ignition-delay time at lower pressures (at 4 bar in particular in this graph) still is not described accurately by any of the models, apparently owing to the fact that the CSFM does not take into account axial diffusion of species. With the models of Warnatz et al. and Konnov, methane profiles monotonously rise after complete oxygen conversion, and this rise is not methane diffusion from the reactor wall to the axial centerline, but rather a numerical response to change of total number of

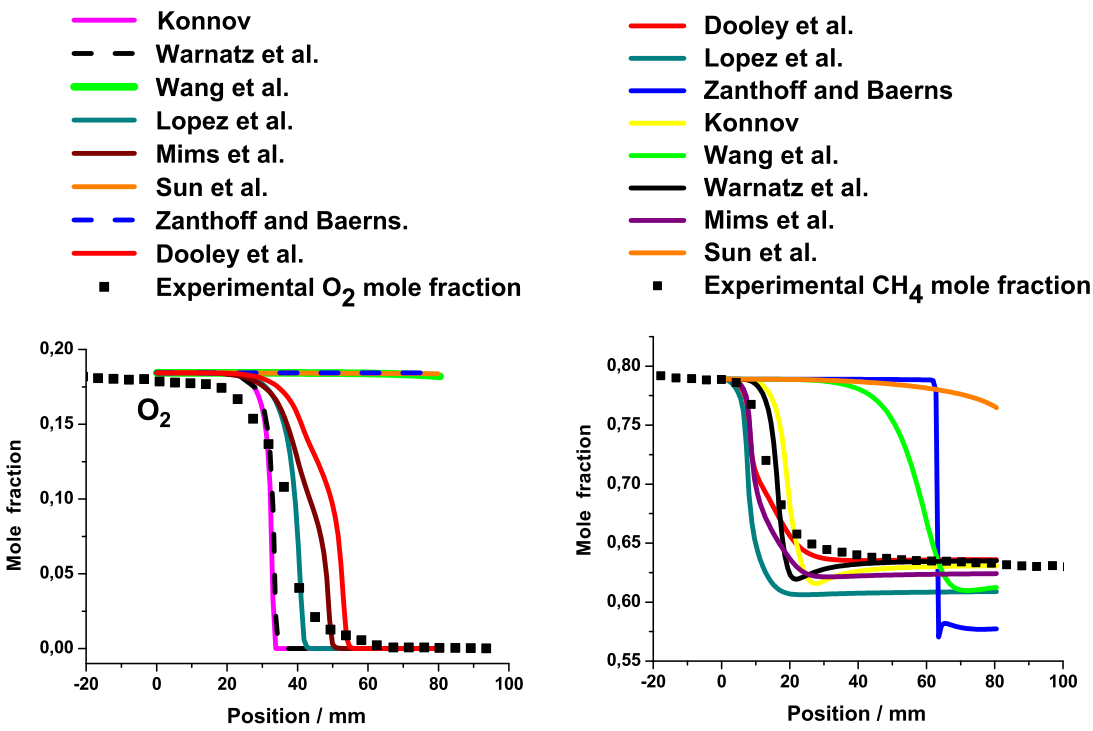

(a) (b)

Figure 5.14: Comparison of profiles of the experimental and simulated data with the cylindrical shear-flow reactor model for (a) O_2 species at C/O=2, 4 bar, 2000 mln $\cdot$ min^{-1} and 500 °C conditions; (b) CH_4 species at C/O=4, 8 bar, 2000 mln $\cdot$ min^{-1}, 750 °C. Symbols – experimental data; lines – modeled data.

moles.

Similar comparison of the models, but with the plug-flow reactor model (PFM) applied, is illustrated in Figure 5.15. The reason for application of the PFM is to compare the microkinetic models at equal temperature values, and for that purpose the experimental temperature profiles as input were used. As is expected with the plug-flow model which assumes limitless radial diffusion rate, the start of ignition is shifted towards reactor entrance for all the models. The models which showed worst results with the CSFM (of Wang et al., Sun et al., Lopez et al. and Zanthoff and Baerns), also gave results with significant errors in case of PFM. The models of Warnatz et al. and of Konnov, which exhibited too intensive conversion with CSFM, in fact perform satisfactorily with PFM, and the models

which showed almost no ignition in the CSFM unexpectedly showed excessively high conversions. Considering that CSFM is more close to real flow scenario, the plots show how misleading a PF model can be.

All the models showed overpredicted hydrogen concentrations for C/O ratio of 2 at 4 bar pressure, even inverse H_2O/H_2 for Konnov model, and quite often this overprediction is accompanied by excessive CO and/or C_2H_4 mole fractions. For C_2 hydrocarbons, there is either underprediction of both ethane and ethylene (models of Konnov, Warnatz et al., Dooley et al.), or too high rate of ethane dehydrogenation to ethylene (models of Lopez et al., Wang et al.). In light of calculated ethane and ethylene mole fractions relative to each other, particularly noteworthy is that the model by Dooley et al. and of Konnov predict a slower rate of ethane oxidative dehydrogenation to ethylene than all the other models leading to the experimentally observed crossover of the C_2H_6 and C_2H_4 profiles. Qualitative reproduction of this particular feature is important. As a general summary of the models testing and intermodel comparison, it can be stated that model by Dooley et al. [1] performs most satisfactorily for fuel-rich methane oxidation for considered experimental conditions, except for crossover of H_2 and H_2O curves.

Finally one can state that none of the used microkinetic models described the species and temperature profiles for fuel-rich methane oxidation quantitatively precisely. A plausible explanation for such non-precise description can be that earlier sophisticated models have been developed and validated for methane combustion conditions, whereas the models designed for OCM specifically have not yet reached that level of precision achieved by repeated model re-evaluation as in the case of stoichiometric combustion. Overall, the models by Dooley et al. and Mims et al. showed in cylindrical shear-flow simulations good agreement with the experimental data and were therefore selected for further detailed analysis.

5.2.9 Detailed Analysis of Microkinetic Models

From all the simulation results with the cylindrical shear-flow, as well as plug-flow reactor models, the mechanism of Dooley et al. showed a very good prediction for the experimental curves. To analyse this mechanism in a more detail, the

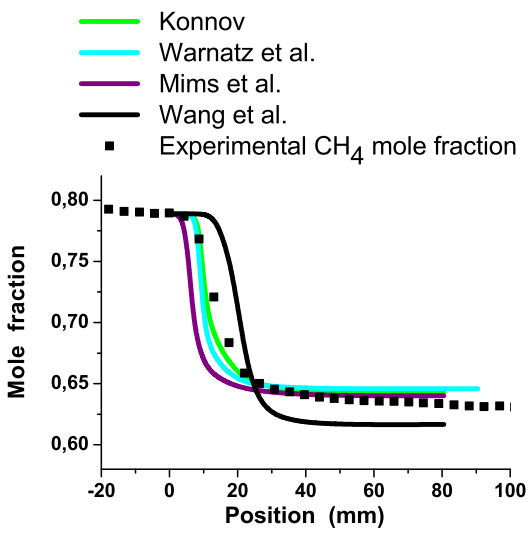

(a)

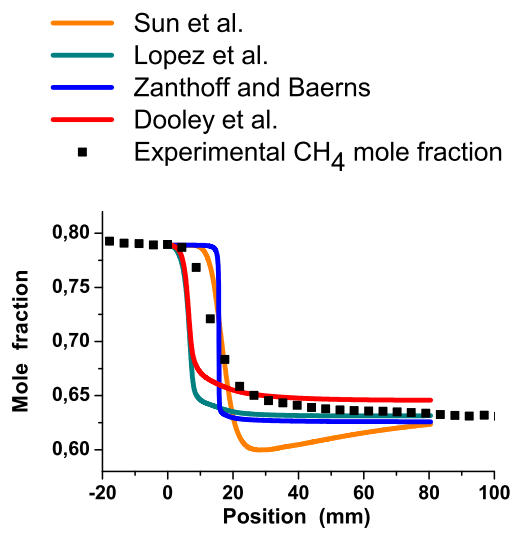

(b)

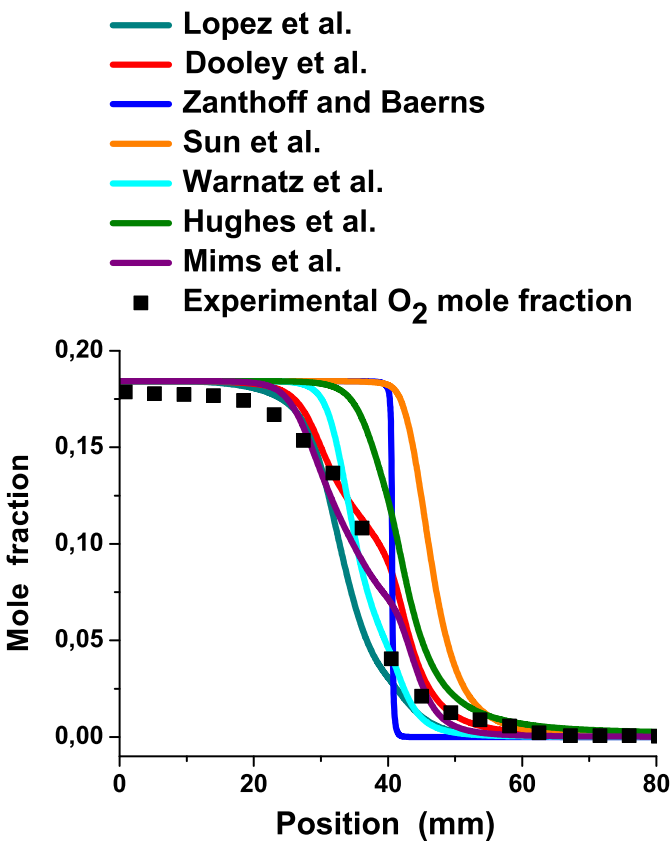

(c)

Figure 5.15: Comparison of profiles of the experimental and simulated data with the plug-flow reactor model for (a) and (b): CH_4 at C/O=4, 8 bar, 2000 mln $\cdot$ min^{-1} and 750 °C conditions; (c) for O_2 at C/O=2, 4 bar, 2000 mln $\cdot$ min^{-1} and 500 °C conditions. Symbols – experimental data; lines – modeled data.

reaction path analysis (RPA) was done at 4 positions on the axial profile: at the beginning of the free gas phase (position 0 mm); at a point slightly before the reactants conversion commence (position 19 mm); at 19% methane and 47% oxygen conversion, which also approximately corresponds to the peak of ethane production (position 50 mm); and finally, at the end of the free gas phase (position 80.5 mm) under full oxygen and 39% methane conversion conditions. The conditions of C/O=2, 4 bar, 2000 mln $\cdot$ min^{-1} and 500 °C were chosen for RPA analysis. The methane consumption rate was 1.4E-7, 4E-5, 3.5E-1 and -6.1E-3 mol $\cdot$ m^{-3} $\cdot$ s^{-1} for axial positions of 0, 19, 50 and 80.5 mm, respectively. Negative consumption rate is due to increase of methane mole fraction curve (Fig. 5.6(a)) with decrease of total mole number; in principle the methane consumption rate at this position is 0 mol $\cdot$ m^{-3} $\cdot$ s^{-1}.

The percent numbers in the RPA correspond to consumption of species which are at the beginning of arrows, and each arrow denotes relative rate analysis for a particular species. A relative rate analysis can be accomplished while each reaction is split; it calculates the ratio of the rate of a jth reaction consuming an ith species to the total rates of all reactions depleting this species. This scaling helps to determine which reaction has the largest influence on the removal of a species locally [118]. It should also be noted that not all of the major pathways are shown in the network, but they are nevertheless discussed.

RPA done at the beginning of the free gas phase (position 0 mm) corresponds to the initiation regime. At this position, methane can be activated through the only reaction channel (also given as R-n 2.1):

$$CH_4 + O_2 = CH_3^{\bullet} + HO_2^{\bullet} \tag{5.3}$$

No subsequent reactions of produced methyl or of hydroperoxyl radicals are distinguished at this position.

RPA of species slightly after ignition, corresponding to ca. 0.13% CH_4 and O_2 conversion, is shown in Figure 5.16. At this axial position, the majority of methane is activated by OH radicals, and afterwards, in the chain-propagation regime, 65.3% of reactant oxygen converts almost half of the generated methyl radicals to methylperoxy radicals, and formation of ethane from coupling of

methyl radicals is negligibly little. Nevertheless, the formed ethane is a precursor for C_{3+} hydrocarbons from which ethylene is formed (also a negligible pathway at this axial position). For example, most of ethylene is formed by decomposition of ethylperoxyl radicals:

$$C_2H_5O_2^\bullet = C_2H_4 + HO_2^\bullet \tag{5.4}$$

Ethylperoxy radicals were generated after oxygen reaction with ethyl radicals, wherein ethyl radicals originate not from ethane, but from other species, e.g., by decomposition of ethyl-methylene ketone (butanon-1yl) or propionyl radical:

$$C_2H_5COCH_2^\bullet = C_2H_5^\bullet + CH_2CO^\bullet \tag{5.5}$$

$$C_2H_5CO^\bullet = C_2H_5^\bullet + CO \tag{5.6}$$

The main formation channels of propionyl radicals, $C_2H_5CO^\bullet$, are via decomposition of propyl aldehyde, $C_2H_5CHO^\bullet$, by the same radicals which in principle activate initial methane, viz., H, OH, HO_2, CH_3 and CH_3O_2 radicals. Among other less significant channels of ethyl radical formation are unimolecular decomposition of propoxy, but-1en-3yl and but-2oxy radicals:

$$NC_3H_7O^\bullet = C_2H_5^\bullet + CH_2O \tag{5.7}$$

$$C_4H_{7\ 1-3}^\bullet = C_2H_5^\bullet + C_2H_2 \tag{5.8}$$

$$SC_4H_9O^\bullet = C_2H_5^\bullet + CH_3CHO \tag{5.9}$$

Oxygen "regeneration" can occur by methylperoxy radical consumption reactions:

$$CH_3O_2 + HO_2^\bullet = O_2 + CH_3O_2H \tag{5.10}$$

$$2CH_3O_2^\bullet = O_2 + 2CH_3O^\bullet \tag{5.11}$$

Also in agreement with the literature works discussed in Chapter 2, the main products at this temperature and pressure (4 bar) are oxygenates formaldehyde and methanol, with non-significant production of carbon monoxide.

Two main steps for formation of the hydroperoxy radical are the chain-

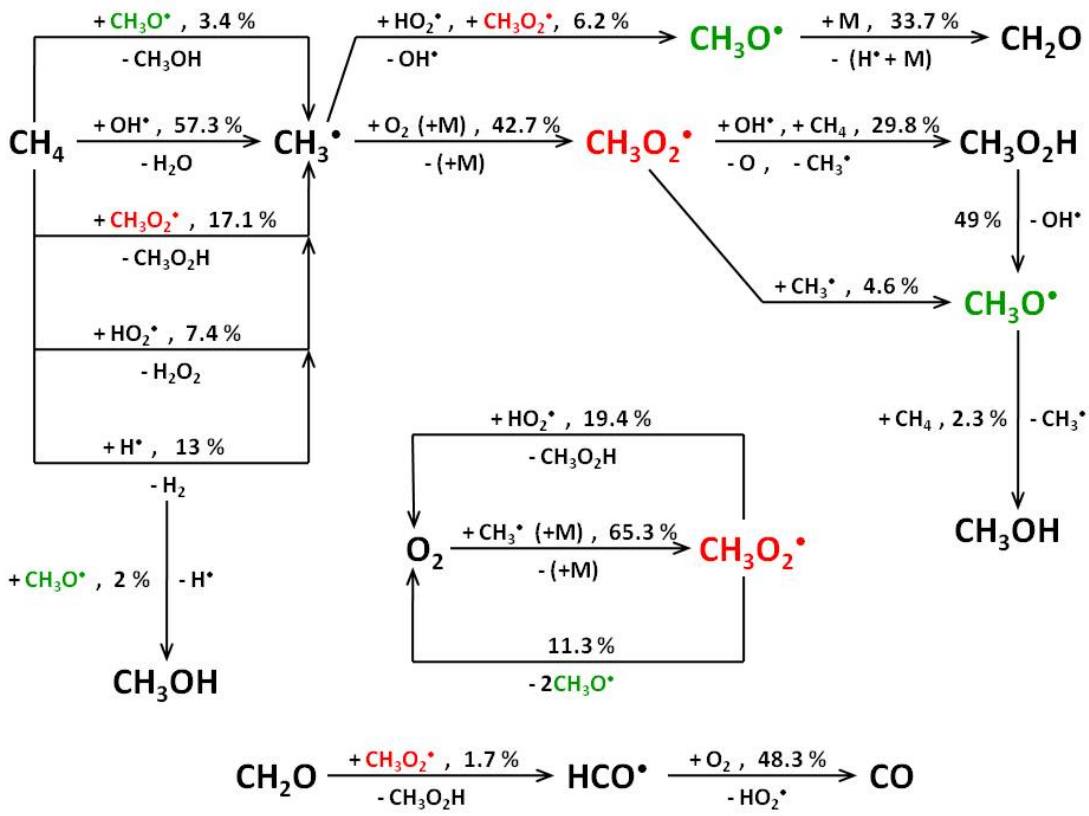

Figure 5.16: Main reaction pathways for the mechanism of Dooley et al. at C/O=2, 4 bar, 2000 mln · min^{-1}, 500 °C conditions at the axial position of 19 mm.

propagation step,

$$H^{\bullet} + O_2(+M) = HO_2^{\bullet} \tag{5.12}$$

and via formyl radicals shown in the network. Reactions of the hydroperoxy radical with methylperoxy radical, shown above, and the coupling to hydrogen peroxide, $2HO_2^{\bullet} = H_2O_2 + O_2$, in essence are the dominant reactions for quenching of hydroperoxy radicals (in combination constitute 46.4% of hydroperoxy radicals conversion). Another minor route of this radical quenching is a reaction with methane and methyl radicals (combined 11.7%).

RPA of species at position 50 mm is shown in Figure 5.17. At this position too, CH_4 is also mostly consumed by reaction with OH radicals, and the latter are produced in largest by thermal decomposition of H_2O_2 upon collision with a

third body M (the only reaction of hydrogen peroxide conversion) as the secondary initiation step. The largest share of hydrogen peroxide, on its turn, is generated through a branching step:

$$CH_4 + HO_2^{\bullet} = CH_3^{\bullet} + H_2O_2 \tag{5.13}$$

The largest part of water as the final product is also generated through the reaction of methane with hydroxyl radicals, upon which 40% of OH radicals are consumed. The majority of generated CH_3 radicals in the presence of a third body M (rate constant is in the pressure fall-off region) couple to ethane, which is subsequently destroyed by 4% of CH_3 radicals as the major ethane destruction channel. Thus, methyl radicals are both a source and consumer of ethane. Similarly to ethane, the formed ethylene (35.6%) is transformed back to methane by reaction with 2.5% of the primarily produced methyl radicals. This accounts to the largest ethylene consumption channel. Ethylene at this stage is formed through either unimolecular decomposition of oxygen-containing C_3-C_4 radicals, of propylene oxide, 1-propen-3-ol, butyl and ethylperoxyl radicals, ethylformate, or ethanol decomposition upon collision with a third body M, or by reaction of methylidine radicals:

$$CH^{\bullet\bullet\bullet} + CH_4 = C_2H_4 + H^{\bullet} \tag{5.14}$$

Surprisingly, but there is any no pathway of direct ethylene formation from ethane.

Reaction of the primary methyl radicals with the reactant molecular oxygen accounts to "loss" of only 3.2% of the former; here by loss one implies the amount of methyl radicals which do not couple to ethane.

$$CH_3^{\bullet} + O_2 = CH_2O + OH^{\bullet} \tag{5.15}$$

Unlike at position 19 mm, there are no methylperoxy radicals formed. Mims et al. [5] pointed out that methyl radicals are relatively unreactive with O_2, unlike, for example, vinyl radicals which are known to react very quickly with O_2(g) to form CO_x precursors. The initial $CH_3 - O_2$ adduct is said to be unstable and fall back to methyl and O_2(g).

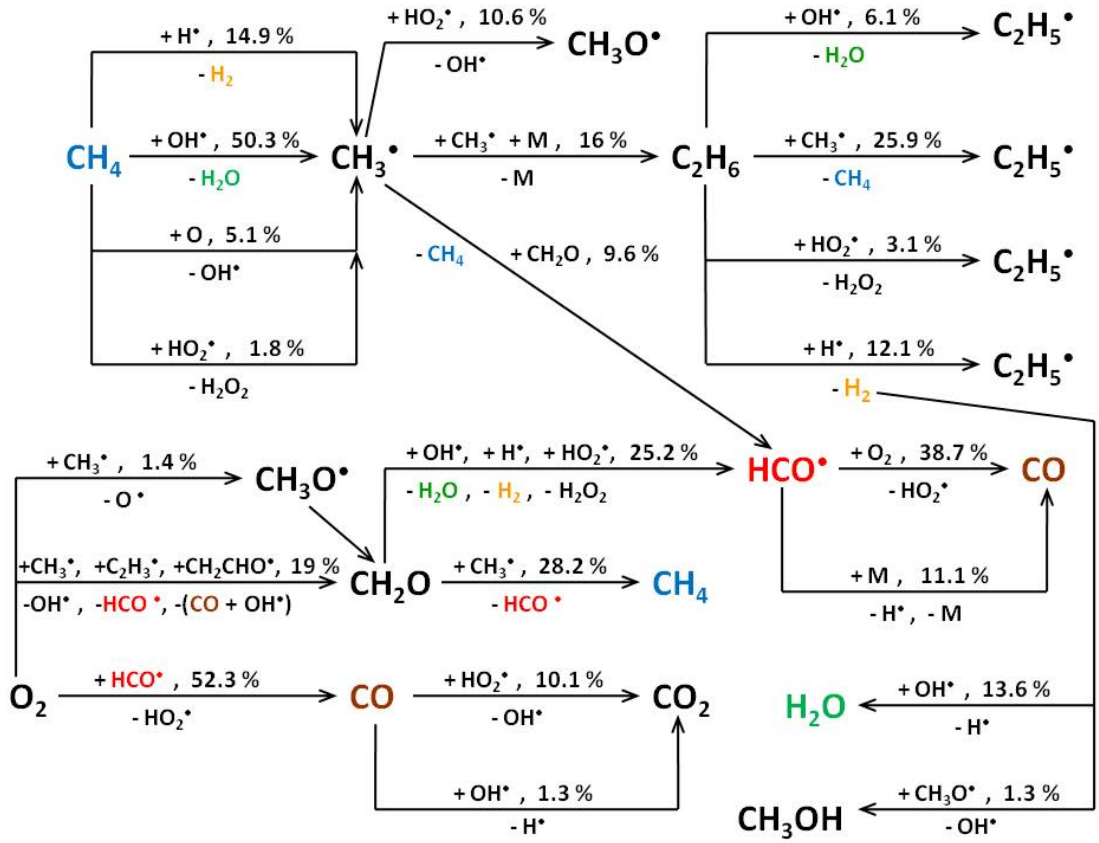

Figure 5.17: Main reaction pathways for the mechanism of Dooley et al. at C/O=2, 4 bar, 2000 mln · min^{-1}, 500 °C conditions at the axial position of 50 mm.

Formaldehyde was reported to be one of the major precursors of carbon monoxide in fuel-rich methane oxidation [43; 136]. The RPA shown also corroborates the thesis that formaldehyde is the carbon monoxide precursor, since more than half of it is converted to CO through formyl radical, HCO, which, in turn, converts the majority of the initial reactant oxygen. Whereas one of the largest routes to CO is indirect through formaldehyde, the other largest but direct route to CO, as well as to formaldehyde, formation is through oxidation of vinoxy radical:

$$CH_2CHO^{\bullet} + O_2 = CH_2O + CO + OH^{\bullet} \tag{5.16}$$

So, there are only two significant reaction channels to carbon monoxide at this position. As was mentioned above, the oxidation reaction of HCO radicals to CO

and HO_2 represent the main formation pathway for the HO_2 radical.

At this axial position of 50 mm in Fig. 5.17, which can be said to lie in the radical-rich region, CH_3O radical is formed from methyl and either hydroperoxyl radicals or molecular oxygen. CH_3O radical is the only precursor of methanol (the path to methanol through hydrogen destruction is shown in the network). Only about 6% of this radical is transformed to methanol, whereas the major share – one-third of it – ends up as formaldehyde due to its thermal instability:

$$CH_3O^{\bullet} + M = CH_2O + H^{\bullet} + M \tag{5.17}$$

Fig. 5.18(c) demonstrates simulated profiles of the methoxy radical. In general, this sub-figure clearly explains non-closure of carbon balance (up to maximum of 10%) given in Fig. 5.18(b) due to formation of formaldehyde and methanol, also discussed above for the case of mass-spectrometric measurements.

Oxidation of CO almost exclusively by OH radicals to form CO_2 was reported by some authors in the area of stoichiometric methane combustion [51; 137; 138]. From our RPA at this axial position, such exclusive role of OH radicals is diminished by hydroperoxyl radicals which actually contribute largest to CO oxidation. These authors stated that the oxidation rate of CO by OH radicals has little effect on ignition-delay time (because of the late proceeding of this step during combustion), but nevertheless very important for determining the rate of flame propagation; in fact, variation of its rate coefficient was said to strongly influence the flame propagation. Interestingly, but in the RPA there is no reaction of direct CO oxidation by atomic oxygen:

$$CO + O(+M) = CO_2(+M) \tag{5.18}$$

which indicates that either pressure or temperature are not sufficient for this reaction to occur.

RPA at the end of the free gas phase, shown in Figure 5.19, indicates methane activation mostly by atomic hydrogen. Percentages of the generated methyl radicals, coupling to ethane, with subsequent destruction of the formed ethane by atomic hydrogen simultaneously almost double compared to the RPA at position

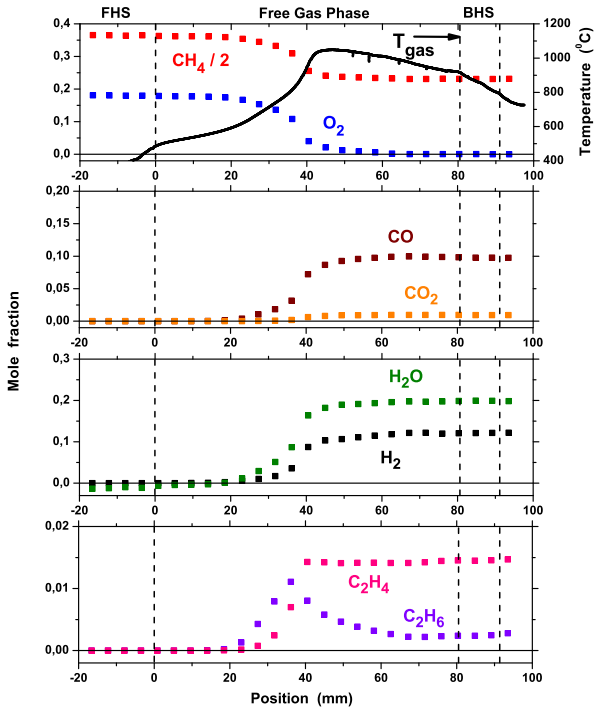

(a)

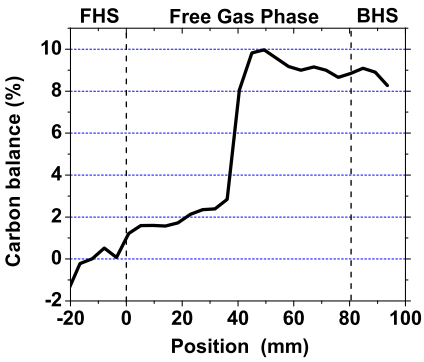

(b)

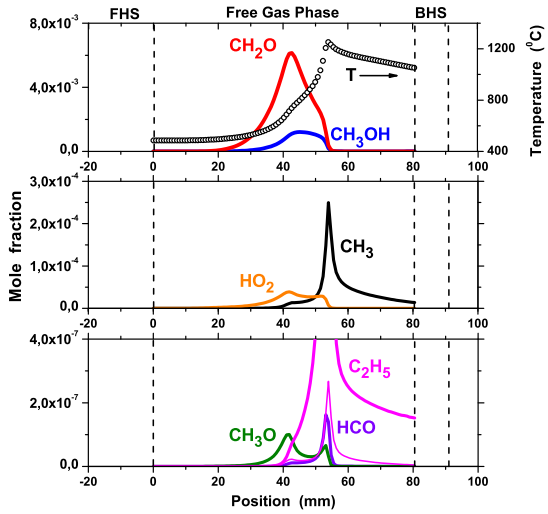

(c)

Figure 5.18: (a) Experimental profiles; (b) Carbon balance, and (c) Simulated temperature and radical mole fractions at C/O=2, 4 bar, 2000 mln·min^{-1}, 500 °C conditions. Simulation with Dooley et al. model.

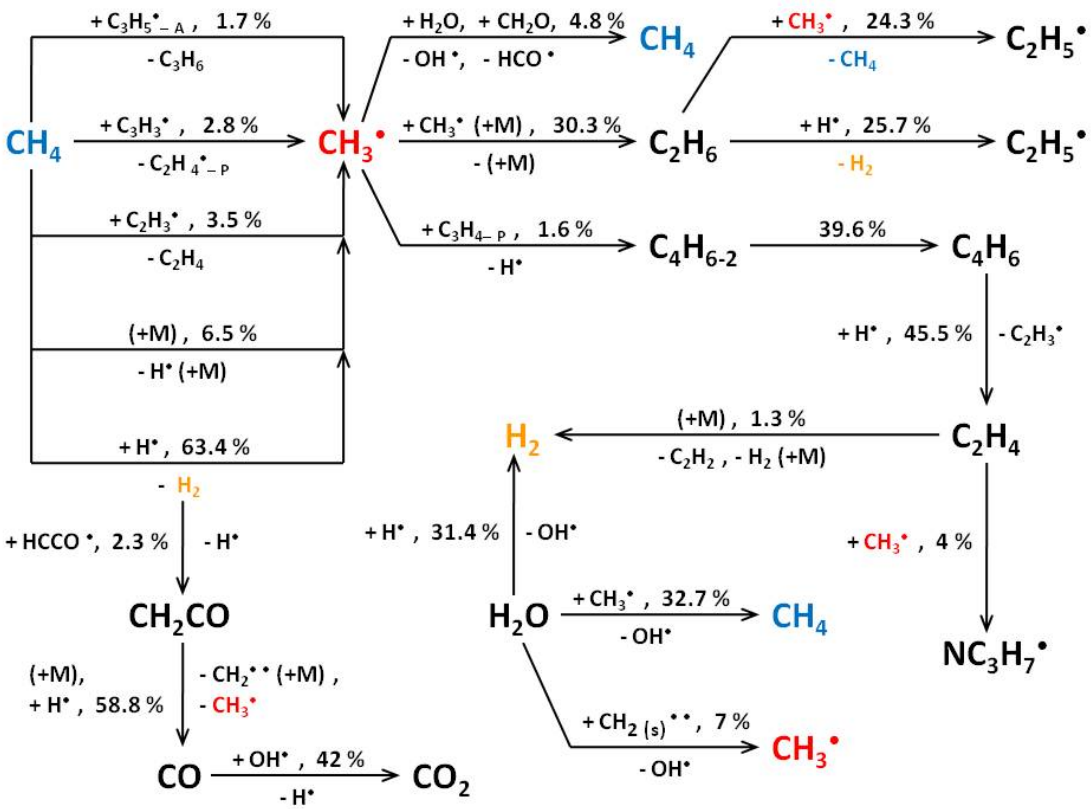

Figure 5.19: Main reaction pathways for the mechanism of Dooley et al. at C/O=2, 4 bar, 2000 mln $\cdot$ min^{-1}, 500 °C conditions at the axial position of 80.5 mm.

50 mm. At the same time, percentage of methyl radicals interacting with ethane remains more or less similar to that at position 50 mm, viz. 6.6% (percentages of methyl radicals reacting with ethane are not shown in RPA).

By far the dominant share of HCCO radicals, which are involved in the hydrogen destruction channel (the only hydrogen destruction channel) to ketene, arises from reaction of the reactant oxygen (57.6% of it) with acetylene:

$$C_2H_2 + O_2 = HCCO^{\bullet} + OH^{\bullet} \tag{5.19}$$

The latter reaction was thoroughly investigated and confirmed by several authors [139; 140; 141]. Subsequently, around 50% of HCCO radicals are converted to CH_2CO which open up one of the two main carbon monoxide formation chan-

nels shown in the network. The other channel to CO, not shown here, is from HCO radical derived from oxygen reaction with C_2H_3 and C_3H_3 radicals:

$$C_2H_3^\bullet + O_2 = HCO^\bullet + CH_2O \tag{5.20}$$

$$C_3H_3^\bullet + O_2 = HCO^\bullet + CH_2CO \tag{5.21}$$

These two channels share around 10% of oxygen conversion reactions. Even less percentage of oxygen conversion reactions goes to the remaining route, which is a reaction with methane: $CH_4 + O_2 = CH_3^\bullet + HO_2^\bullet$.

All the carbene species (CH_2 and CH_2(s)) from ketene, CH_2CO, eventually transform to methyl radicals (directly or via surface carbene species) via reactions with terminal stable species H_2, CH_4 and H_2O, constituting major secondary methyl radical formation channels.

Reactions of ethylene generation are mostly the same as those at position 50 mm in Fig. 5.17; one of the formation steps through C_4H_6 species is shown in the network. In analogy with ethane, the main destruction path of ethylene is via reaction with methyl radicals leading to formation of ethenyl radicals and methane. Unlike in RPA at position of 50 mm, ethanol decomposition upon collision with a third body here does not generate ethylene, but methyl and hydroxymethyl radicals:

$$C_2H_5OH + M = CH_2OH^\bullet + CH_3^\bullet + M \tag{5.22}$$

Reactions of the water molecules are shown separately in the network. As is seen, for example, more than half of H_2O transforms to hydrogen and methane. In the reaction path analyses for all 4 positions, in agreement with experimental results, the quantities of C_3 hydrocarbons are very limited, not because they are oxidised very fast, but because there are no significant reaction paths to them.

In the following paragraphs, similar reaction path analysis for other selected microkinetic models used in this thesis are described, in order to reveal main discrepancies and similarities with the model of Dooley et al.

The basis of the mechanism of Lopez et al. is the previously reported mechanism of Rasmussen et al. [47] for which the authors did RPA and found that the

main methane activation pathway is through reaction with OH radicals,

$$CH_4 + OH^\bullet = CH_3^\bullet + H_2O, \tag{5.23}$$

regardless of methane-to-oxygen stoichiometry. RPA for the mechanism of Lopez et al. was also done in this thesis for simulated profiles at different axial distances. It was found that this reaction of methane activation with OH radicals is pertinent when oxygen is available in the system. Shortly after reaching the point of complete oxygen conversion, the main methane activation pathway is through atomic hydrogen,

$$CH_4 + H^\bullet = CH_3^\bullet + H_2, \tag{5.24}$$

and at the end of the free gas phase (much after reaching the point of complete oxygen conversion), the main methane activation step is via the reactions with ethenyl and ethyl radicals:

$$CH_4 + C_2H_3^\bullet = CH_3^\bullet + C_2H_4 \tag{5.25}$$

$$CH_4 + C_2H_5^\bullet = CH_3^\bullet + C_2H_6 \tag{5.26}$$

It should be noted that these shown reaction pathways for the Dooley et al. model are conserved qualitatively regardless of which of the 5 experimental conditions are considered, and quantitatively they differ.

Figures 5.21 and 5.20 show a RPA focused on the reactions of methane and ethane for the models of Lopez et al. and Mims et al. at two selected axial positions: that corresponding to the maximum of ethane generation, and at the end of the free gas phase. Analysing these reaction paths, together with RPA for Dooley et al. model, one can convincingly conclude that in the presence of oxygen, various mechanisms show identical elementary reactions, i.e., they agree qualitatively, whereas absence of oxygen signifies varying pathways among the models. The gas-phase OCM mechanism of Chen et al. [66] is the basis of the gas-phase part of the mechanism of Sun et al. [9], and the latter showed poor prediction of the experimental data in this thesis as shown above. Couwenberg [56] performed RPA for the mechanism of Chen et al. [66] at 100 and 400 kPa and noted exactly the same reactions – i.e., for example, methane activation by OH,

H, and HO_2 radicals, and ethane destruction by CH_3, H, and OH radicals – as are observed from the RPA in this thesis. Also Tjatjopoulos and Vasalos [70], who did RPA for Zanthoff and Baerns model [7], observed the same qualitative picture with radicals reacting with methane and C_2 products. In other words, even a mechanism poorly describing the experimental data qualitatively agrees with the best describing mechanisms. The steps which are present in one mechanism and absent in another (e.g., C_2H_6 reaction with $HO_2^{\bullet}$), do not have significant numerical contribution.

The widely accepted paradigm in the area of catalytic OCM is that OCM is a gas-phase reaction catalysed by a solid catalyst. According to this paradigm, an ideal catalyst should produce methyl radicals to a maximal extent, so that they can desorb from the surface and couple to ethane in the gas phase [58; 59]. From RPA done for several models in this thesis it is seen that destruction of the formed ethane by methyl radicals in the gas phase does not favour the concept of maximal methyl radicals generation into the gas phase, but rather an ideal catalyst should serve as a platform on which methyl radicals diffuse across the catalyst surface and combine to ethane, with ethane desorbing into gas phase before reaction with methyl radicals on the surface. Even more favourable case is when ethane is dehydrogenated to ethylene on the surface; in any case, the rate of C_2 hydrocarbons desorption from an ideal catalyst's surface is very high.

To have an additional insight into models apart from RPA, the relative sensitivity analysis was done for the models of Dooley et al. and Lopez et al. The sensitivity analysis was possible only with plug-flow reactor model. Comparison of experimental and plug-flow-simulated results for the models of Dooley et al. and Lopez et al. are shown in Fig. 5.22(a) and 5.22(b), respectively. In contrast to boundary-layer simulations, in this approach the experimental temperature profile was used as the input. Corresponding profiles of the normalised first-order sensitivity coefficients for the most sensitive reactions with respect to ethylene are given in Fig. 5.22(c) and Fig. 5.22(d). As is seen from the axial positions corresponding to highest rates of ethylene production in both models, reactions scavenging methylperoxyl and formyl radicals favour ethylene formation. Less sensitivity is to reactions scavenging methyl and hydroperoxyl radicals; this result can be linked to RPA for ethane destruction in that methyl and hydroperoxyl

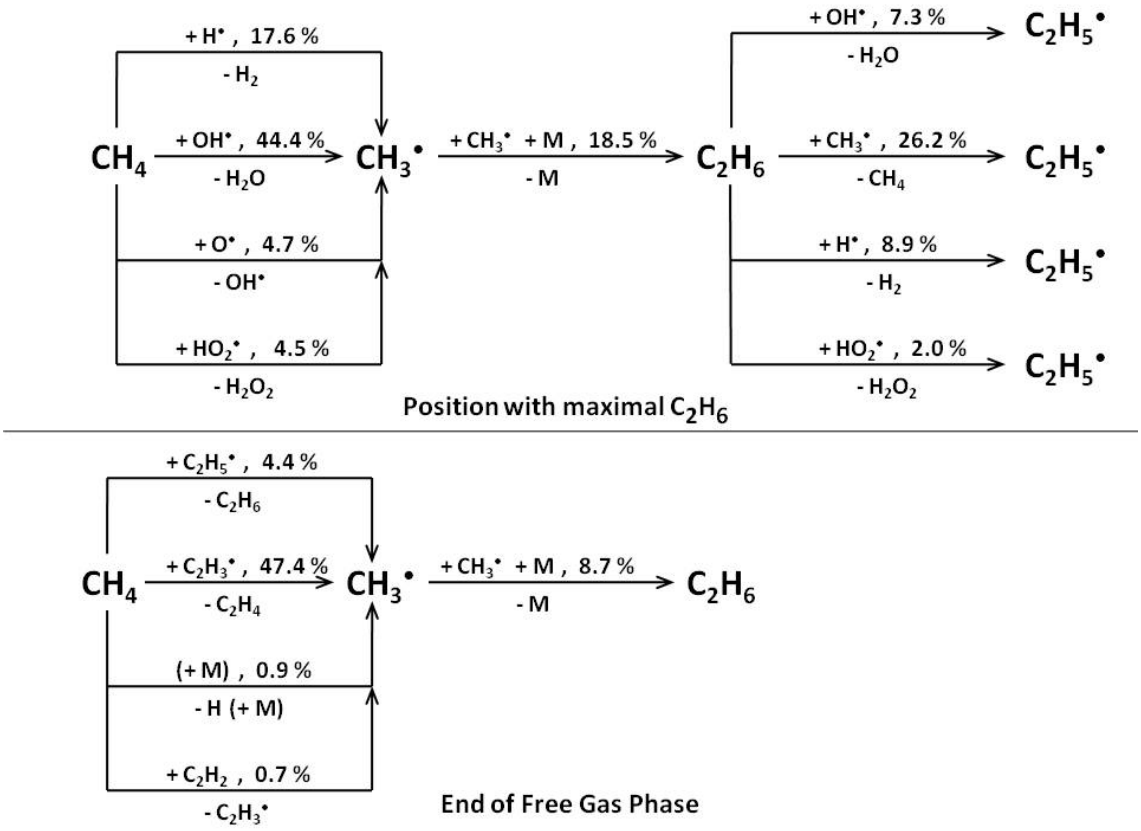

Figure 5.20: Selected main reaction pathways for the model of Lopez et al. at C/O=2, 4 bar, 2000 mln $\cdot$ min^{-1}, 500 °C conditions at the axial position of maximal C_2H_6 mole fraction (upper scheme) and at the end of free gas phase (lower scheme).

radicals, which degrade ethane to ethyl radicals, also degrade ethylene to ethenyl radicals. Overall, because of the radical-poor situation the rate-limiting reactions tend to be chain-branching and chain-terminating ones, as is discussed in Chapter 2.

Without calculation of laminar velocities of the reacton front propagation it can be inferred that the flame velocity with Lopez et al. model calculations should be higher than with Dooley et al. model calculations, owing to the more stretched zone of most sensitive radical reactions in Lopez et al. model. Higher velocities of reaction front propagation foster more intensive diffusive transport of radicals before the main reaction zone, and such diffusive transport makes the chain ini-

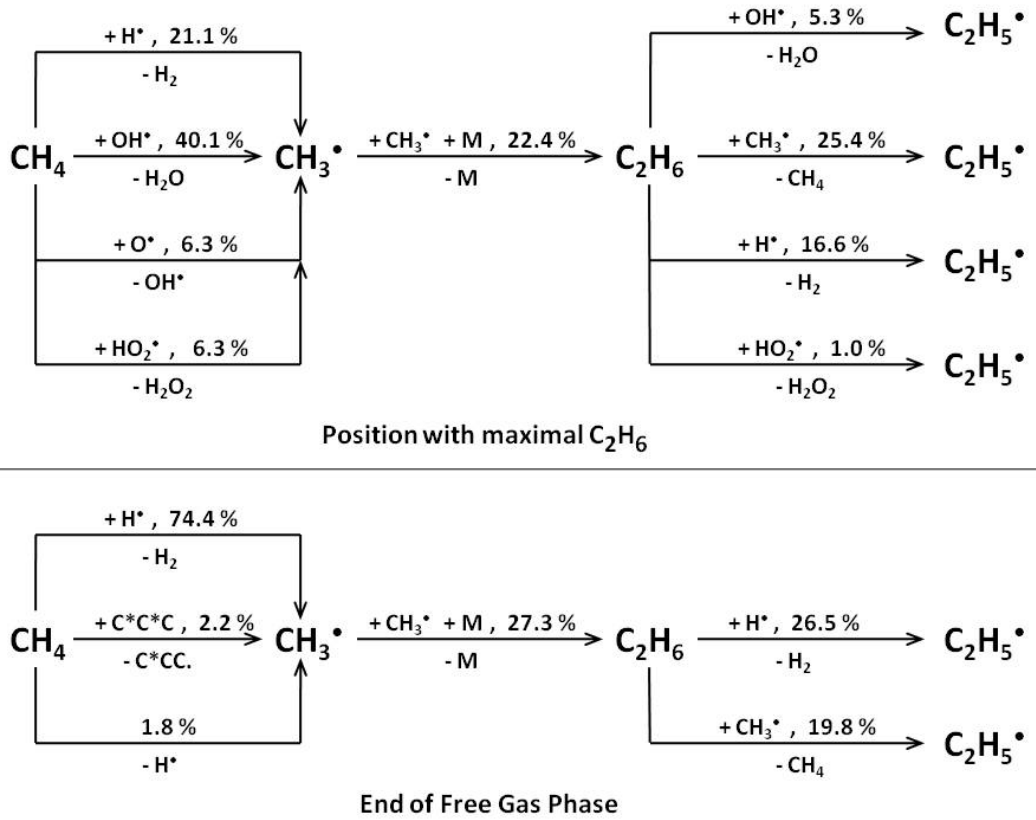

Figure 5.21: Selected main reaction pathways for the model of Mims et al. at C/O=2, 4 bar, 2000 mln · min^{-1}, 500 °C conditions at the axial position of maximal C_2H_6 mole fraction (upper scheme) and at the end of free gas phase (lower scheme).

tiation irrelevant, with radical-radical reactions becoming more important than during ignition. Table 5.2 shows the rate constants for the most sensitive reactions with respect to ethylene formation/consumption from Figure 5.22 in both the models calculated at 1064 K (corresponding to axial position of 35 mm). The first four reactions with positive sensitivity coefficients (favouring ethylene formation) in Lopez et al. model have similar rate constants as in Dooley et al. model. However, the rate constants with negative sensitivity coefficients (favouring ethylene destruction) in Dooley et al. model are appreciably higher than in Lopez et al. model – for instance the rate constant of the reaction of hydroperoxyl radicals coupling to hydrogen peroxide is three orders of magnitude higher. Simulation

with Lopez et al. model with the Arhhenius parameters of this reaction taken from Dooley et al. mechanism is shown in Figure 5.23. Since this reaction favours ethylene destruction, the higher rate constant of it results in better agreement of the modelled and experimental ethylene curves. However, prediction for the other species gets worse dut to more intensive chemistry caused by the increased rate of hydrogen peroxide formation (rate constant of 1.08E+14 $m^3 \cdot mol^{-1} \cdot s^{-1}$ versus 2.22E+11 in the original mechanism), and the latter is the precursor of hydroxyl radical, a very strong chain initiator:

$$H_2O_2(+M) = OH^\bullet + OH^\bullet(+M) \tag{5.27}$$

Thus, a way of improvement of a microkinetic model and its agreement with other models lies in the verification and ascertaining (by theory or experimental methods) of the rate constant parameters of certain elementary reactions, especially of those reactions which show too varying rate constant parameters from one mechanism to another.

Table 5.2: Rate constants and sensitivity coefficients for selected bimolecular reactions most sensitive with respect to C_2H_4 species derived from plug-flow model calculations with Dooley et al. and Lopez et al. models.

No.	Elementary reaction	Rate constant k at 1064.15 K		Sensitivity coefficient	
		Dooley et al.	Lopez et al.	Dooley et al.	Lopez et al.
(1)	$CH_3 + HO_2 = CH_3O + OH$	8.27E+12	1.77E+13	0.79	0.43
(2)	$CH_3O_2 + CH_3 = CH_3O + CH_3O$	6.8E+12	5.98E+12	0.51	0.16
(3)	$H + O_2 = O + OH$	3.35E+13	3.39E+13	0.31	0.21
(4)	$CH_4 + HO_2 = CH_3 + H_2O_2$	0.22E+11	1.61E+11	0.2	0.15
(5)	$HO_2 + HO_2 = H_2O_2 + O_2$	1.08E+14	2.22E+11	-0.31	-0.09
(6)	$CH_3 + HO_2 = CH_4 + O_2$	3.16E+12	8.2E+11	-1.3	-0.88

Plug-flow-reactor simulations for the C/O ratio of 2 at 4 bar in Figure 5.22(a) and 5.22(b) show a much better agreement with experimental data than corresponding boundary-layer simulations. However, such a good agreement is of

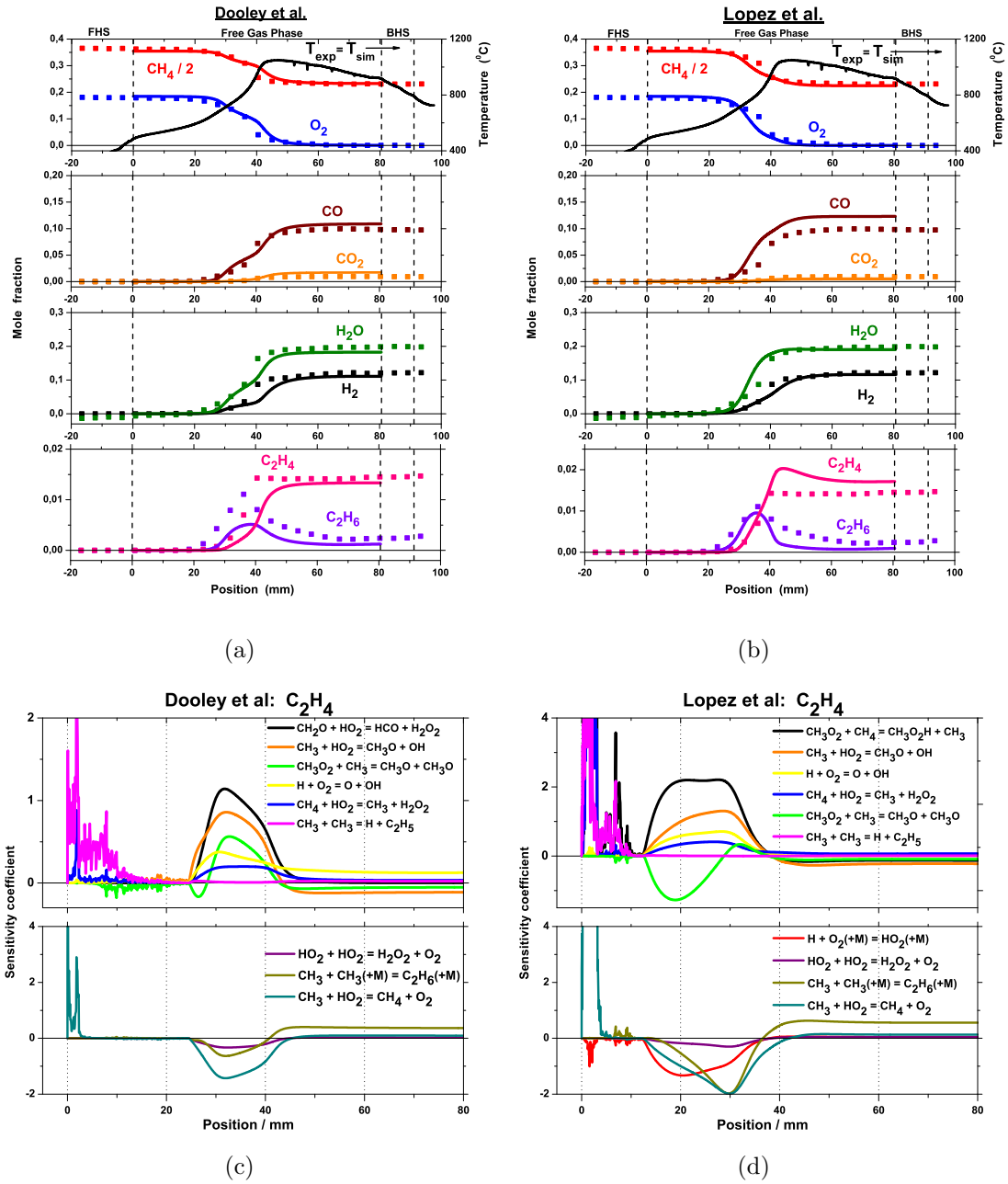

Figure 5.22: Comparison of the experimental profiles with simulated species and sensitivity coefficients profiles. Simulation with the plug-flow reactor model at C/O=2, 4 bar, 2000 mln $\cdot$ min^{-1} and 500 °C conditions for (a) and (c) – Dooley et al. model; (b) and (d) – Lopez et al. model. Symbols – experimental data; lines – modeled data.

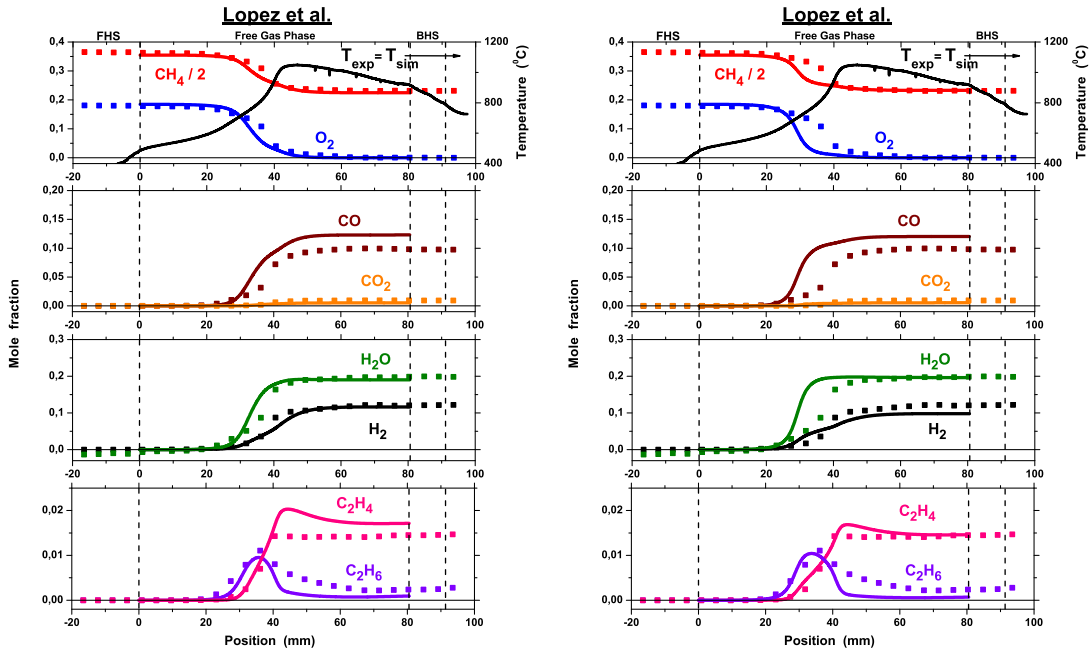

(a) (b)

Figure 5.23: Comparison of the experimental and simulated species profiles. Simulation with the plug-flow reactor model at C/O=2, 4 bar, 2000 mln $\cdot$ min^{-1} and 500 °C conditions with (a) Original Lopez et al. [2] model; (b) Lopez et al. model with the Arrhenius parameters for the reaction $HO_2 + HO_2 = H_2O_2 + O_2$ taken from Dooley et al. [1] mechanism (rate constant k = 1.08E+14 m$^3 \cdot$ mol$^{-1} \cdot$ s^{-1}).

coincidence, since plug-flow simulated profiles in Figure 5.24 for C/O ratio of 4 at 8 bar still suffer from rapid reactants conversion peculiar for plug-flow reactor model. In this regard, good agreement of plug-flow-model simulations with experiments at lower pressures can be misleading.

The sensitivity coefficient towards some of the products in Dooley et al. and Lopez et al. models at the end of the free gas phase (position of 80.5 mm) are calculated and plotted in Figures 5.25 and 5.26. This particular position (80.5 mm) for sensitivity analyses was chosen because at it the differences between the models are clearly pronounced. From sensitivity analyses at this axial position it is seen that ethane and ethylene formation/destruction are sensitive to almost the same elementary reactions in both models. Particular noteworthy is the reaction of ethylene destruction by methyl radicals which is observed not to be sensitive

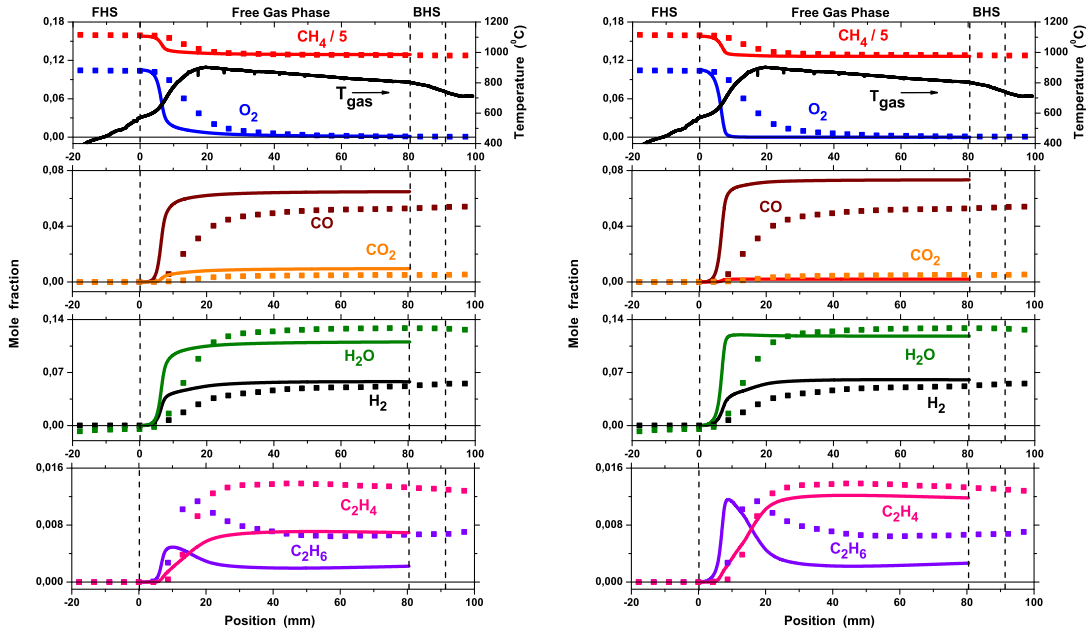

(a) (b)

Figure 5.24: Comparison of the experimental and plug-flow simulated profiles at C/O=4, 8 bar, 2000 mln $\cdot$ min^{-1} and 750 °C conditions for (a) Dooley et al. model; (b) Lopez et al. model. Symbols – experimental data; lines – modeled data.

to in the oxidation zone.

Lastly, considering good prediction of the experimental data by Dooley et al. model, a series of simulations using this model was performed in order to determine the operation "window" for gas-phase OCM, i.e., identify reaction conditions at which the output of the target C_2 hydrocarbons is maximal. As the output parameter, the combined selectivity of ethane and ethylene was selected. Figures 5.27 and 5.28 show the contour plots for reactants conversions, combined ethane and ethylene selectivities and their combined yields on methane conversion basis as a function of carbon-to-oxygen equivalence ratio, total reactor pressure and temperature. The temperatures in the abscissa correspond to gas temperature inside the reactor when oven temperature was kept constant at 750 °C for all simulations.

In particular, Figure 5.27 shows that the maximal combined C_2 hydrocarbons

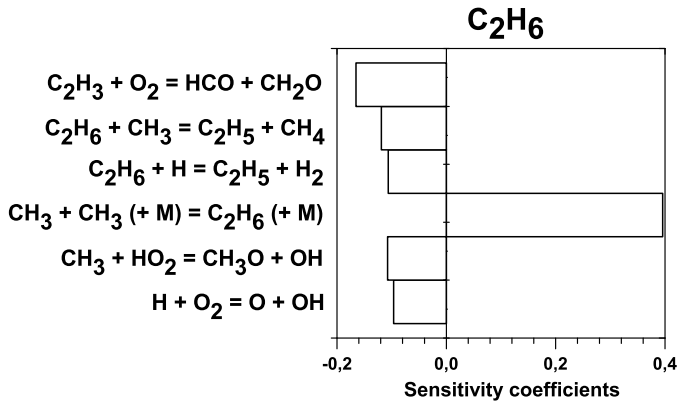

(a)

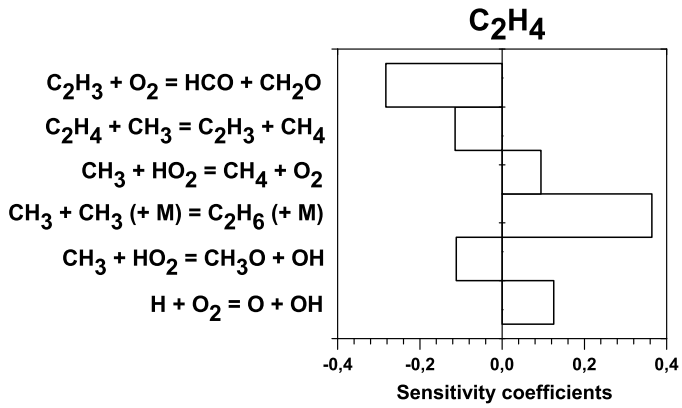

(b)

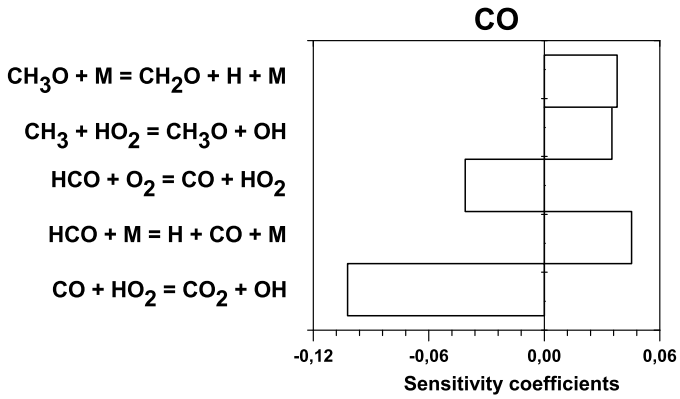

(c)

Figure 5.25: First-order sensitivity coefficients for the most important elementary reactions with respect to formation of (a) C_2H_6, (b) C_2H_4 and (c) CO from sensitivity analysis done for C/O=2, 4 bar, 2000 mln·min^{-1} and 500 °C conditions for the model of Dooley et al. [1].

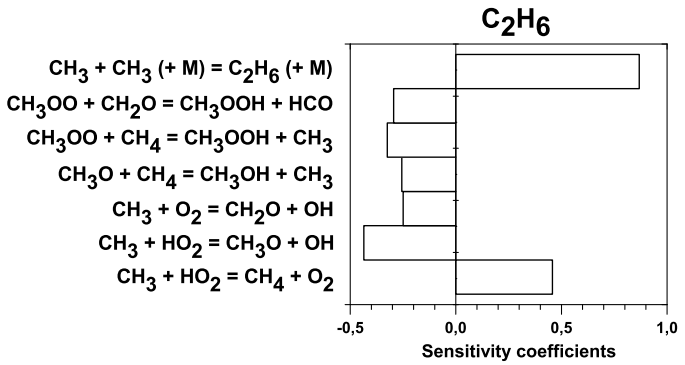

(a)

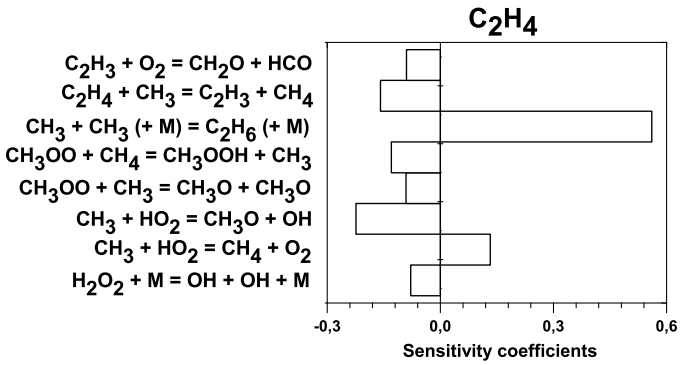

(b)

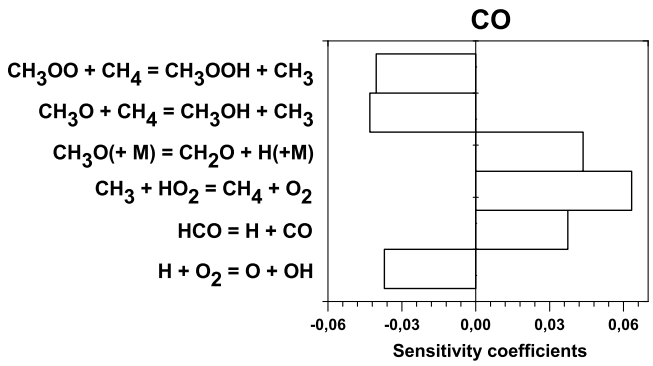

(c)

Figure 5.26: First-order sensitivity coefficients for the most important elementary reactions with respect to formation of (a) C_2H_6, (b) C_2H_4 and (c) CO from sensitivity analysis done for C/O=2, 4 bar, 2000 mln·min^{-1} and 500 °C conditions for the model of Lopez et al. [2].

selectivity at the C/O ratio of 2 is achieved at middle ranges of methane conversion (ca. 29% conversion in the plot) and at maximal oxygen conversion levels. Similarly, Figure 5.28 shows that at C/O ratio of 8, the maximal C_2 hydrocarbons selectivity coincides with the maximal O_2 conversion. From analysis of these two C/O ratios, it can be said that for a technical process the gas-phase OCM at C/O ratio of 8 is more appropriate, because the C_2 selectivity is higher than that at C/O = 2. Appropriateness for a technical process is valid if high selectivity is a target, because C_2 yield values in relation to methane conversion drop significantly when going to a higher C/O ratio. For example, at C/O ratio of 2 the yield drops 3.5 times when CH_4 conversion goes from middle range (highest C_2 selectivity) to maximal, whereas it correspondingly drops 6.3 times at C/O ratio of 8. The yield calculations are in agreement with experimentally observed space-time yield values in Figure 5.5 from which the C/O ratio of 8 is outside the technically feasible range of 1 – 10 $mol \cdot m^{-3} \cdot s^{-1}$ described by Weisz [133].

At the same time, the pressure window at which the maximal C_2 selectivity is obtained is wider (from 5 to 10 bar) at the C/O ratio of 8 at lower temperature values – from 975 K at C/O = 8 versus from 1100 K at C/O = 2. Overall, from these contour plots one can conclude that engineering concepts which globally increase oxygen concentration in the feed for high C_2 hydrocarbons yield, but locally decrease oxygen concentration (for high C_2 selectivity) along the axial profile in order to compensate for its rapid consumption as the limiting reactant are necessary. In case of catalytic OCM, one of such engineering concepts realising increased oxygen concentration locally along the reactor axial length is catalytic membrane reactors [142].

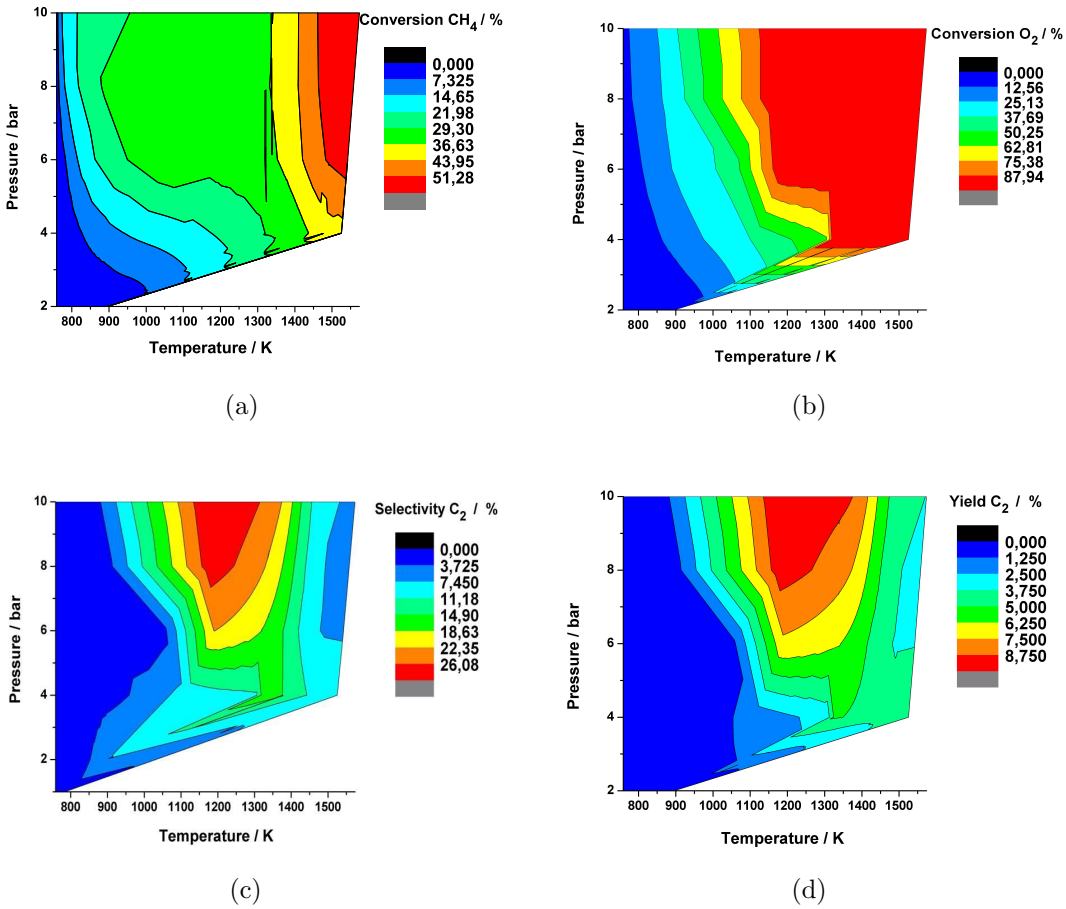

Figure 5.27: Contour plots of simulated (a) CH_4 conversion; (b) O_2 conversion; (c) combined C_2H_6 and C_2H_4 selectivities; (d) combined C_2H_6 and C_2H_4 yields as a function of pressure and temperature at C/O = 2, 2000 mln $\cdot$ min^{-1} and 750 °C oven temperature conditions. Simulation with Dooley et al. [1] model.

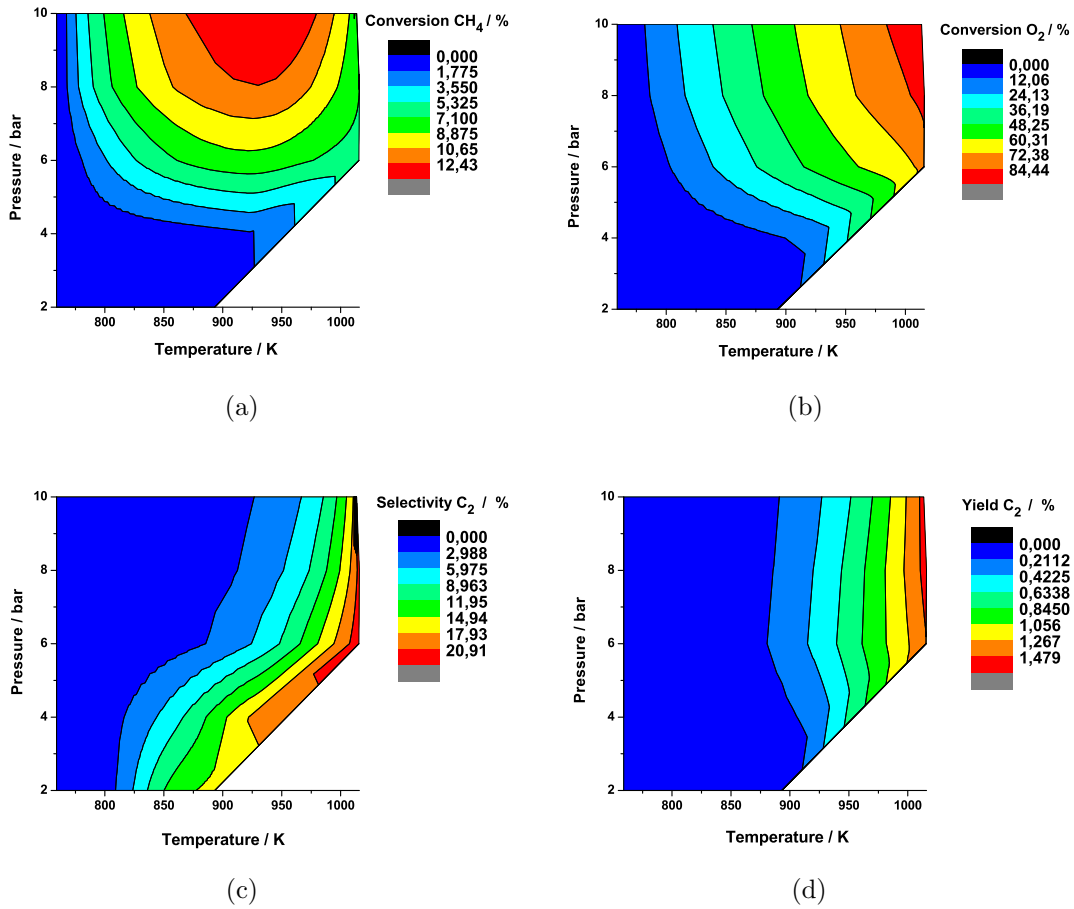

Figure 5.28: Contour plots of simulated (a) CH_4 conversion; (b) O_2 conversion; (c) combined C_2H_6 and C_2H_4 selectivities; (d) combined C_2H_6 and C_2H_4 yields as a function of pressure and temperature at C/O = 8, 2000 mln $\cdot$ min^{-1} and 750 °C oven temperature conditions. Simulation with Dooley et al. [1] model.

Chapter 6

General Conclusions

It is possible to obtain spatially resolved steady-state profiles of species and temperatures during gas-phase oxidative coupling of methane using the spatially resolved profile reactor at industrially relevant high-temperature, high-pressure conditions. Moreover, the experimental profiles of species and temperatures which can be obtained with this reactor configuration are appropriate data to validate a microkinetic model created for fast radical-chain reactions.

Boundaries for experimentation in terms of optimal pressures for the used reactor geometry are determined, viz., the gas-phase OCM reaction does not proceed at atmospheric pressure nor that too high pressures as 20 bar at certain methane-to-oxygen equivalence ratios are not suitable for kinetic investigations and do not comply with reactor safety conventions owing to the shift of the reaction front out of the designed reaction zone towards the reactor entrance. Concerning constructive peculiarities for the spatial profile reactor operation, a diameter of the sampling orifice of 100 μm is optimal for such types of gas phase experimentation when the aim is to obtain more precise gas-phase temperature profile measurements.

Prevailing reaction products are water, carbon monoxide and hydrogen, in descending order of molar fractions. Selectivities to the target ethane and ethylene, along with selectivity to carbon dioxide, are generally very low. Ethane is the primary product of methane coupling, and depending on conditions is overtaken by later-generated ethylene.

Ten microkinetic models from literature are chosen and validated against the

obtained experimental profiles of species and temperatures. These models are based on elementary reactions and provide fundamental insights into the reaction mechanism. Comparison of the experimental data with the microkinetic modeling results showed that all of them in almost all considered cases except at lowest carbon-to-oxygen stoichiometry of 2 qualitatively predict the output of species correctly, but none of the models is able to predict the experimental species profiles quantitatively correctly for all the species simultaneously. Also it was shown that almost all the models underpredict the concentration of ethane out of the two target hydrocarbons. Overall, the microkinetic model of Dooley et al. showed best quantitative agreement with experimental results. The models developed for high-temperature stoichiometric methane combustion demonstrate the most unsatisfactory qualitative and quantitative performance. The procedure of reduction of large microkinetic mechanisms based on sensitivity analysis without alteration of their performance can be successfully realised using the Reaction Mechanism Generator software.

Comparison of the microkinetic models based on the cylindrical shear-flow reactor model showed that through this reactor model the ignition-delay time is not reproduced correctly, at least at lower pressures, whereas better reproduction is achieved with the plug-flow reactor model. On account of this, for correct reproduction of ignition-delay times it is recommended to apply full Navier-Stokes equations for modeling.

Detailed analysis of the microkinetic models via quantitative reaction path analysis for the major reaction pathways at various reactor axial positions shows that the first step in methane activation is by molecular oxygen with formation of methyl and hydroperoxyl radicals. Also the tested microkinetic models agree on most reactions when oxygen is present in the system (e.g., reactions of methane activation), whereas in the absence of oxygen, most of them differ substantially. One of the intrinsic limitations to high yields of the target ethane and ethylene is found to be owing to destruction of these formed hydrocarbons by desirable primary methyl radicals. Out of reaction path analysis results, a functioning of a hypothetically ideal catalyst which is not only an active methyl radicals generator into the gas, but also as a platform on which methyl radicals diffuse across the catalyst surface and combine before desorption is proposed.

The operation "window" for technical feasibility of gas-phase OCM shows that higher methane-to-oxygen ratios, higher pressures, and temperatures above 950 K are desirable for higher selectivities at low methane conversion and low combined yield of ethane and ethylene. Novel engineering concepts which globally increase oxygen concentration in the feed in order to compensate for its rapid consumption as the limiting reactant are necessary.

Appendix A Calibration of Analytical Instruments

Calibration of the mass spectrometer (MS) and micro gas chromatograph (GC) was done using either pure Ar or 8 vol.% He in Ar mixture as the internal standard. Figures 1 – 4 and Figures 5 – 8 show the species calibration curves for MS and GC, respectively, with curve parameters indicated within the graphs. The slope of each calibration curve for i^{th} species was taken as the response factor r_i for calculation of the molar flow rate (see Experimental Methodology section). Volumetric flow rates were measured with an electronic soap film-flow-meter from Horiba Corp, and each measuremenent point was the average of minimum 5 runs.

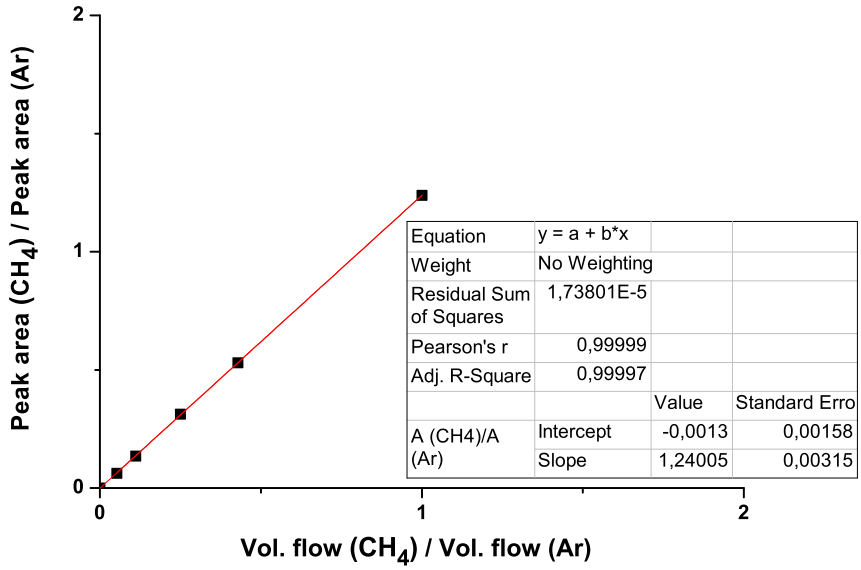

(a)

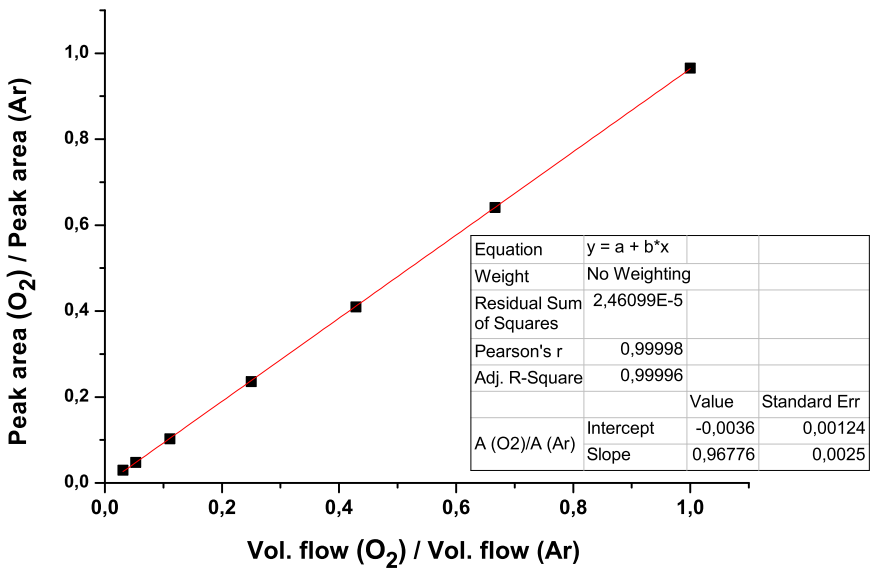

(b)

Figure 1: MS calibration curves with plot parameters of (a) CH_4; (b) O_2. Part I.

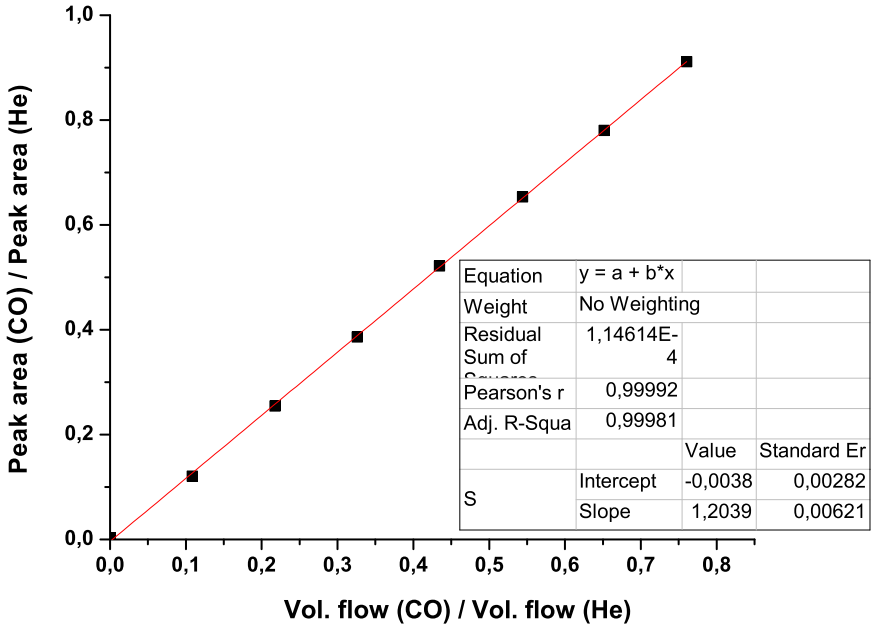

(a)

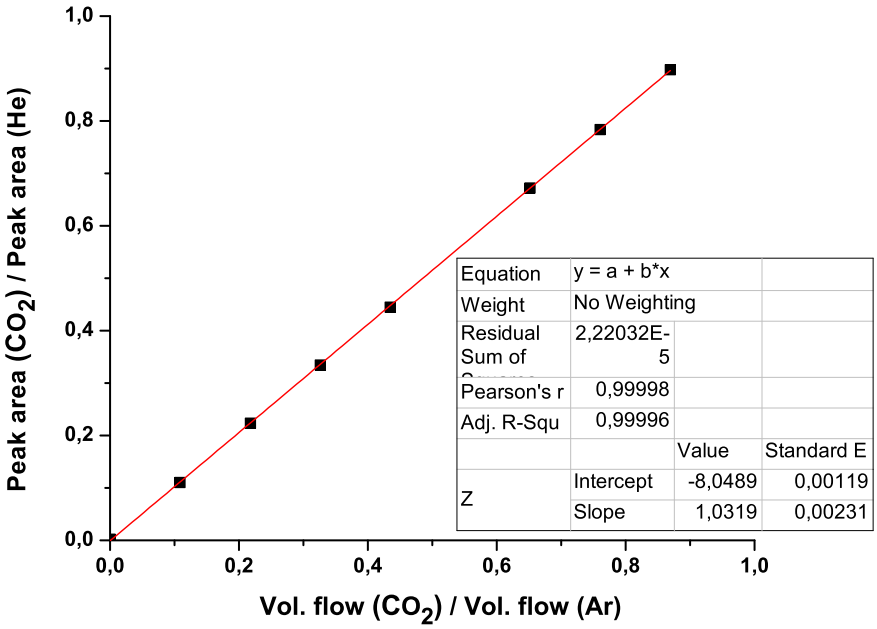

(b)

Figure 2: MS calibration curves with plot parameters of (a) CO; (b) CO_2. Part II.

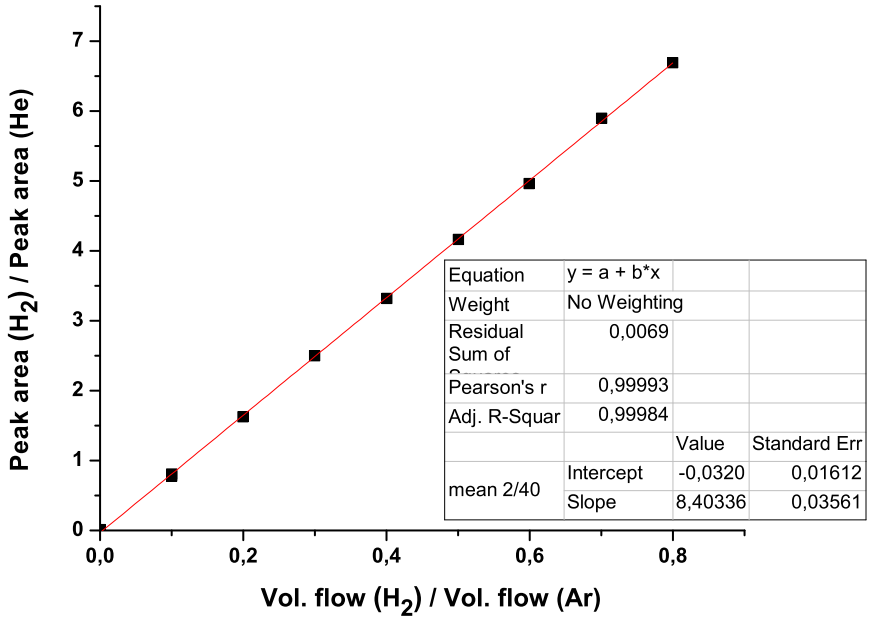

(a)

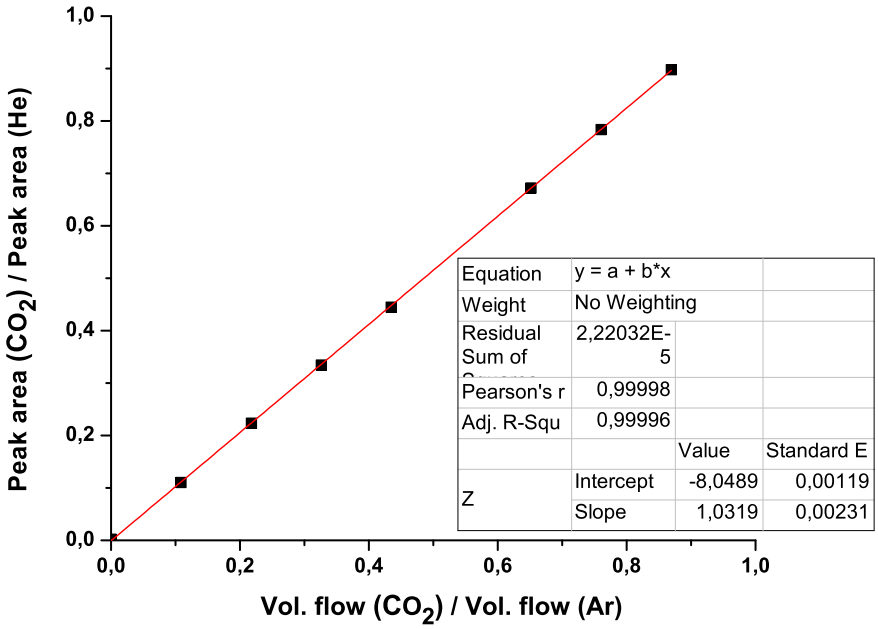

(b)

Figure 3: MS calibration curves with plot parameters of (a) H_2; (b) C_2H_6. Part III.

MSC2H4calibr2.jpg

Figure 4: MS calibration curve with plot parameters of C_2H_4. Part IV.

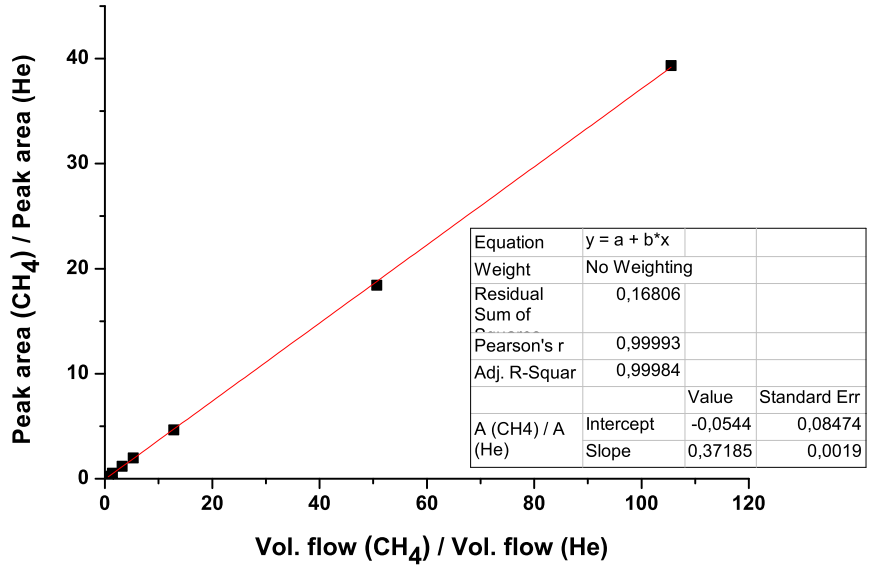

(a)

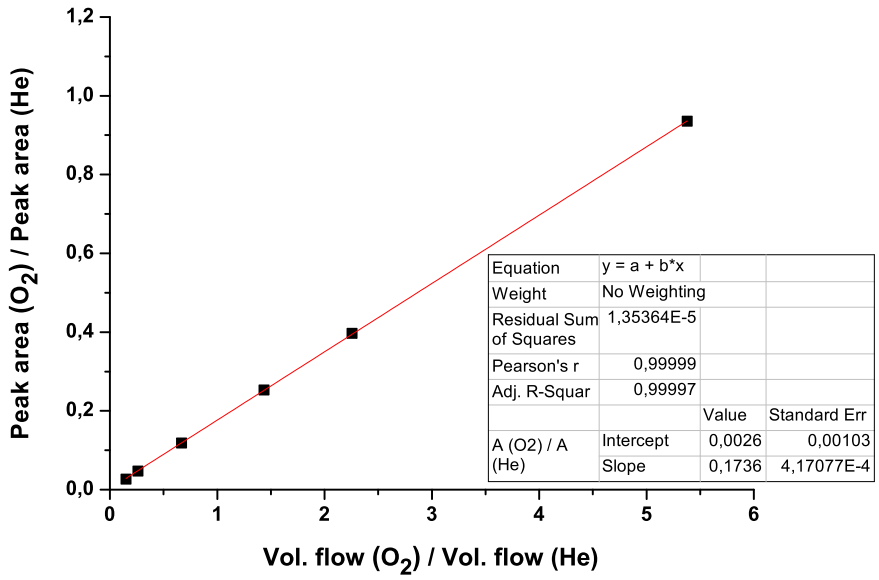

(b)

Figure 5: Micro GC calibration curves with plot parameters of (a) CH_4; (b) O_2. Part I.

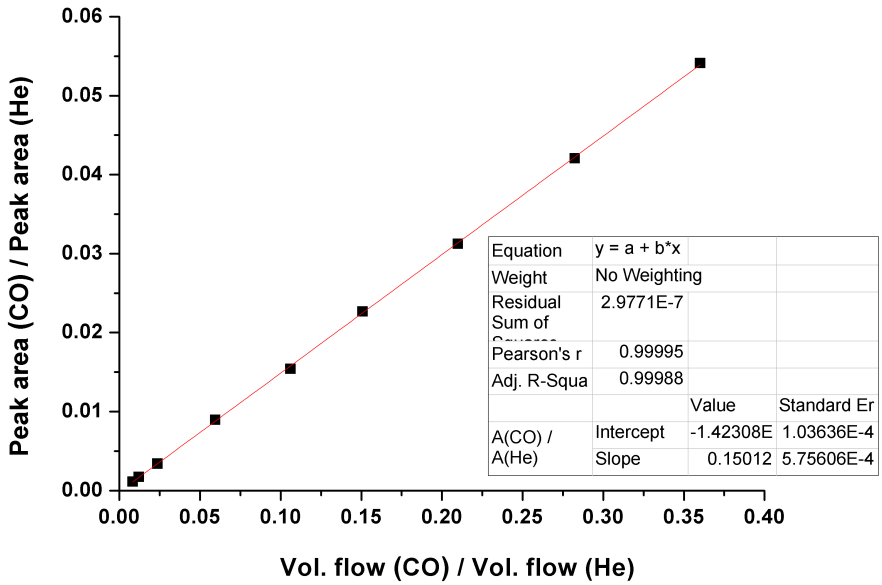

(a)

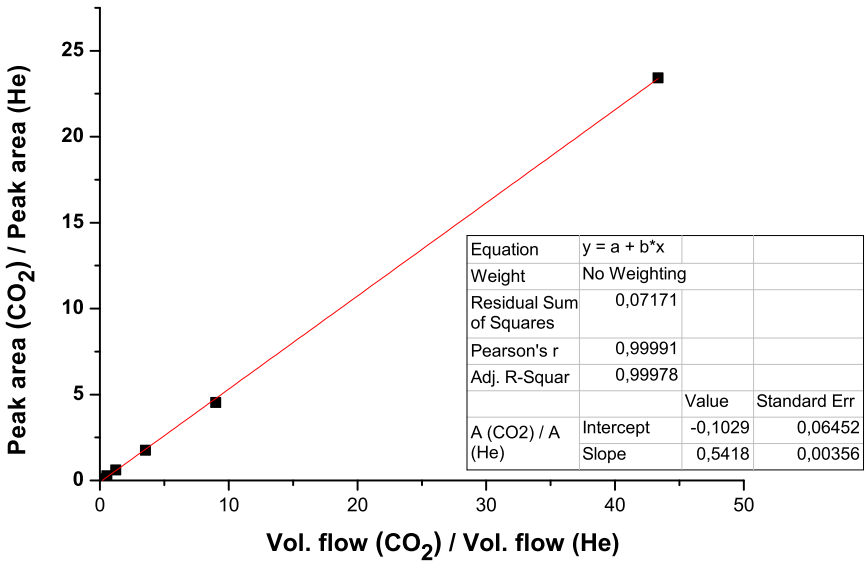

(b)

Figure 6: Micro GC calibration curves with plot parameters of (a) CO; (b) CO_2. Part II.

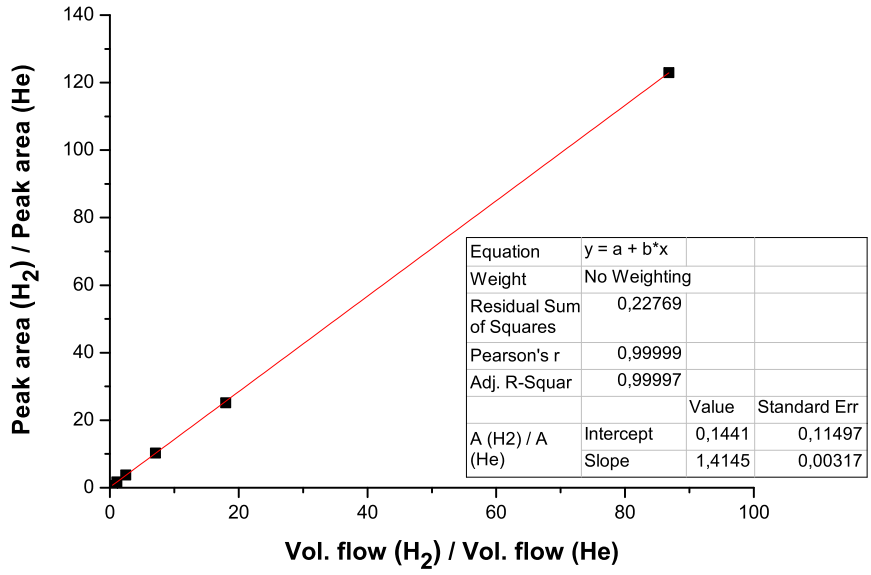

(a)

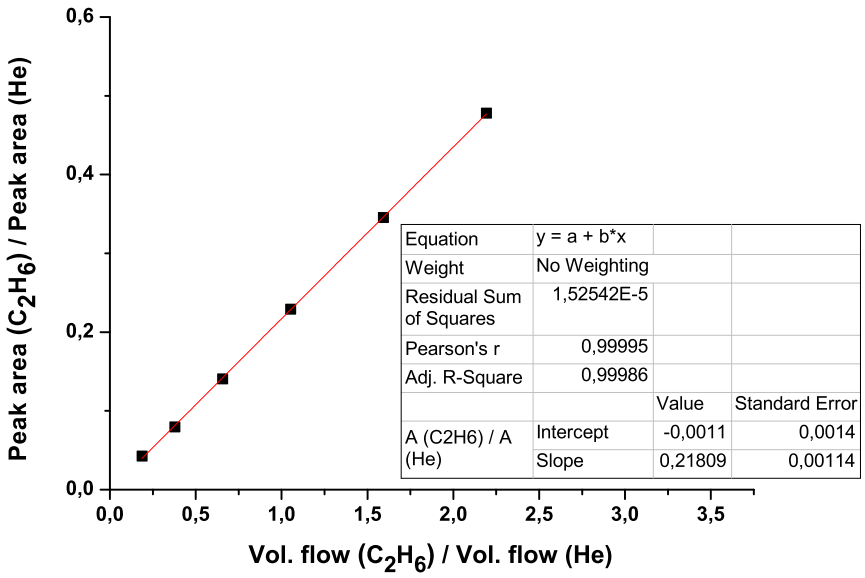

(b)

Figure 7: Micro GC calibration curves with plot parameters of (a) H_2; (b) C_2H_6. Part III.

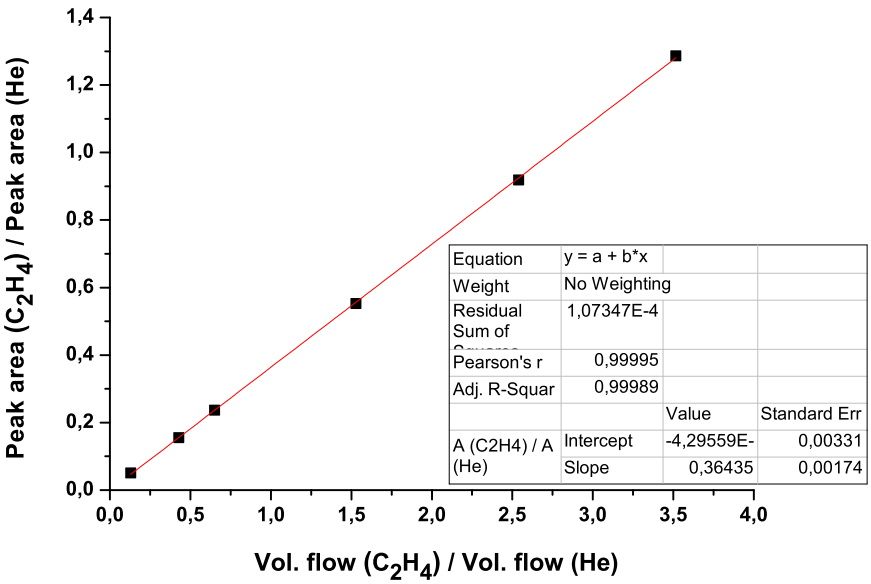

Figure 8: GC calibration curve with plot parameters of C_2H_4. Part IV.

Appendix B MATLAB Script for Fast Evaluation of Profiles

Spatially resolved profiles are a data containing large number of data points (from GS, MS, thermocouple/pyrometer) demanding a tedious time-consuming analysis procedure. A MATLAB script [1] was compiled for quick evaluation of the raw data from spatial profile reactor measurements. The initial files to be input for evaluation are the MS spectra (ASCII format), temperature reading (CSV format) and micro GC peak areas (files from the instrument software), together with measurement starting times of the analytical instruments, thermocouple/pyrometer and of the high-precision motor. For the high-precision motor, its translational velocity in counts/sec (1 μm = 56.88889 counts). Besides, positions inside the reactor are also given in counts from the motor. The script allowed to evaluate the data in ca. 60 s. Description of most operations done in the script are given after the % comment signs.

```
1
2 %------------------------------------------------------------------------------------%
3 %Program for evaluating of species profiles and temperature
    profiles:      %
4 %Uses iterative substraction of m/z for C2 quantification and does
    not     %
5 %include oxygenate species; this script evaluates temperature
    profiles of %
6 %a thermocouple as temperature probe, no background correction
    included    %
7 %by Oliver Korup, 2011
                                                                    %
8 %------------------------------------------------------------------------------------%
```

[1] The script was developed by Oliver Korup [113], FHI

```
clear
format long g

tic
disp('PROGRAM FOR QUICK PROFILE EVALUATION')
disp('Processing, please wait.')

%-------------------------------------------------------------------------------%
%Input calculation parameters                                                   %
%-------------------------------------------------------------------------------%

%Input filenames of ASCII raw data
%-----------------------------------

MSfilename='down_ctoo4_2000ml_set750c8bar_1000cs_05082011.asc';
Tcfilename='temp_down_ctoo4_2000ml_set750c_8bar_1000cs_05082011.CSV';
GC1filename='down_ctoo4_2000ml_set750c_8bar_1000cs-Channel 1 10m MS5A Heated Injector, Backflush.Area';
GC2filename='down_ctoo4_2000ml_set750c_8bar_1000cs-Channel 2 10m PPU Heated Injector, Backflush.Area';
GC3filename='down_ctoo4_2000ml_set750c_8bar_1000cs-Channel 3 10m AL2O3-KCL Heated Inj, Backflush.Area';
%GC4filename=''; %not used in methane OCM

%Input of stack coordinates (!!!In counts relative to FHS bottom side!!!)
%-----------------------------------------------------------------------
FHS_bottom=0; %This must be zero!
FHS_top=1103645;
BHS_bottom=5683201;
BHS_top=6280534;
translation_top=6564987;
translation_bottom=-284444;
translation_velocity=1000;
translation_direction=1; % "1" represents running down; "2" represents running up
start_MS=0; % Master time index in profile measurements [s]
start_GC=60; %Delay to master time index [s]
start_Tc=120; % Delay to master time index [s]
start_Motor=300; % Delay to master time index [s]

%Integration limits for MS data evaluation !!! Have a look on the spectra!!!
%-------------------------------------------------------------------------------
IP=[1 0.91 1.56
    2 1.56 2.69
    3 2.69 3.62
    4 3.62 4.62
```

```
    5 NaN NaN
    6 NaN NaN
    7 NaN NaN
    8 NaN NaN
    9 NaN NaN
    10 NaN NaN
    11 NaN NaN
    12 11.56 12.53
    13 12.53 13.56
    14 13.56 14.53
    15 14.53 15.56
    16 15.56 16.59
    17 16.59 17.53
    18 17.53 18.56
    19 18.56 19.41
    20 19.41 20.56
    21 NaN NaN
    22 21.56 22.44
    23 NaN NaN
    24 23.50 24.50
    25 24.50 25.44
    26 25.44 26.47
    27 26.47 27.38
    28 27.28 28.50
    29 28.50 29.44
    30 29.44 30.50
    31 30.41 31.19
    32 31.19 32.56
    33 32.56 33.38
    34 33.38 34.31
    35 34.31 35.25
    36 35.25 36.41
    37 36.41 37.34
    38 37.34 38.34
    39 NaN NaN
    40 38.44 40.50
    41 40.50 41.34
    42 NaN NaN
    43 NaN NaN
    44 43.06 44.44
    45 44.41 45.31
    46 45.31 46.31
    47 NaN NaN
    48 NaN NaN
    49 NaN NaN
    50 NaN NaN];

%Gas feed composition [mln/min]
%-----------------------------------
```

```
FCH4=1705; %Calculation of the flow according to Oliver's MFC calibration (with suitable flow range) on March 2011 is 1705
FO2=226.6; %Calculation of the flow according to Oliver's MFC calibration (with suitable flow range) on March 2011 is 226.6
FAr=211.14; %Considering 92% Argon in the flow of Ar-He mixture. Calculation of the flow according to Oliver's MFC calibration (with suitable flow range) on March 2011 is Ar only=211.14 (Ar-He=229.51 ml/min)

FCH4=FCH4/1000000; % Converted to SI system
FO2=FO2/1000000;
FAr=FAr/1000000;

%MS calibration data (slope of calibration line)
%-----------------------------------------------------
%1. H2
mH2calib=8.40336; %%Calibration date 02.09.2009 (2/40)
%2. CH4
mCH4calib=1.24005; %Calibration date 17.10.2011 (15/40) in pure Ar by Sardor
%3. CO
mCOcalib=1.20395; %Calibration date 25.07.2011 (28/40) by Oliver
%4. O2
mO2calib=0.96776; %Calibration date 17.10.2011 (32/40) in pure Ar by Sardor
%5. CO2
mCO2calib=1.0319; %Calibration date 25.07.2011 (44/40) by Oliver
mCOfromCO2calib=0.09258; %Calibration date 25.07.2011 (28/40)
%6. C2H4
mC2H4calib=0.5583; %Calibration of Micha 15.06.2010
%7. C2H6
mC2H6calib=0.29722; %Calibration of Micha 15.06.2010

%GC calibration data (slope of calibration line)
%-----------------------------------------------------
%1. H2 on column 1
mH2calibGC1=1.41455; %Sardor 20.04.2011 (m=(A_H2/A_He)/(F_H2/F_(Ar+He))
%2. CH4 on column 1
mCH4calibGC1=0.34; %Sardor 20.04.2011 (m=(A_CH4/A_He)/(F_H2/F_(Ar+He)). Correction of the response factor to get flow that should be acc to ideal gas law
%3. CO on column 1
mCOcalibGC1=0.15012; %Sardor 25.02.2011 (m=(A_CO/A_He)/(F_H2/F_(He))!!! This is done in pure He not in the Ar/He=92/8 mixture.
%4. O2 on column 1
mO2calibGC1=0.169; %Sardor 20.04.2011 (m=(A_O2/A_He)/(F_H2/F_(Ar+He)). Correction of the response
```

```
    factor to get flow that should be acc to ideal gas law
%5. CO2 on column 2
mCO2calibGC2=0.5418; %Sardor 20.04.2011 (m=(A_CO2/A_He)/(F_H2/F_(Ar+He))
%6. C2H4 on column 3
mC2H4calibGC3=0.36435; %Sardor 20.04.2011 (m=(A_C2H4/A_He)/(F_H2/F_(Ar+He))
%7. C2H6 on colum 3
mC2H6calibGC3=0.2180; %Sardor 20.04.2011 (m=(A_C2H6/A_He)/(F_H2/F_(Ar+He))


%Other parameters/constant
%-------------------------
R=8.31447215; %Universal gas constant [J*mol^-1*k^-1]
MScyclelength=3650/333; %Duration for a MS cycle [s]

%-----------------------------------------------------------------------------------%
%Read raw data to workspace                                                         %
%-----------------------------------------------------------------------------------%

%MS
%--
data=dlmread(MSfilename,'\t');
[a,b]=size(data);
[c,d]=size(IP);

%Thermocouple
%------------
[fid, message]=fopen(Tcfilename,'rt');
if fid==-1, %File doesn't exist?
    disp('Input file does not exist!');
    return;
else %Ok it exists
    i=1;
    count=0;
    while feof(fid)==0,
        header=fgetl(fid);
        count=count+1;
        if findstr(header,'MAIN.PV'), %Search for key word, i.e. the headers end
            index(i)=count;
            i=i+1;
            offset=count; %Offset from key word
        end
    end
end
```

```
[c1,c2,c3,c4, c5]=textread(Tcfilename, '%f %f %d %f %f',
    'delimiter', ',', 'headerlines', offset);
[Ttc_rawdata]=[c1,c2,c3,c4,c5];
clear c1 c2 c3 c4 c5;
fclose(fid);

%GC
%--
%Channel1
%--------
[fid, message]=fopen(GC1filename,'rt');
if fid==-1, %File doesn't exist?
    disp('Input file does not exist!');
    return;
else %Ok it exists
    i=1;
    count=0;
    while feof(fid)==0,
        header=fgetl(fid);
        count=count+1;
        if findstr(header,'Autosampler Program He H2
            O2 N2 CH4 CO'), %Search for key word, i.e.
            the headers end
            index(i)=count;
            i=i+1;
            offset=count; %Offset from key word
        end
    end
end
[c1,c2,c3,c4,c5,c6,c7,c8,c9,c10,c11,c12,c13,c14,c15]=textread(GC1filename,
    '%s %s %s %s %s %s %d %s %s %d %d %d %d %d %d', 'delimiter',
    '\t', 'headerlines', offset);
fclose(fid);
c1=strrep(c1,'.','/');
c1=datevec(c1);
c2=datevec(c2);
GC1rawdata=[c1(:,1),c1(:,2),c1(:,3),c2(:,4),c2(:,5),c2(:,6),c10,c11,
c12,c13,c14,c15]; %Format: Y, M, D, H, M, S, He, H2, O2, N2, CH4, CO

%Channel2
%--------
[fid, message]=fopen(GC1filename,'rt');
if fid==-1, %File doesn't exist?
    disp('Input file does not exist!');
    return;
else %Ok it exists
    i=1;
    count=0;
    while feof(fid)==0,
```

```
        header=fgetl(fid);
        count=count+1;
        if findstr(header,'Autosampler Program  CO2     C2H4
            C2H6    C2H2'), %Search for key word, i.e. the headers
            end
            index(i)=count;
            i=i+1;
            offset=count; %Offset from key word
        end
    end
end
[c1,c2,c3,c4,c5,c6,c7,c8,c9,c10,c11,c12,c13]=textread(GC2filename,
    '%s %s %s %s %s %s %d %s %s %d %d %d %d', 'delimiter', '\t',
    'headerlines', offset);
fclose(fid);
c1=strrep(c1,'.','/');
c1=datevec(c1);
c2=datevec(c2);
GC2rawdata=[c1(:,1),c1(:,2),c1(:,3),c2(:,4),c2(:,5),c2(:,6),c10,c11,c12,c13];
    %Format: Y, M, D, H, M, S, CO2, C2H4, C2H6, C2H2

%Channel3
%--------
[fid, message]=fopen(GC1filename,'rt');
if fid==-1, %File doesn't exist?
    disp('Input file does not exist!');
    return;
else %Ok it exists
    i=1;
    count=0;
    while feof(fid)==0,
        header=fgetl(fid);
        count=count+1;
        if findstr(header,'Autosampler Program  C2H6    C2H4
            C3H8    C3Hx    C2H2'), %Search for key word, i.e. the
            headers end
            index(i)=count;
            i=i+1;
            offset=count; %Offset from key word
        end
    end
end
[c1,c2,c3,c4,c5,c6,c7,c8,c9,c10,c11,c12,c13,c14]=textread(GC3filename,
    '%s %s %s %s %s %s %d %s %s %d %d %d %d %d', 'delimiter', '\t',
    'headerlines', offset);
fclose(fid);
c1=strrep(c1,'.','/');
c1=datevec(c1);
c2=datevec(c2);
```

```
GC3rawdata=[c1(:,1),c1(:,2),c1(:,3),c2(:,4),c2(:,5),c2(:,6),c10,c11,
c12,c13,c14]; %Format: Y, M, D, H, M, S, C2H6, C2H4, C3H8, C3Hx,
    C2H2

%Channel4
%--------
%not used in methane OCM

clear c1 c2 c3 c4 c5 c6 c7 c8 c9 c10 c11 c12 c13 c14 c15 count fid
    header i index message offset ans;

%-------------------------------------------------------------------------%
%Calculations
                                                                        %
%-------------------------------------------------------------------------%

%% Evaluate MS data

%Integration MS raw data in given interval
%-----------------------------------------
for spectrum=1:(b-1),
    for peak=1:c,
        pos1=int2str(spectrum);
        pos2=int2str(peak);
        for l=1:a,
            if data(l,1)==IP(peak,2);
                indexx0=l;
            else
            end
        end
        for l=1:a,
            if data(l,1)==IP(peak,3),
                indexx1=l;
            else
            end
        end
    x=data(indexx0:indexx1,1);
    y=data(indexx0:indexx1,(spectrum+1));
    MS_peakareas(spectrum,peak)=trapz(x',y);
    end
end
clear IP a b c d data indexx0 indexx1 l peak pos1 pos2 spectrum x y;

%Calculate m/z ratios for reactants and products (H2 (2), CH4 (15),
    H2O (18),
%C2H4 (27), CO (28), C2H6 (30), O2 (32), Ar (40), CO2 (44))
%----------------------------------------------------------------------
H2Ar=MS_peakareas(:,2)./MS_peakareas(:,40);
CH4Ar=MS_peakareas(:,15)./MS_peakareas(:,40);
```

```
H2OAr=MS_peakareas(:,18)./MS_peakareas(:,40);
C2H4Ar=MS_peakareas(:,27)./MS_peakareas(:,40);
COAr=MS_peakareas(:,28)./MS_peakareas(:,40);
C2H6Ar=MS_peakareas(:,30)./MS_peakareas(:,40);
O2Ar=MS_peakareas(:,32)./MS_peakareas(:,40);
CO2Ar=MS_peakareas(:,44)./MS_peakareas(:,40);

%Calculate species molecular flow with respect to calibration data MS
%-----------------------------------------------------------------------
%1. CH4
%------
%CH4profile=(CH4Ar./mCH4calib).*(101325*FAr/R/298.15); %[mol/min]

    %-----------------------------------------------------------------------
    %Alternatively calculated with one point calibration from gas feed
    %composition and blank in front heat shield
    %-----------------------------------------------------------------------
    if translation_direction==1,
        h1=(translation_top-translation_bottom)/translation_velocity; %Time until full profile run completed [s]
        h2=round(h1/MScyclelength); %Number (integer) of MS cycles in a full profile run
        blank=0;
        for i=h2-6:1:h2; %Seven cycles from the end of profile run, i.e. sampling position in or prior to the FHS
            blank=blank+CH4Ar(i);
        end
        blank=blank/7;
        CH4profile=CH4Ar.*(FCH4*101325/R/298.15/blank);
    elseif translation_direction==2,
        h1=(translation_top-translation_bottom)/translation_velocity; %Time until full profile run completed [s]
        h2=round(h1/MScyclelength); %Number (integer) of MS cycles in a full profile run
        blank=0;
        for i=2:1:8, %Seven cycles, first cycle is neglected, sampling position in or prior to the FHS
            blank=blank+CH4Ar(i);
        end
        blank=blank/7;
        CH4profile=CH4Ar.*(FCH4*101325/R/298.15/blank);
    else
    end

%2. O2
%-----
%O2profile=(O2Ar./mO2calib).*(101325*FAr/R/298.15); %[mol/min]
```

```
    %-----------------------------------------------------------------------
    %Alternatively calculated with one point calibration from gas feed
    %composition and blank in front heat shield
    %-----------------------------------------------------------------------
    if translation_direction==1,
        h1=(translation_top-translation_bottom)/translation_velocity; %Time until full profile run completed [s]
        h2=round(h1/MScyclelength); %Number (integer) of MS cycles in a full profile run
        blank=0;
        for i=h2-6:1:h2; %Seven cycles from the end of profile run, i.e. sampling position in or prior to the FHS
            blank=blank+O2Ar(i);
        end
        blank=blank/7;
        O2profile=O2Ar.*(FO2*101325/R/298.15/blank);
    elseif translation_direction==2,
        h1=(translation_top-translation_bottom)/translation_velocity; %Time until full profile run completed [s]
        h2=round(h1/MScyclelength); %Number (integer) of MS cycles in a full profile run
        blank=0;
        for i=2:1:8, %Seven cycles, first cycle is neglected, sampling position in or prior to the FHS
            blank=blank+O2Ar(i);
        end
        blank=blank/7;
        O2profile=O2Ar.*(FO2*101325/R/298.15/blank);
    else
    end

%3. CO2
%------
CO2profile=(CO2Ar./mCO2calib).*(101325*FAr/R/298.15); %[mol/min]

%4. C2H6
%-------
C2H6profile=(C2H6Ar./mC2H6calib).*(101325*FAr/R/298.15); %[mol/min]

%5. C2H4
%-------
C2H4profile=((C2H4Ar-((0.3323/0.2622)*C2H6Ar))./mC2H4calib).
*(101325*FAr/R/298.15);

%6. CO
%-----
COprofile=((COAr-((0.9999/0.2622)*C2H6Ar)-
```

```
(0.9999/0.6236)*(C2H4Ar-((0.3323/0.2622)*C2H6Ar))-
((0.0981/0.9999)*CO2Ar))./mCOcalib).*(101325*FAr/R/298.15);
    %[mol/min]

%7. H2
%-----
H2profile=(H2Ar./mH2calib).*(101325*FAr/R/298.15); %[mol/min]

%8. H2O calculation from O balance
%-----------------------------------
i=length(MS_peakareas(:,1));
h1=ones(i,1);
H2Oprofile=(2*(FO2*101325/R/298.15)*h1)-COprofile-2*O2profile-2*CO2profile;
    %[mol/min]

clear CH4Ar CO2Ar COAr H2Ar H2OAr C2H4Ar C2H6Ar O2Ar blank i
    mCH4calib mCO2calib mCOcalib mH2calib mO2calib mC2H4calib
    mC2H6calib mCOfromCO2calib;

%Calculate mass balances MS
%-------------------------
%1. C
%----
Cbalance=((((101325*FCH4/R/298.15)*h1)-CH4profile-COprofile-CO2profile-
2*C2H4profile-2*C2H6profile)./(101325*FCH4/R/298.15).*100); %[%]
%2. H
%----
Hbalance=(((4*(101325*FCH4/R/298.15)*h1)-2*H2profile-4*CH4profile-2*H2Oprofile-
4*C2H4profile-6*C2H6profile)./(4*(101325*FCH4/R/298.15)).*100); %[%]
%3. O
%----
Obalance=(((2*(101325*FO2/R/298.15)*h1)-COprofile-2*O2profile-2*CO2profile-
H2Oprofile)./(2*(101325*FO2/R/298.15)).*100); %[%]

clear h1;

%Calculate mole fraction of all species from molar flow rates MS
%-------------------------------------------------------------
tmp=ones(length(O2profile),1);
Arprofile=tmp.*((FAr*101325)/(R*298.15));
Heprofile=tmp.*((((FAr/0.92)-FAr)*101325)/(R*298.15)); %In case the
    Ar/He mixture with 8% He is used
Sumprofile=Arprofile+Heprofile+COprofile+CO2profile+O2profile+H2Oprofile+
H2profile+CH4profile+C2H4profile+C2H6profile;

XArprofile=Arprofile./Sumprofile;
XHeprofile=Heprofile./Sumprofile;
XCOprofile=COprofile./Sumprofile;
XCO2profile=CO2profile./Sumprofile;
```

```
XO2profile=O2profile./Sumprofile;
XH2Oprofile=H2Oprofile./Sumprofile;
XH2profile=H2profile./Sumprofile;
XCH4profile=CH4profile./Sumprofile;
XC2H4profile=C2H4profile./Sumprofile;
XC2H6profile=C2H6profile./Sumprofile;
CheckSum=XArprofile+XHeprofile+XCOprofile+XCO2profile+XO2profile+
XH2Oprofile+XH2profile+XCH4profile+XC2H4profile+XC2H6profile;

%% Evaluate GC data
%-----------------

%Calculate relative GC peak areas
%-------------------------------------
H2He=GC1rawdata(:,8)./GC1rawdata(:,7);
O2He=GC1rawdata(:,9)./GC1rawdata(:,7);
CH4He=GC1rawdata(:,11)./GC1rawdata(:,7);
COHe=GC1rawdata(:,12)./GC1rawdata(:,7);
CO2He=GC2rawdata(:,7)./GC1rawdata(:,7);
C2H4He=GC3rawdata(:,8)./GC1rawdata(:,7);
C2H6He=GC3rawdata(:,7)./GC1rawdata(:,7);

%%Calculate species molecular flow with respect to calibration data
    GC
%-------------------------------------------------------------------
%1. H2
%-----
GCH2profile=H2He./mH2calibGC1.*((FAr/0.92-FAr)*101325/R/298.15);
    %F_Ar+He = F_Ar/0.92, because of 8% He in Ar mixture
%2. CO2
%------
GCO2profile=O2He./mO2calibGC1.*((FAr/0.92-FAr)*101325/R/298.15);
%3. CO
%-----
GCCOprofile=COHe./mCOcalibGC1.*((FAr/0.92-FAr)*101325/R/298.15);
    %correction for different calibration method, see calibration
    data Sardor
%4. CH4
%------
GCCH4profile=CH4He./mCH4calibGC1.*((FAr/0.92-FAr)*101325/R/298.15);
%5. CO2
%------
GCCO2profile=CO2He./mCO2calibGC2.*((FAr/0.92-FAr)*101325/R/298.15);
%6. C2H4
%-------
GCC2H4profile=C2H4He./mC2H4calibGC3.*((FAr/0.92-FAr)*101325/R/298.15);
%7. C2H6
%-------
GCC2H6profile=C2H6He./mC2H6calibGC3.*((FAr/0.92-FAr)*101325/R/298.15);
```

```
%8. H2O calculation from O balance
%-----------------------------------
i=length(GC1rawdata(:,1));
h1=ones(i,1);
GCH2Oprofile=(2*(FO2*101325/R/298.15)*h1)-GCCOprofile-
2*GCO2profile-2*GCCO2profile; %[mol/min]

%Calculate mass balances GC
%-------------------------
%1. C
%----
GCCbalance=((((101325*FCH4/R/298.15)*h1)-GCCH4profile-GCCOprofile-GCCO2profile-
2*GCC2H4profile-2*GCC2H6profile)./(101325*FCH4/R/298.15).*100); %[%]
%2. H
%----
GCHbalance=(((4*(101325*FCH4/R/298.15)*h1)-2*GCH2profile-4*GCCH4profile-
2*GCH2Oprofile-4*GCC2H4profile-6*GCC2H6profile)./(4*(101325*FCH4/R/298.15)).*100);
    %[%]
%3. O
%----
GCObalance=(((2*(101325*FO2/R/298.15)*h1)-GCCOprofile-2*GCO2profile-
2*GCCO2profile-GCH2Oprofile)./(2*(101325*FO2/R/298.15)).*100); %[%]

clear h1 H2He C2H6He CH4He CO2He COHe mC2H4calibGC3 mC2H6calibGC3
    mCH4calibGC1 mCO2calibGC2 mCOcalibGC1 mH2calibGC1 mO2calibGC1;

%Calculate mole fraction of all species from molar flow rates GC
%-----------------------------------------------------------------
tmp=ones(length(GCO2profile),1);
GCArprofile=tmp.*((FAr*101325)/(R*298.15));
GCHeprofile=tmp.*((((FAr/0.92)-FAr)*101325)/(R*298.15)); %In case
    the Ar/He mixture with 8% He is used
GCSumprofile=GCArprofile+GCHeprofile+GCCOprofile+GCCO2profile+GCO2profile+
GCH2Oprofile+GCH2profile+GCCH4profile+GCC2H4profile+GCC2H6profile;

GCXArprofile=GCArprofile./GCSumprofile;
GCXHeprofile=GCHeprofile./GCSumprofile;
GCXCOprofile=GCCOprofile./GCSumprofile;
GCXCO2profile=GCCO2profile./GCSumprofile;
GCXO2profile=GCO2profile./GCSumprofile;
GCXH2Oprofile=GCH2Oprofile./GCSumprofile;
GCXH2profile=GCH2profile./GCSumprofile;
GCXCH4profile=GCCH4profile./GCSumprofile;
GCXC2H4profile=GCC2H4profile./GCSumprofile;
GCXC2H6profile=GCC2H6profile./GCSumprofile;
GCCheckSum=GCXArprofile+GCXHeprofile+GCXCOprofile+GCXCO2profile+GCXO2profile+
GCXH2Oprofile+GCXH2profile+GCXCH4profile+GCXC2H4profile+GCXC2H6profile;

clear tmp;
```

```
%%
%-----------------------------------------------------------------------------%
%Transform time coordinate to spatial coordinate and plot results %
%-----------------------------------------------------------------------------%
%1. Thermocouple
%----------------
if translation_direction==1,
    i=length(Ttc_rawdata(:,1));
    h1=ones(i,1); h3=h1;
    h1=h1*Ttc_rawdata(1,1);
    h2=(Ttc_rawdata(:,1)-h1)*86400;
    h4=(((translation_top*h3)-(h2-
    (h3*(start_Motor-start_Tc)))*translation_velocity)+\\
    (h3*(FHS_bottom-FHS_top)))/56.88889;
    %This formula is: Uppermost position - velocity * time (pyrometer time
    %index - delay to master time index) + corrected to zero position to begin
    %at the catalyst bed bottom divided by number of counts per micrometer
    clear h1 h2 h3;
elseif translation_direction==2, %now comes exactly the same as in case of down movement with one difference the starting position of the movement is the lowest spatial position
    i=length(Ttc_rawdata(:,1));
    h1=ones(i,1); h3=h1;
    h1=h1*Ttc_rawdata(1,1);
    h2=(Ttc_rawdata(:,1)-h1)*86400;
    h4=(((translation_bottom*h3)+(h2-
    (h3*(start_Motor-start_Tc)))*translation_velocity)+
    (h3*(FHS_bottom-FHS_top)))/56.88889;
    %This formula is: Uppermost position + velocity * time (pyrometer time
    %index - delay to master time index) + corrected to zero position to begin
    %at the catalyst bed bottom divided by number of counts per micrometer
    clear h1 h2 h3;
else
end

%Plot results - Thermocouple
%---------------------------
    figure;
    plot(h4,Ttc_rawdata(:,5),h4,Ttc_rawdata(:,2),h4,Ttc_rawdata(:,3));
    legend('T thermocouple stack center','T thermocouple furnace center rim','T furnace setpoint center rim');
    axis([(FHS_bottom-FHS_top)/56.88889,(BHS_top+FHS_bottom-
```

```
565     FHS_top)/56.88889,min(Ttc_rawdata(:,5)-100),max(Ttc_rawdata(:,5)+100)]);
566     xlabel('sampling position [m]');
567     ylabel('thermocouple temperature [C]');
568     line([0,0],ylim,'color',[0,0,0]); %Line at catalyst bed
            beginning
569     line([(BHS_bottom+FHS_bottom-FHS_top)/56.88889,(BHS_bottom+FHS_bottom-
570     FHS_top)/56.88889],ylim,'color',[0,0,0]); %Line at catalyst bed
            end
571     resultTc=[h4,Ttc_rawdata(:,5),Ttc_rawdata(:,2),Ttc_rawdata(:,3)];
            resultTcLabel=[cellstr('axial position thermocouple [m]'),
            cellstr('T thermocouple stack center[C]'), cellstr('T
            thermocouple furnace center rim [C]'), cellstr('T furnace
            setpoint center rim[C]')]; %For storage of result data
572     clear h4;
573
574 %3. MS species & balances
575 %-----------------------
576 if translation_direction==1,
577     h1=[1:length(H2profile)];
578     h1=reshape(h1,[],1);
579     h2=(h1*MScyclelength);
580     h3=ones(length(H2profile),1);
581     h4=(((translation_top*h3)-
582     (h2-(h3*(start_Motor-start_MS)))*translation_velocity)+
583     (h3*(FHS_bottom-FHS_top)))/56.88889;
584     clear h1 h2 h3;
585 elseif translation_direction==2,
586     h1=[1:length(H2profile)];
587     h1=reshape(h1,[],1);
588     h2=(h1*MScyclelength);
589     h3=ones(length(H2profile),1);
590     h4=(((translation_bottom*h3)+
591     (h2-(h3*(start_Motor-start_MS)))*translation_velocity)+
592     (h3*(FHS_bottom-FHS_top)))/56.88889;
593     clear h1 h2 h3;
594 else
595 end
596
597 %4. GC species & balances
598 %-----------------------
599 if translation_direction==1,
600     if
            sum(GC1rawdata(:,3))/length(GC1rawdata(:,3))==GC1rawdata(1,3),
            %Check if data are recorded crossing midnight (importent for
            correct time to position assingment)
601         h1=GC1rawdata(1,6)+GC1rawdata(1,5)*60+GC1rawdata(1,4)*3600;
602         h2=[];
603         for i=1:length(GC1rawdata(:,1)),
604             h2=[h2;GC1rawdata(i,6)+GC1rawdata(i,5)*60+GC1rawdata(i,4)*3600-h1];
```

```
        end
        h3=ones(length(GCH2profile),1);
        h5=(((translation_top*h3)-
        (h2-(h3*(start_Motor-start_MS)))*translation_velocity)+
        (h3*(FHS_bottom-FHS_top)))/56.88889;
    else
        %needs to be done as soon as a test case exists
    end
    clear h1 h2 h3;
elseif translation_direction==2,
    if
       sum(GC1rawdata(:,3))/length(GC1rawdata(:,3))==GC1rawdata(1,3),
       %Check if data are recorded crossing midnight (importent for
        correct time to position assingment)
        h1=GC1rawdata(1,6)+GC1rawdata(1,5)*60+GC1rawdata(1,4)*3600;
        h2=[];
        for i=1:length(GC1rawdata(:,1)),
            h2=[h2;GC1rawdata(i,6)+GC1rawdata(i,5)*60+GC1rawdata(i,4)*3600-h1];
        end
        h3=ones(length(GCH2profile),1);
        h5=(((translation_bottom*h3)+
        (h2-(h3*(start_Motor-start_MS)))*translation_velocity)+
        (h3*(FHS_bottom-FHS_top)))/56.88889;
    else
        %needs to be done as soon as a test case exists
    end
    clear h1 h2 h3;
end


%Plot results - Species
%----------------------
figure;
plot(h4,H2profile,'k-',h4,CH4profile,'r-',h4,H2Oprofile,'c-',h4,COprofile,
'm-',h4,O2profile,'b-',h4,CO2profile,'g-',h4,C2H4profile,'r-',h4,C2H6profile,
'b-',h5,GCH2profile,'ko',h5,GCCH4profile,'ro',h5,GCH2Oprofile,'co',h5,
GCCOprofile,'mo',h5,GCO2profile,'bo',h5,GCCO2profile,'go',h5,GCC2H4profile,
'ro',h5,GCC2H6profile,'bo');
legend('H_2','CH_4','H_2O','CO','O_2','CO_2','C_2H_4',
'C_2H_6','H_2','CH_4','H_2O','CO','O_2','CO_2','C_2H_4','C_2H_6');
axis([(FHS_bottom-FHS_top)/56.88889,(BHS_top+FHS_bottom-FHS_top)/56.88889,
-0.01,max(CH4profile)*1.25]);
xlabel('sampling position [m]');
ylabel('molar flow rate [mol/min]');
line([0,0],ylim,'color',[0,0,0]);
line([(BHS_bottom+FHS_bottom-FHS_top)/56.88889,
(BHS_bottom+FHS_bottom-FHS_top)/56.88889],ylim,'color',[0,0,0]);
```

```
%Plot results - Balances
%-----------------------------
figure;
plot(h4,Cbalance,'r-',h4,Hbalance,'b-',h4,Obalance,
'k-',h5,GCCbalance,'ro',h5,GCHbalance,'bo',h5,GCObalance,'ko');
legend('carbon balance','hydrogen balance','oxygen balance');
axis([(FHS_bottom-FHS_top)/56.88889,
(BHS_top+FHS_bottom-FHS_top)/56.88889,-100,+100]);
xlabel('sampling position [m]');
ylabel('deviation from closed mass balance [%]');
line([0,0],ylim,'color',[0,0,0]);
line([(BHS_bottom+FHS_bottom-FHS_top)/56.88889,
(BHS_bottom+FHS_bottom-FHS_top)/56.88889],ylim,'color',[0,0,0]);

%Plot results - Mole fractions (all)
%-----------------------------------------
figure;
plot(h4,XArprofile,'y-',h4,XHeprofile,'c-',h4,XCOprofile,'m-',
h4,XO2profile,'b-',h4,XCO2profile,'g-',h4,XH2Oprofile,'c-',
h4,XH2profile,'k-',h4,XCH4profile,'r-',h4,XC2H4profile,'r-',
h4,XC2H6profile,'b-',h4,CheckSum,'k-',h5,GCXArprofile,'yo',
h5,GCXHeprofile,'co',h5,GCXCOprofile,'mo',h5,GCXO2profile,'bo',
h5,GCXCO2profile,'go',h5,GCXH2Oprofile,'co',h5,GCXH2profile,'ko'
,h5,GCXCH4profile,'ro',h5,GCXC2H4profile,'ro',h5,GCXC2H6profile,'bo',
h5,GCCheckSum,'ko')
legend('Ar','He','CO','O_2','CO_2','H_2O','H_2','CH_4','C_2H_4','C_2H_6','Sum
    X_i','Ar','He','CO','O_2','CO_2','H_2O','H_2','CH_4','C_2H_4','C_2H_6','Sum
    X_i');

axis([(FHS_bottom-FHS_top)/56.88889,
(BHS_top+FHS_bottom-FHS_top)/56.88889,-0.01,1.01]);
xlabel('sampling position [m]');
ylabel('mole fraction');
line([0,0],ylim,'color',[0,0,0]);
line([(BHS_bottom+FHS_bottom-FHS_top)/56.88889,
(BHS_bottom+FHS_bottom-FHS_top)/56.88889],ylim,'color',[0,0,0]);
resultSpeciesBalancesMoleFractions=[h4,H2profile,CH4profile,H2Oprofile,
COprofile,O2profile,CO2profile,C2H4profile,C2H6profile,Cbalance,Hbalance,
Obalance,XArprofile,XHeprofile,XCOprofile,XO2profile,XCO2profile,XH2Oprofile,
XH2profile,XCH4profile,XC2H4profile,
XC2H6profile,CheckSum]; %For storage of result data
resultSpeciesBalancesMoleFractionsLabel=[cellstr('axial position
    species/balances [m]'), cellstr('F H2 [mol/min]'), cellstr('F
    CH4 [mol/min]'), cellstr('F H2O [mol/min]'), cellstr('F CO
    [mol/min]'), cellstr('F O2 [mol/min]'), cellstr('F CO2
    [mol/min]'), cellstr('F C2H4 [mol/min]'), cellstr('F C2H6
    [mol/min]'), cellstr('C balance [percent]'), cellstr('H balance
    [percent]'), cellstr('O balance [percent]'), cellstr('X_Ar'),
    cellstr('X_He'), cellstr('X_CO'), cellstr('X_CO2'),
```

```
    cellstr('X_O2'), cellstr('X_H2O'), cellstr('X_H2'),
    cellstr('X_CH4'), cellstr('X_C2H4'), cellstr('X_C2H6'),
    cellstr('Sum X_i')]; %For storage of result data
resultGCSpeciesBalancesMoleFractions=[h5,GCH2profile,GCCH4profile,
GCH2Oprofile,GCCOprofile,GCO2profile,GCCO2profile,GCC2H4profile,
GCC2H6profile,GCCbalance,GCHbalance,GCObalance,GCXArprofile,GCXHeprofile,
GCXCOprofile,GCXO2profile,GCXCO2profile,GCXH2Oprofile,
GCXH2profile,GCXCH4profile,GCXC2H4profile,GCXC2H6profile,GCCheckSum];
%For storage of result data
resultGCSpeciesBalancesMoleFractionsLabel=[cellstr('axial position
    species/balances [m]'), cellstr('F H2 [mol/min]'), cellstr('F
    CH4 [mol/min]'), cellstr('F H2O [mol/min]'), cellstr('F CO
    [mol/min]'), cellstr('F O2 [mol/min]'), cellstr('F CO2
    [mol/min]'), cellstr('F C2H4 [mol/min]'), cellstr('F C2H6
    [mol/min]'), cellstr('C balance [percent]'), cellstr('H balance
    [percent]'), cellstr('O balance [percent]'), cellstr('X_Ar'),
    cellstr('X_He'), cellstr('X_CO'), cellstr('X_CO2'),
    cellstr('X_O2'), cellstr('X_H2O'), cellstr('X_H2'),
    cellstr('X_CH4'), cellstr('X_C2H4'), cellstr('X_C2H6'),
    cellstr('Sum X_i')]; %For storage of result data
clear h4 h5;

disp('Evaluation ready.');

%-----------------------------------------------------------------------
%Write all results in one result files (ASCII, JPG)
                                %
%-----------------------------------------------------------------------
h1=input('Do you wanna store data to file? (Y/N)', 's');

tic

if h1=='Y',
    dlmwrite('MS.txt',resultSpeciesBalancesMoleFractions);
    fid=fopen('MSlabel.txt', 'w');
    for k=1:length(resultSpeciesBalancesMoleFractionsLabel),
        if k<length(resultSpeciesBalancesMoleFractionsLabel),
            fprintf(fid,
                [cell2mat(resultSpeciesBalancesMolefractionsLabel(k))
                ',']);
        else
        fprintf(fid,
            [cell2mat(resultSpeciesBalancesMoleFractionsLabel(k))
            '\n']);
        end
    end
    fclose(fid);
    !copy MSlabel.txt+MS.txt result_MS.txt;
    delete MS.txt MSlabel.txt;
```

```
    dlmwrite('GC.txt',resultGCSpeciesBalancesMoleFractions);
    fid=fopen('GClabel.txt', 'w');
    for k=1:length(resultGCSpeciesBalancesMoleFractionsLabel),
        if k<length(resultGCSpeciesBalancesMoleFractionsLabel),
            fprintf(fid,
                [cell2mat(resultGCSpeciesBalancesMoleFractionsLabel(k))
                ',']);
        else
        fprintf(fid,
            [cell2mat(resultGCSpeciesBalancesMoleFractionsLabel)
            '\n']);
        end
    end
    fclose(fid);
    !copy GClabel.txt+GC.txt result_GC.txt;
    delete GC.txt GClabel.txt;

    dlmwrite('Tc.txt', resultTc);
    fid=fopen('Tclabel.txt', 'w');
    for k=1:length(resultTcLabel),
        if k<length(resultTcLabel),
            fprintf(fid, [cell2mat(resultTcLabel(k)) ',']);
        else
            fprintf(fid, [cell2mat(resultTcLabel(k)) '\n']);
        end
    end
    fclose(fid);
    !copy Tclabel.txt+Tc.txt result_Tc.txt;
    delete Tc.txt Tclabel.txt;

    saveas(gcf-2, 'T thermocouple profile.jpg');
    saveas(gcf-1, 'Molar flow rates profile.jpg');
    saveas(gcf, 'Mass balances profile.jpg');

elseif h1=='y',
    dlmwrite('MS.txt',resultSpeciesBalancesMoleFractions);
    fid=fopen('MSlabel.txt', 'w');
    for k=1:length(resultSpeciesBalancesMoleFractionsLabel),
        if k<length(resultSpeciesBalancesMoleFractionsLabel),
            fprintf(fid,
                [cell2mat(resultSpeciesBalancesMoleFractionsLabel(k))
                ',']);
        else
        fprintf(fid,
            [cell2mat(resultSpeciesBalancesMoleFractionsLabel(k))
            '\n']);
        end
    end
```

```
    fclose(fid);
    !copy MSlabel.txt+MS.txt result_MS.txt;
    delete MS.txt MSlabel.txt;

    dlmwrite('GC.txt',resultGCSpeciesBalancesMoleFractions);
    fid=fopen('GClabel.txt', 'w');
    for k=1:length(resultGCSpeciesBalancesMoleFractionsLabel),
        if k<length(resultGCSpeciesBalancesMoleFractionsLabel),
            fprintf(fid,
                [cell2mat(resultGCSpeciesBalancesMoleFractionsLabel(k))
                ',']);
        else
        fprintf(fid,
            [cell2mat(resultGCSpeciesBalancesMoleFractionsLabel)
            '\n']);
        end
    end
    fclose(fid);
    !copy GClabel.txt+GC.txt result_GC.txt;
    delete GC.txt GClabel.txt;

    dlmwrite('Tc.txt', resultTc);
    fid=fopen('Tclabel.txt', 'w');
    for k=1:length(resultTcLabel),
        if k<length(resultTcLabel),
            fprintf(fid, [cell2mat(resultTcLabel(k)) ',']);
        else
            fprintf(fid, [cell2mat(resultTcLabel(k)) '\n']);
        end
    end
    fclose(fid);
    !copy Tclabel.txt+Tc.txt result_Tc.txt;
    delete Tc.txt Tclabel.txt;

    saveas(gcf-3, 'T thermocouple profile.jpg');
    saveas(gcf-2, 'Molar flow rates profile.jpg');
    saveas(gcf-1, 'Mass balances profile.jpg');
    saveas(gcf, 'Mole fractions profile.jpg');
else
    disp('OK');
end

disp('Done.');
toc

disp('---------');
```

Appendix C MATLAB Script for Oven Temperature Fit

Herebelow is a MATLAB script [1] allowing to create a 3D plot of the oven temperature as a function of oven heating power and axial position. As the initial input, three vectors should be defined, which are power (x), position (y) and oven temperature profile (z). In total 5 oven temperature profiles were measured; accordingly, 5 various oven heating power settings are to be defined in the script.

```
ll %[X,Y] = meshgrid(-1:.2:1, -2:.2:2);
% Z = X .* exp(-X.^2 - Y.^2);
% surf(X,Y,Z)
power=[133.17041 185.00517 252.68906 345.91756 450.51228]
Tcoilset=[450 550 650 750 850]
position=[1:.1:15]
[X,Y] = meshgrid(power,position)
z450=spline(toven450(:,1),toven450(:,2),position)
z550=spline(toven550(:,1),toven550(:,2),position)
z650=spline(toven650(:,1),toven650(:,2),position)
z750=spline(toven750(:,1),toven750(:,2),position)
z850=spline(toven850(:,1),toven850(:,2),position)
Z=[z450;z550;z650;z750;z850]'
surf(X,Y,Z)
function [fitresult, gof] = createSurfaceFit(powervector,
    positionvector, temperaturevector)
%  CREATESURFACEFIT(POWERVECTOR,POSITIONVECTOR,TEMPERATUREVECTOR)
%  Fit surface to data.
%  Data for 'Oven Temperature Profile' fit:
%  X Input : powervector
%  Y Input : positionvector
%  Z output: temperaturevector
%  Weights : (none)
```

[1] The script was developed by Dr. Raimund Horn, FHI

```
%  Output:
%  fitresult : an sfit object representing the fit.
%  gof : structure with goodness-of fit info.
%  See also FIT, SFIT.
%  Auto-generated by MATLAB on 25-Mar-2011 12:13:04
%  Fit: 'Oven Temperature Profile'.
ft = fittype( 'poly33' );
opts = fitoptions( ft );
opts.Weights = zeros(1,0);
[fitresult, gof] = fit( [powervector, positionvector],
    temperaturevector, ft, opts );
% Plot fit with data.
figure( 'Name', 'Oven Temperature Profile' );
h = plot( fitresult, [powervector, positionvector],
    temperaturevector );
grid on
% Label axes
xlabel( 'powervector' );
ylabel( 'positionvector' );
zlabel( 'temperaturevector' );
legend( h, 'Oven Temperature Profile', 'temperaturevector vs.
    powervector, positionvector', 'Location', 'NorthEast' );
view( -44.5, 30 );
```

Appendix D Calculation of Diffusion Coefficients and Plug-Flow Validity Criterion

The molecular diffusion coefficient for the binary mixture according to Bird et al. [17] was calculated based on mean free path arguments and the Chapman-Enskog kinetic theory [143]. The diffusion coefficient according to Fuller et al. [18] was calculated similar to the example shown by Hayes and Kolaczkowski [112] on p. 228. Figure 9 shows diffusion coefficients calculated by these two group of authors. As is seen, the diffusion coefficients in the sub-figures are essentially identical, showing good agreement of the two approaches.

The diffusion coefficient calculations were ultimately used to calculate the criterion of Cleland and Wilhelm. The result of calculation using the profile of residence times extracted from the experimental temperature profiles is shown in Figure 10. According to the authors, the plug-flow regime is valid when $\lambda\alpha$ is more than 1, and in the figure this criterion is less than 1, signifying the validity of the boundary-layer flow regime.

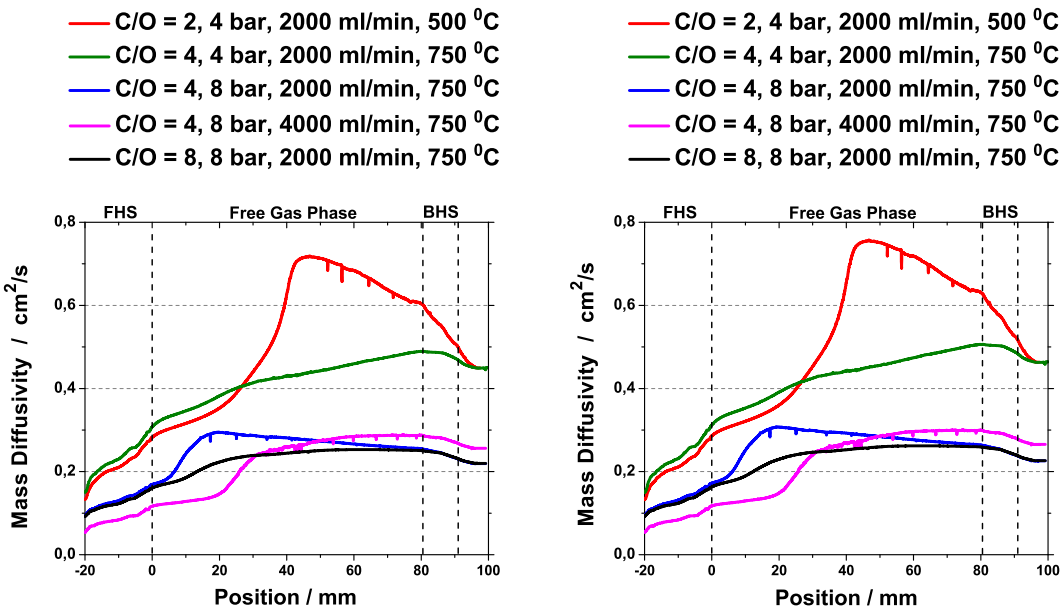

Figure 9: Profiles of the mass diffusion coefficients for the CH_4 – O_2 binary mixture according to (a) Bird et al. [17] and (b) Fuller et al. [18].

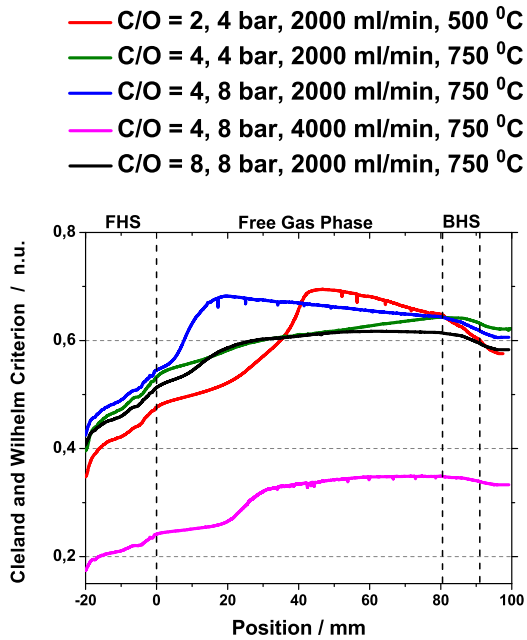

Figure 10: Cleland and Wilhelm [19] criterion applied to experimental profiles in this thesis to verify plug-flow limit validity.

References

[1] Dooley, S., Burke, M. P., Chaos, M., Stein, Y., Dryer, F. L., Zhukov, V. P., Finch, O., Simmie, J. M., and Curran, H. J. *Int. Jour. of Chem. Kin.* **42**, 527–549 (2010). ii, iv, v, viii, ix, xii, xv, xvi, 17, 18, 77, 78, 80, 91, 108, 110, 113, 114

[2] Lopez, J. G., Rasmussen, C. L., Alzueta, M. U., Gao, Y., Marshall, P., and Glarborg, P. *Proc. of the Combustion Inst.* **32**, 367–375 (2009). ii, iv, xiii, xv, 17, 18, 80, 81, 108, 111

[3] Warnatz, J., Dibble, R. W., and Maas, U. *Combustion: Physical and Chemical Fundamentals, Modeling and Simulation.* Springer-Verlag, New York, (1996). ii, iv, xiii, 9, 11, 17, 18, 56, 82, 83, 84

[4] Konnov, A. A. *Combustion and Flame* **156**, 2093–2105 (2009). ii, iv, viii, xiii, 17, 18, 84, 85

[5] Mims, C., Mauti, R., Dean, A. M., and Rose, K. D. *J. Phys. Chem.* **98**, 13357–13358 (1994). ii, iv, v, viii, xiii, 16, 17, 18, 84, 86, 96

[6] Wang, H., You, X., Joshi, A. V., Davis, S. G., Laskin, A., Egolfopoulos, F., and Law, C. K. *High-Temperature Combustion Reaction Model of H2/CO/C1-C4 Compounds.* University of South California, May (2007). iii, iv, xiv, 17, 18, 84, 87, 88

[7] Zanthoff, H. and Baerns, M. *Ind. Eng. Chem. Res.* **29**, 2–10 (1990). iii, iv, xiv, 15, 17, 18, 87, 89, 103

[8] Hughes, K. J., Turanyi, T., Clague, A. R., and Pilling, M. J. *Int. Jour. Chem. Kinet.* **33**, 513–538 (2001). iv, 17, 18, 87

[9] Sun, J., Thybaut, J. W., and Marin, G. B. *Catalysis Today* **137**, 90–102 (2008). iv, 16, 17, 18, 87, 102

[10] Smith, G. P., Golden, D. M., Frenklach, M., Moriarty, N. W., Eiteneer, B., Goldenberg, M., Bowman, C. T., Hanson, R. K., Song, S., Gardiner, W. C., Lissianski, V. V., and Qin, Z. *GRI Mechanism Version 3.0.* http://www.me.berkeley.edu/grimech/version30/, (1999). iv, 17, 18, 87

[11] Warnatz, J., Maas, U., and Dibble, R. W. *Combustion: Physical and Chemical Fundamentals, Modeling and Simulation, Experiments, Pollutant Formation.* Springer Berlin Heidelberg, (2006). x, xi, 9, 10, 50, 53

[12] Horn, R., Korup, O., Geske, M., Zavyalova, U., Oprea, I., and Schlögl, R. *Rev. Sci. Instrum.* **81**(6), 64102–64102 (2010). x, 20, 23, 24, 25

[13] Zabetakis, M. G. Technical report, U.S. Bureau of Mines. Bulletin 627, (1965). x, 29, 30

[14] de Hoffmann, E. and Stroobant, V. *Mass Spectrometry: Principles and Applications (Third ed.).* John Wiley & Sons, Ltd., Chichester, (2007). xi, 33, 38

[15] Keulemans, A. I. M. *Gas Chromatography.* Reinhold Publishing Corporation, New York, (1957). xi, 40

[16] Purnell, H. *Gas Chromatography.* John Wiley & Sons, Inc., (1962). xi, 39, 41

[17] Bird, R. B., Stewart, W. E., and Lightfoot, E. N. *Transport phenomena, 2nd edition.* John Wiley & Sons, Inc., (2002). xvi, 62, 149, 150

[18] Fuller, E. N., Schettler, P. D., and Giddings, J. C. *Ind. Eng. Chem.* **58**, 19–27 (1966). xvi, 62, 149, 150

[19] Cleland, F. A. and Wilhelm, R. H. *AIChE Journal* **2**, 489–497 (1956). xvi, 61, 150

[20] Kee, R., Rupley, F. M., and Miller, J. A. Technical report, Sandia National Laboratories, Albuquerque, NM, SAND 87-8215, (1987). xvii, 7, 8, 54

[21] Pacala, S. and Socolow, R. *Science* **305**, 968–972 (2004). 1

[22] Review. *World Energy Outlook*. British Petroleum Corporation, (2011). 1

[23] Wood, R., Gilbert, P., Sharmina, M., Anderson, K., Fottitt, A., Glynn, S., and Nicholls, F. Technical report, Tyndall Center, University of Manchester, Manchester, England., (2011). 1

[24] Haldor-Topsoe. *Oryx synthesis gas technology*. Preprint from Hydrocarbon Engineering, (2006). 3

[25] Zhao, T. and Wang, H. *Journal of Natural Gas Chemistry* **20**, 547–552 (2011). 3

[26] Rokstad, O., Olsvik, O., Jenssen, B., and Holmen, A. *Novel Production Methods for Ethylene, Light Hydrocarbons and Aromatics*, chapter Ethylene, Acetylene and Benzene from Methane Pyrolysis, 259. Marcel Dekker, New York (1992). 3, 7

[27] Olah, G. A., Goeppert, A., and Surya Prakash, G. K. *Beyond Oil and Gas: The Methanol Economy*. Wiley-VCH Verlag GmbH & Co. KGaA, Weinheim, (2006). 3

[28] Eilers, J., Posthuma, S. A., and Sie, S. T. *Catal. Lett.* **7**, 1–4 (1990). 3

[29] Wolf, E. E., editor. *Methane Conversion by Oxidative Processes. Fundamental and Engineering Aspects*. Van Nostrand Reinhold, New York, (1992). 4, 8, 74

[30] Onsager, O. T., Loedeng, R., Soeraker, P., Anundskaas, A., and Helleborg, B. *Catalysis Today* **4**, 355–363 (1989). 4, 7, 9, 14

[31] Hutchings, G. J., Scurrell, M. S., and Woodhouse, J. R. *J. Chem. Soc., Chem. Commun.* , 253–255 (1988). 4, 14, 15

[32] Sinev, M. Y., Fattakhova, Z. T., Lomonosov, V. I., and Gordienko, Y. A. *Jour. of Nat. Gas. Chem.* **18**, 273–287 (2009). 4

[33] Blanksby, S. J. and Ellison, G. B. *Acc. Chem. Res.* **36**, 255–263 (2003). 7

[34] Pitchai, R. and Klier, K. *Catal. Rev.: Sci. and Eng.* **28**, 13–88 (1986). 7, 8

[35] Norrish, R. G. W. and Foord, S. G. *Proc. R. Soc. Lond.: A* **157**, 503–525 (1936). 7, 8

[36] Karmilova, L. V., Enikolopyan, N. S., Nalbandyan, A. B., and Semenov, N. N. *Zh. Fiz. Chim.* **34**, 1176 (1960). 7

[37] Gesser, H. D., Hunter, N. R., and Prakash, C. B. *Chemical Reviews* **85**, 235–244 (1985). 7, 11

[38] Gesser, H. D., Hunter, N. R., and Prakash, C. B. *Preprints American Chemical Society, Division of Fuel Chemistry* **32**, 255 (1987). 7

[39] Yarlagadda, P. S., Morton, L. A., Hunter, N. R., and Gesser, H. D. *Ind. Eng. Chem. Res.* **27**, 252–256. (1988). 8

[40] Semenov, N. N. *Chain Reactions (English translation).* Oxford University Press, (1935). 8

[41] Vardanyan, I. A. and Nalbandyan, A. B. *Int. Jour. Chem. Kinet.* **17**, 901–924 (1985). 9, 16

[42] Benson, S. W. *Prog. in Energy and Comb. Sci.* **7**, 125–134 (1981). 10

[43] Mackie, J. C. *Catal. Rev. - Sci. Eng.* **33**(1&2), 169–240 (1991). 10, 97

[44] Hoare, D. E. and Walsh, A. D. In *5th Symposium (International) on Combustion; Pittsburgh, PA; 30 August 1954 through 3 September 1954; Code 87678*, (1955). 11

[45] Mahajan, S., Menzies, W. R., and Albright, L. F. *Ind. and Eng. Chem. Proc. Des. and Dev.* **16**, 271–274 (1977). 11

[46] Rytz, D. W. and Baiker, A. *Ind. Eng. Chem. Res.* **30**, 2287–2292 (1991). 11

[47] Rasmussen, C. L., Jakobsen, J. G., and Glarborg, P. *Int. Jour. of Chem. Kin.* **40**, 778–807 (2008). 11, 101

[48] Vedeneev, V. I., Arutyunov, V. S., Krymov, N. Y., Cherbakov, P. M., and Sedykh, A. D. *Catal. Today* **13**, 613–616 (1992). 11

[49] Bone, W. A. and Gardner, J. B. *Proc. Royal. Soc. London* **154**, 297–328 (1936). 11

[50] Lane, G. S. and Wolf, E. E. *Jour. of Catal.* **113**, 144–163 (1988). 11, 14, 21, 68, 74

[51] Warnatz, J. In *18th International Combustion Symposium, The Combustion Institute*, (1981). 11, 12, 98

[52] Asami, K., Omata, K., Fujimoto, K., and Tominaga, H. *J. Chem. Soc., Chem. Commun.* , 1287–1288 (1987). 12, 14

[53] van Kasteren, J., Geerts, J., and van der Wiele, K. *Catalysis Today* **6**, 497–502 (1990). 13

[54] Keller, G. E. and Bhasin, M. M. *Journal of Catalysis* **73**, 9–19 (1982). 13

[55] Driscoll, D. J., Campbell, K. D., and Lunsford, J. H. *Advances in Catalysis* **35**, 139–186 (1987). 13

[56] Couwenberg, P. M. *Gas-phase chain reactions catalyzed by a solid: the oxidative coupling of methane.* PhD thesis, Eindhoven University of Technology, (1995). 13, 68, 76, 102

[57] Lin, C. H., Ito, T., Wang, J.-X., and Lunsford, J. H. *J. Am. Chem. Soc.* **109**, 4808–4810 (1987). 13

[58] Campbell, K. D., Morales, E., and Lunsford, J. H. *J. Am. Chem. Soc.* **109**, 7900–7901 (1987). 13, 103

[59] Lunsford, J. H. *Angewandte Chemie, International Edition in English* **34**, 970–980 (1995). 13, 103

[60] Myrach, P., Nilius, N., Levchenko, S. V., Gonchar, A., Risse, T., Dinse, K. P., Boatner, L., Frandsen, W., Horn, R., Freund, H. J., Schlögl, R., and Scheffler, M. *ChemCatChem* **2**, 854–862 (2010). 13

[61] Martin, G. A., Bates, A., Ducarme, V., and Mirodatos, C. *Appl. Catal.* **47**, 287–297 (1989). 14

[62] Chen, Q., Couwenberg, P. M., and Marin, G. B. *AIChE J.* , 521–535 (1994). 14, 15, 16

[63] Ekstrom, A., Regtop, R., and Bhargava, S. *Appl. Catal.* **62**, 253–269 (1990). 14

[64] Tulenin, Y. P., Kadushin, A. A., Seleznev, V. A., Shestakov, A. F., and Menshikov, V. A. *Catal. Today* **13**, 329–337 (1992). 14, 15

[65] Tulenin, Y. P., Kadushin, A. A., Seleznev, V. A., Shestakov, A. F., and Menshikov, V. A. *Catal. Today* **13**, 523–528 (1992). 14, 15

[66] Chen, Q., Hoebink, H. B. J., and Marin, G. B. *Ind. Eng. Chem. Res.* **30**, 2088–2097 (1991). 15, 102

[67] Sekine, Y., Nishimura, T., and Fujimoto, K. *Energy & Fuels* **12**, 828–829 (1998). 15

[68] Hunter, T. B., Wang, H., Litzinger, T. A., and Frenklach, M. *Combustion and Flame* **97**, 201–224 (1994). 15, 16, 19, 21

[69] Geerts, J., Chen, Q., van Kasteren, J., and van der Wiele, K. *Catalysis Today* **6**, 519–526 (1990). 15, 16

[70] Tjatjopoulos, G. J. and Vasalos, I. A. *Applied Catalysis A: General* **88**, 213–230 (1992). 15, 103

[71] Qui, X., Zhu, Q., Wong, N., and Tin, K. *Jour. Chem. Tech. Biotechnol.* **65**, 380–384 (1996). 16

[72] Vedeneev, V. I., Krylov, O. V., Arutyunov, V. S., Basevich, V. Y., Goldenberg, M. Y., and Teitel boim, M. A. *Applied Catalysis A: General* **127**, 51–53 (1995). 16

[73] Steinle, J. U. and Franck, E. U. *Ber. Bunsen-Ges. Phys. Chem.* **99**, 66–73 (1995). 16

[74] Blundell, R. V., Cook, W. G. A., Hoare, D. E., and Milne, G. S. *Proc. Combust. Inst.* **10**, 445–452 (1965). 16

[75] Williams, G. C., Hottel, H. C., and Morgan, A. C. *Proc. Combust. Inst.* **12**, 913–925 (1965). 16

[76] Rotzoll, G. *Combustion Science and Technology* **47**, 275–298 (1986). 16

[77] Dagaut, P., Boettner, J.-C., and Cathonnet, M. *Combustion Science and Technology* **77**, 127–148 (1991). 16

[78] Bromly, J. H., Barnes, F. J., Muris, S., You, X., and Haynes, B. S. *Combustion Science and Technology* **115**, 259–296 (1996). 16

[79] Bendtsen, A. B., Glarborg, P., and Dam-Johansen, K. *Combustion Science and Technology* **151**, 31–71 (2000). 16

[80] Skjoeth-Rasmussen, M. S., Glarborg, P., Oestberg, M., Johanessen, J. T., Livbjerg, H., Jensen, A. D., and Christensen, T. S. *Combustion and Flame* **136**, 91–128 (2004). 16, 73

[81] Dagaut, P. and Nicolle, A. *Combustion and Flame* **140**, 161–171 (2005). 16

[82] Burcat, A., Scheller, K., and Lifshitz, A. *Combustion and Flame* **16**, 29–33 (1971). 16

[83] Lifshitz, A., Scheller, K., Burcat, A., and Skinner, G. B. *Combustion and Flame* **16**, 311–321 (1971). 16

[84] Bowman, C. T. *Proc. Combust. Inst.* **15**, 869–882 (1974). 16

[85] Olson, D. B. and Gardiner, W. C. *Combustion and Flame* **32**, 151–161 (1978). 16

[86] Levy, Y., Olchanski, E., Sherbaurn, V., Erenburg, V., and Burcat, A. *Jour. Propulsion Power* **22**, 669–676 (2006). 16

[87] Peeters, J. and Mahnen, G. *Proc. Combust. Inst.* **14**, 133–146 (1974). 16

[88] Egolfopoulos, F. N., Cho, P., and Law, C. K. *Combustion and Flame* **76**, 375–391 (1989). 16

[89] Heard, D. E., Jeffries, J. B., Smith, G. P., and Crosley, D. R. *Combustion and Flame* **88**, 137–148 (1992). 16

[90] Davies, S. G. and Law, C. K. *Combustion Science and Technology* **140**, 427–449 (1998). 16

[91] Turbiez, A., Bakali, A. E., Pauwels, J. F., Rida, A., and Meunier, P. *Fuel* **83**, 933–941 (2004). 16

[92] Goos, E., Burcat, A., and Ruscic, B. *Extended Third Millenium Ideal Gas and Condensed Phase Thermochemical Database for Combustion with Updates from Active Thermochemical Tables.* Argonne National Laboratories Report ANL-05/20, Technion Aerospace Report TAE 960, (2005). 16, 54

[93] *CHEMKIN Thermodynamic Database.* Reaction Design, Sandia National Laboratories. 18

[94] Shannon, S. L. and Goodwin, Jr., J. G. *Chem. Rev.* **95**(3), 677–695 (1995). 19

[95] Gleaves, J. T., Ebner, J. R., and Kuechler, T. C. *Catal. Rev.: Sci. Eng.* **30**, 49116 (1988). 19

[96] Gleaves, J. T., Yablonsky, G., Zheng, X., Fushimi, R., and Mills, P. L. *J. Mol. Catal. A: Chem.* **315**, 108–134 (2010). 19

[97] Dagaut, P., Cathonnet, M., Rouan, J. P., Foulatier, R., Quilgars, A., Boettner, J. C., Gaillard, F., and James, H. *J. Phys. E.: Sci. Instrum* . **19**, 207–209 (1986). 19

[98] Dagaut, P., Cathonnet, M., and Boettner, J. C. *J. Phys. Chem.* **96**, 991 (1988). 19

[99] Brezinsky, K., Litzinger, T. A., and Glassman, I. *Int. Jour. Chem. Kinet.* **16**, 1053–1074 (1984). 19, 21

[100] Lyubovsky, M., Roychoudhury, S., and LaPierre, R. *Catal. Lett.* **99**, 113–117 (2005). 19

[101] Partridge, W. P., Storey, J. M. E., Lewis, S. A., Smithwick, R. W., DeVault, G. L., Cunningham, M. J., Currier, N. V., and Yonushonis, T. M. *SAE Int. J. Fuels Lubr.* **109**, 2992–2999 (2000). 20

[102] Sa, J., Fernandes, D. L. A., Aiouache, F., Goguet, A., Hardcare, C., Lundie, D., Naeem, W., Partridge, W. P., and Stere, C. *Analyst* **135**, 2260–2272 (2010). 20

[103] Bosco, M. and Vogel, F. *Catal. Today* **116**, 348–353 (2006). 20

[104] Horn, R., Williams, K. A., Degenstein, N. J., and Schmidt, L. D. *J. Catal.* **242**(1), 92–102 (2006). 20, 25, 57

[105] Horn, R. *In-Situ Measurements of Spatially Resolved Spectroscopic Data within a Reactor Chamber of a Reactor.* European Patent WO2011072701, (6/23/2011). 20

[106] Horn, R., Williams, K. A., Degenstein, N. J., Bitsch-Larsen, A., Dalle Nogare, D., Tupy, S. A., and Schmidt, L. D. *J. Catal.* **249**(2), 380–393 (2007). 20, 80

[107] Horn, R., Williams, K. A., Degenstein, N. J., and Schmidt, L. D. *Chem. Eng. Sci.* **62**(5), 1298–1307 (2007). 20

[108] Dalle Nogare, D., Degenstein, N. J., Horn, R., Canu, P., and Schmidt, L. D. *J. Catal.* **258**(1), 131–142 (2008). 20

[109] Korup, O., Mavlyankariev, S., Geske, M., Goldsmith, C. F., and Horn, R. *Chem. Eng. and Processing: Process Intensification* **50**, 998–1009 (2011). 20, 21

[110] Vanderstraeten, B., Tuerlinckx, D., Berghmans, J., Vliegen, S., Van't Oost, E., and Smit, B. *J. Hazard. Mater.* **56**, 237–246 (1997). 29

[111] Plehiers, P. M. and Froment, G. F. *Oil and Gas Journal* , 41–49 (1987). 44, 61

[112] Hayes, R. E. and Kolaczkowski, S. T. *Introduction to Catalytic Combustion.* Gordon and Breach Science Publishers, Amsterdam, (1997). 46, 149

[113] Korup, O. *Methane Oxidation on Platinum Catalysts Investigated by Spatially Resolved Methods.* PhD thesis, Technische Universität Berlin, (2012). 47, 127

[114] Dumesic, J., Rudd, D. F., Aparicio, L. M., Rekoske, J. E., and Trevino, A. A. *The Microkinetics of Heterogeneous Catalysis.* Wiley-VCH, (1993). 48, 50

[115] Kee, R. J., Miller, J. A., and Jefferson, T. H. *CHEMKIN: A General-Purpose, Problem-Independent, Transportable, Fortran Chemical Kinetics Code Package.* Sandia National Laboratories, Albuquerque, New Mexico, sand 80-8003 edition, (1980). 48

[116] Hindmarsh, A. C. *ACM Signum Newsletter* **15(4)** (1980). 49

[117] Gear, W. C. *Numerical Initial Value Problems in Ordinary Differential Equations.* Prentice-Hall, Englewood Cliffs, NJ, (1971). 49

[118] CHEMKIN-PRO. Reaction Design, San Diego, 15101 edition, (2010). 49, 55, 57, 93

[119] Reaction Design: San Diego. *CHEMKIN-PRO Theory Manual.* Reaction Design, San Diego, (2008). 49

[120] Lindemann, F. A. *Trans. Faraday Soc.* **17**, 598 (1922). 50

[121] Gilbert, R. G., Luther, K., and Troe, J. *Ber. Bunsenges. Phys. Chem.* **87**, 169 (1983). 52

[122] Stewart, P. H., Larson, C. W., and Golden, D. M. *Combustion & Flame* **75**, 25–31 (1989). 53

[123] Wang, H. and Frenklach, M. *Chem. Phys. Lett.* , 271–276 (1993). 53

[124] Gardiner, W. C. In *12th IMACS World Congress on Scientific Computations, Paris*, (1988). 53

[125] Poole, J. S. and Gilbert, R. G. *Int. J. Chem. Kinet.* **26**, 273–281 (1994). 53

[126] Benson, S. *Thermochemical Kinetics: Methods for the Estimation of Thermochemical Data and Rate Parameters.* Wiley, New York, (1976). 54

[127] Stall, D. R. and Prophet, H. *JANAF Thermochemical Tables.* Technical Report, Department of Commerce, Washington DC, (1971). 54

[128] Svehla, R. A. *Estimated Viscosities and Thermal Conductivities of Gases at High Temperatures.* NASA Technical Report R-132, (1962). 55

[129] Kee, R. J., Coltrin, M. E., and Glarborg, P. *Chemically Reacting Flow: Theory and Practice.* John Wiley & Sons, Inc., (2003). 58, 60

[130] Bityukov, V. K. and Petrov, V. A. *High Temperature* **38**, 293–299 (2000). 63

[131] Incropera, F. P., DeWitt, D. P., Bergmann, T. L., and Lavine, A. S. *Fundamentals of Heat and Mass Transfer.* John Wiley & Sons, (2006). 64

[132] Technical report, National Institute of Standards and Technology, (2011). 69

[133] Weisz, P. B. *CHEMTECH* , 424 (1982). 74, 112

[134] Reaction Mechanism Generator. Green, W. H., Allen, J. W., Ashcraft, R. W., Beran, G. J., Class, C. A., Gao, C., Goldsmith, C. F., Harper, M. R., Jalan, A., Magoon, G. R., Matheu, D. M., Merchant, S. S., Mo, J. D., Petway, S., Raman, S., Sharma, S., Song, J., Van Geem, K. M., Wen, J., West, R. H., Wong, A., Wong, H. W., Yelvington, P. E., and Yu, J. Massachusetts Institute of Technology, 3.3 edition, (2011). 77, 80

[135] Vereecken, L., Nguyen, T. L., Hermans, I., and Peeters, J. *Chemical Physics Letters* **393**, 432–436 (2004). 80

[136] Semenov, N. N. *Some Problems in Chemical Kinetics and Reactivity.* Princeton University Press, (1958). 97

[137] Warnatz, J. *Ber. Bunsenges. Phys. Chem.* **83**, 950 (1979). 98

[138] Warnatz, J. In *24th Int. Symp. Combust., 553, Pittsburgh, The Combustion Institute*, (1993). 98

[139] Fenimore, C. P. and Jones, G. W. *J. Chem. Phys.* **39**, 1514–1519 (1963). 100

[140] Michael, J. V. and Wagner, A. F. *J. Phys. Chem.* **94**, 2453–2464 (1990). 100

[141] Chikan, V. and Leone, S. R. *J. Phys. Chem.* **109**, 2525–2533 (2005). 100

[142] Bhatia, S., Thien, C. Y., and R., M. A. *Chemical Engineering Journal* **148**, 525–532 (2009). 112

[143] Chapman, S. and Cowling, T. G. *The MathematicaI Theory of Non-Unifovm Gases, 3rd edition.* Cambridge University Press, (1970). 149

Acknowledgements

I would like to thank and express my deep gratitude to Dr. Raimund Horn, Prof. Dr. Robert Schlögl and Prof. Dr. Reinhard Schomäcker for mentoring my thesis, for continuous scientific and personal support that made this thesis become real. Also special gratitude to Dr. Jean-Philippe Lonjaret, the managing director of the BIG-NSE Graduate School, for selection and interview invitation for my candidature, as well as continuous support whenever I and other members of the school needed help on various matters. His endeavours to make the PhD studies for BIG-NSE students not only productive (courses on scientific writing, English and German language, on project compilation), but also enjoyable (soft-skill courses, social events and cultural programmes) deserve special mention. In this regard, I would thank Prof. Reinhard Schomäcker once again for conducting the selection procedures for BIG-NSE candidates and supporting the students of the School in the status of the Director of the BIG-NSE Graduate School.

Endless thanks to my lab-colleagues Dr. Oliver Korup, Dr. Michael Geske, Dr. Claude Franklin Goldsmith, Heiner Schwarz and Dr. Hugo Petitjean. These people, especially Dr. Oliver Korup and Dr. Michael Geske, helped me to adapt to the group as I was a newcomer, introduced to me the various techniques and mentored and co-performed the exhausting experimental work for my thesis. I cannot imagine if I could have gone so far without their help. Besides, I would like to thank PhD colleagues Pierre Schwach and Timur Kandemir for readily agreeing to conduct night-time experiments with me, which is pretty tiring piece of work.

My family for enduring my long-term absence from home, moral support and blessings. Without them creation of this thesis would likely not have been possible. In addition, my own family: girlfriend Hong Thi Diem Nguyen and

my sweet daughter Nigora for direct everyday support and understanding. Last, but not at all the least, my colleagues from BIG-NSE family, many of whom are already a cohort of Doctors: Stanislav Jaso, Subhamoy Bhattacharya, Sylvia Reiche, Carlos Carrero, Kirstin Hobiger, Manuel Harth and Sara Bruun for very fruitful scientific discussions and chill-out together.

Curriculum Vitae

Personal information	
Name	Sardor Mavlyankariev
Date and place of birth	23.03.1984, Tashkent, Uzbekistan
Address	Fritz-Haber-Institut der MPG, Abteilung AC Faradayweg 4-6, 14195 Berlin
Email	sardor@hotmail.com
Education	
7/2008 – 6/2013	PhD Thesis "Investigation of Oxidative Coupling of Methane in the Gas Phase by Reactor Profile Measurements and Microkinetic Modeling" at Fritz Haber Institute, Berlin
8/2005 – 8/2007	Master Thesis "Application of Coated Amphoteric Metal Oxides in Adsorption and Photocatalysis" at Kangwon National University, Korea
8/2001 – 7/2005	Bachelor Diploma "Design of Selective Acetylene Hydrogenation Unit of the Shurtan Gas-Chemical Complex" at Tashkent Institute of Chemical Technology, Uzbekistan
Language and	Uzbek (mother language), Russian (fluent), English (fluent), German (basic conversational)
software skills	MS Office, Origin, Chemkin, LaTeX

Scholarships	PhD Scholarship from "Berlin International Graduate School of Natural Sciences and Engineering" Master Course Scholarship from The Ministry of Education of Republic of Korea

Publications

1. O. Korup, S. Mavlyankariev, M. Geske, C. F. Goldsmith, R. Horn, "Measurement and analysis of spatial profile reactors in high temperature catalysis research", Chemical Engineering and Processing: Process Intensification, 50, 2011, 998 – 1009.